Effects of freeze-thaw of ballasted track on railway train vibration in cold regions and its evaluation

凍結融解が有道床軌道の軌道狂いと車体動揺に及ぼす影響とその評価に関する研究

by

Shoulong Zhang

A thesis submitted in partial fulfilment of the requirements for the degree of Doctor of Philosophy in Engineering

under the guidance and supervision of

Professor Tatsuya ISHIKAWA

Examined by the Doctoral Committee

Professor Tatsuya ISHIKAWA

Professor Yoichi WATABE

Professor Takashi MATSUMOTO

August 2022

English Engineering Education Program (e^3)

Laboratory of Analytical Geomechanics

Division of Field Engineering for the Environment

Graduate School of Engineering

Hokkaido University

Sapporo, Hokkaido, Japan

ABSTRACT

In the seasonally frozen regions, railway subgrades are subjected to freeze-thaw cycles due to environmental temperature change. The railway track is likely to be deformed during the freezing and thawing processes of subgrades. As a result, the maintenance work for railway track will increase, and train operations will be severely affected.

Due to the different geological and geotechnical conditions (for example, groundwater level, soil physical properties, moisture condition, and the existence of underground structures) along the track line, it can result in track unevenness when the freeze-thaw occurs. For instance, the culvert transition section experiences non-uniform spatial frost heaving and thaw settlement, resulting in track deformation. The present study employed a box culvert transition section of a ballasted track as the research object, and the track deformation induced by the freeze-thaw of railway subgrade was investigated. This study qualitatively and quantitatively studied the influence of freeze-thaw induced track deformation and its influence on the train vibration through freeze-thaw analysis and train vibration analysis. In the freeze-thaw analysis, different types of the buried structure (for example, box culvert, pipe culvert) embedded in the subgrade were selected as an analytical example, as the transition section of buried structure owning complex boundary conditions is likely to experience significant frost heave and thaw settlement. The track surface deformation above the transition section was calculated through finite element analysis, considering the influences of groundwater levels and temperature boundary conditions. Two indices, namely, wavelength and amplitude, were used to quantify the track surface deformation. The influence of variation of groundwater level and different seasonal temperatures on the deformation was investigated from the aspects of absolute value. Subsequently, to evaluate the influence of subgrade freeze-thaw induced track surface deformation on train vibration, the vehicle dynamic analysis was conducted using a vehicle-track model. The calculated absolute value of track surface deformation was inputted into the vehicle-track model as excitation. Finally, the car body vibration was evaluated from the aspect of safety (minimum vertical wheel-rail force, maximum vertical wheel-rail force, and wheel load reduction rate) and stability (car body acceleration and Sperling

index). This study can facilitate understanding the influence of subgrade freeze-thaw on vehicle vibration.

The thesis includes 7 Chapters. Chapter 1 introduces the background, literature review, objectives, and organization of this study. Chapter 2 introduces the freeze-thaw analysis of ballasted track, which include model definition, governing equation, parameters, and boundary conditions. Chapter 3 describes the train vibration analysis on ballasted track during freeze-thaw, which includes vehicle model, wheel-rail contact model, substructure model, model validation, and simulation condition. Chapter 4 evaluates the influence of GWL, temperature, and buried structure type on freeze-thaw induced track surface deformation. Chapter 5 discusses the influence of freeze-thaw induced track surface deformation on train vibration and gives a systematical evaluation of the train vibration from the train operation safety and stability. Chapter 6 discusses the growth of differential ballast settlement under cyclic load considering the influence of freeze-thaw induced track surface deformation. Finally, Chapter 7 summarizes the conclusions of this study and gives several recommendations for future studies.

ACKNOWLEDGEMENT

Firstly, I would like to express my sincere gratitude to my supervisor Prof. Tatsuya Ishikawa for his continuous support during my doctoral study and related research and his patience, motivation, and immense knowledge. His guidance helped me in my research and writing of this thesis all the time.

Sincere thanks are also due to all doctoral committee members, Prof. Watabe and Prof. Matsumoto for their invaluable comments and continuous assessments of my research and his tremendous support for the justification of this thesis.

I want to express my sincere thanks to Dr. Junping Ren for his full support and advice in my research. I am also greatly indebted to Dr. Bin Luo of Hokkaido University, who was always forward to helping me and suggesting valuable advice for my work. I gratefully acknowledge the students of the Laboratory of Analytical Geomechanics for their help during these three years.

I would also like to thank and express my sincere gratitude to my Professors in my home country, Dr. Jinhe Gao of ECIT (East China University of Technology) and Prof. Shijun Chen and Prof. Peng Li of ECIT (East China University of Technology). For their continuous support and guidance all through my research.

This research was made possible through the financial support from MEXT (The Monbukagakusho Scholarship), CSC (China Scholarship Council), and the English Engineering Education (e3) Program of Hokkaido University.

Finally, my special thanks are extended to my parents, family, and friends. Without their encouragement, support, and confidence in me throughout these years, it would not be possible for me to arrive in Japan and complete my doctoral study.

TABLE OF CONTENTS

ABSTRACT I

ACKNOWLEDGEMENT III

TABLE OF CONTENTS IV

LIST OF FIGUREURES VII

LIST OF TABLES X

1. INTRODUCTION 1

1.1 Background 1

1.2 Literature Review 4

1.2.1 Track surface deformation induced by freeze-thaw 4

1.2.2 Model for freeze-thaw 5

1.2.3 Model for train vibration 6

1.2.4 Model for track settlement 7

1.3 Thesis Objectives 8

1.4 Thesis Organization 9

2. FREEZE-THAW ANALYSIS OF BALLASTED TRACK 11

2.1 Model Definition 11

2.2 Governing Equation 13

2.3 Parameters and Boundary Conditions 14

2.3.1 Modeling of frost heave 15

2.3.2 Modeling of thaw settlement 15

2.3.3 Boundary temperature setting 15

3. TRAIN VIBRATION ANALYSIS ON BALLASTED TRACK DURING FREEZE-THAW 18

3.1 Vehicle Model 18

3.2 Wheel-rail Contact Model 22
3.3 Substructure Model 23
3.3.1 Rail model 23
3.3.2 Local stiffness and damping matrices of the rail 26
3.3.3 Local stiffness and damping matrices of sleeper and ballast 27
3.4 Model Validation 34
3.4.1 The peak wheelset acceleration due to dipped Joint 35
3.4.2 The peak ballast acceleration due to jagged joint 37
4. RESULTS OF FREEZE-THAW ANALYSIS 40
4.1 Influence of Temperature 40
4.2 Influence of GWL 42
4.3 Evaluation of Amplitude and Wavelength 47
4.4 Summary of This Chapter 50
5. RESULTS OF TRAIN VIBRATION ANALYSIS 51
5.1 Safety Evaluation 51
5.1.1 Minimum vertical wheel-rail force 51
5.1.2 Maximum vertical wheel-rail force 53
5.1.3 Wheel load reduction rate 54
5.2 Stability Evaluation 55
5.2.1 Car body acceleration 55
5.2.2 Sperling Index 57
5.3 Summary of This Chapter 59
6. DIFFERENTIAL PLASTIC DEFORMATION OF BALLASTED TRACK UNDER CYCLIC LOADS 60
6.1 Differential Track Settlement Calculation 61

6.2 Stress below Sleeper under Different Train Speed and GWL 65
6.3 Influence of Different Train Speed on Ballast Settlement 65
6.4 Summary of This Chapter 67
7. CONCLUSIONS AND RECOMMENDATIONS 68
7.1 Conclusions and Recommendations 68
7.2 Future Assignments 69
LIST OF REFERENCES 71
LIST OF NOTATIONS 78
APPENDIX 82

LIST OF FIGUREURES

Figure 1-1 Diagram of vertical heave of highway (After Zhang, Y et al., 2018) 2

Figure 1-2 Formation of ice lens and frost heave in pavement.....2

Figure 1-3 Diagram of freeze-thaw induced track crack (After Tong, F et al., 2019) ...3

Figure 1-4 Diagram of freeze-thaw induced track deformation 3

Figure 1-5 Flowchart of this study.....10

Figure 2-1 Model diagram (a) Size of buried structure (b) Model of culvert transition section 11

Figure 2-2 Variation of boundary temperature in one year.....17

Figure 3-1 Vehicle model.....18

Figure 3-2 Timoshenko Beam Model (Sun et al., 2002).....23

Figure 3-3 Beam element and its local coordinate systems: physical coordinates x, and natural coordinates ξ. (Eugenio, 2016) 24

Figure 3-4 Substructure model.....27

Figure 3-5 Model diagram (a) model of the ballast under one rail support point (b) The longitudinal section of ballasted track (after Zhai et al., 2004) 29

Figure 3-6 Schematic diagram of ballasted track structure (Yang et al., 2021; Sayeed et al., 2018).....29

Figure 3-7 Flowcharts of vehicle-track model program 34

Figure 3-8 The diagram of dipped joint.....36

Figure 3-9 Max wheelset acceleration under different train speed.....36

Figure 3-10 The diagram of jagged joint 37

Figure 3-11 Max ballast acceleration under different train speed.....38

Figure 3-12 Diagram of simulation condition 38

Figure 4-1 Change in vertical displacement of points A and B with surface temperature in one year (GWL=13m, Box culvert) 41

Figure 4-2 Temperature contour of the box culvert transition section (Day 120, GWL=13m) 41

Figure 4-3 The surface deformation of pipe culvert transition section under different GWL (Day 120) 43

Figure 4-5 Total track surface deformation of surface in the freezing period (Day 120): (a) Box culvert (b) Pipe culvert 45

Figure 4-6 Relative track surface deformation of surface in the freezing period (Day 120): (a) Box culvert (b) Pipe culvert 45

Figure 4-7 Total track surface deformation of surface in the thawing period (Day 165): (a) Box culvert (b) Pipe culvert 46

Figure 4-8 Relative track surface deformation of surface in the thawing period (Day 165): (a) Box culvert (b) Pipe culvert 46

Figure 4-9 Total track surface deformation and relative track surface deformation of point A: (a) Freezing period (Day 120) (b) Thawing period (Day 165) 47

Figure 4-10 Fitted results of relative track surface deformation by Eq.10 in the freezing period (Day 120): (a) Box culvert (b) Pipe culvert 48

Figure 4-11 Amplitude and wavelength in the freezing period (Day 120): (a) Box culvert (b) Pipe culvert 49

Figure 4-12 Amplitude and wavelength in the thawing period (Day 165): (a) Box culvert (b) Pipe culvert 49

Figure 5-1 Safety under different GWL (V=300km/h): (a) Decrement of wheel-rail force (b) Max wheel-rail force 52

Figure 5-2 Safety under different train speed (GWL=18m): (a) Decrement of wheel-rail force (b) Max wheel-rail force 52

Figure 5-3 Wheel load reduction rate: (a) under different GWLs (V=300km/h) (b) under different train speeds (GWL=18m) 54

Figure 5-4 Max car body acceleration: (a) under different GWLs (V=300km/h) (b) under different train speeds (GWL=18m) 56

Figure 5-5 Sperling index: (a) under different GWLs (V=300km/h) (b) under different train speeds (GWL=18m)..... 58

Figure 6-1 Settlement calculation process 60

Figure 6-2 Change in vertical displacement of point A and B with surface temperature 63

Figure 6-3 Change in vertical displacement of point A and B with surface temperature 64

Figure 6-4 Ballast settlement (GWL=18): (a) Ballast settlement in the longitude direction (after first iteration) (b) Ballast settlement (after second iteration) (c) Ballast settlement (after third iteration) 64

Figure 6-5 Stress below sleeper considering frost heave induced track surface deformation (Day 120): (a) Relative track surface deformation (b) Different train speed, GWL=18 (c) Different GWL, V=300km/h..... 65

Figure 6-6 Ballast settlement and track surface deformation (a) Ballast settlement in the longitude direction (GWL=18, Day 150) (b) Ballast settlement plus frost heave induced track surface deformation (GWL=18, Day 150) 66

Figure 6-7 Train operation stability (GWL=18, Day 150) (a) Max car body acceleration (b) Sperling index..... 66

LIST OF TABLES

Table 1-1 Semi-empirical model for accumulative strain of geomaterials 7

Table 2-1 Parameters in THM analysis 16

Table 3-1 Parameters in vehicle-track model 21

Table 3-2 Parameters used in model validation (Zhai et al., 1997) 34

Table 5-1 Criteria of wheel load reduction rate (Zhai 2015; Ishida et al., 1999) 54

Table 5-2 Acceleration controlling criteria 56

Table 5-3 Rating of Sperling index (Xia 2013) 58

Table 6-1 Parameters for UIUC model (Yang et al., 2021) 62

1. INTRODUCTION

1.1 Background

Frost heave is a well-known phenomenon in cold regions. According to statistics, more than 50 percent of land in the northern hemisphere is in cold region and exposed to seasonal climatic change, which leads to the cyclic freeze-thaw of the ground. Accompanying with the freeze-thaw process, the frost heave of subsurface soil often causes severe roughness and cracking of structures like pavements (Figure 1-1, 1-2, 1-3, 1-4). For example, the operation experience of the Harbin-Dalian high-speed railway shows that subgrade frost heave makes it difficult to maintain the stability and safety of vehicles.

Frost heave may happen in the wet clayey ground during winter in seasonally frozen regions and during autumn to winter in active layers in permafrost regions. The railway track upheaval, which happens in cold regions, is generally understood as due to frost heaving in subgrade layers (Akagawa et al., 2017). Frost heave and thaw subsidence characteristics of frozen soil are the most basic characteristics that distinguish it from general soil. In the process of soil freezing, water migration and ice precipitation are the direct factors for frost heaving, and the amount of water migration in soil mainly depends on three aspects such as soil quality, moisture and temperature. (Yang et al., 2020).

Experts and scholars have carried out a series of theoretical and experimental research work on the engineering characteristics of frozen soil, the theory of soil frost heave, the anti-frost heave structure of railway subgrade and preventive measures, and have achieved rich results and a lot of experience.

At present, the research on the frost heave of high-speed railway subgrade at home and abroad mainly focuses on the mechanism and prevention measures of frost heave. In present, there are few studies on the influence of frost heave induced ballasted track deformation on the train vibration and its evaluation, and related research work is urgently needed.

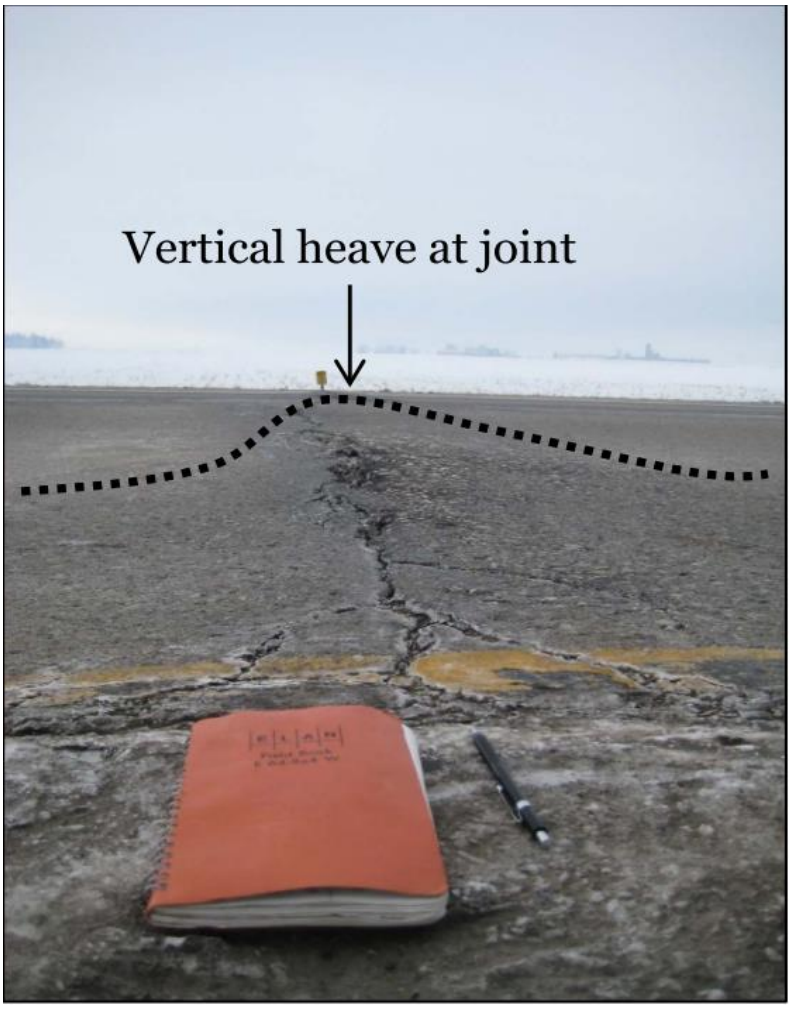

Figure 1-1 Diagram of vertical heave of highway (After Zhang, Y et al., 2018)

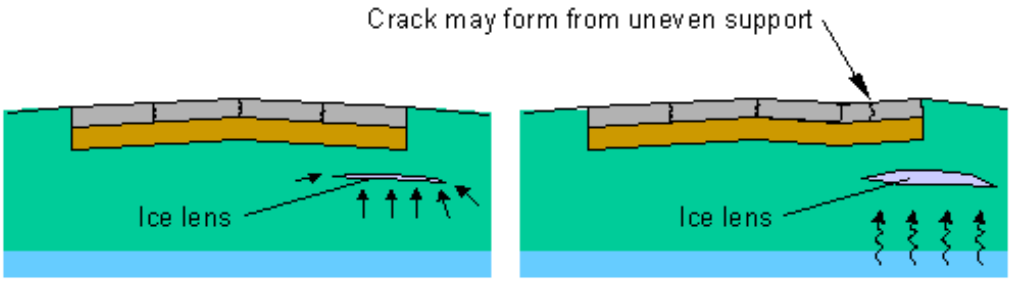

Figure 1-2 Formation of ice lens and frost heave in pavement

Figure 1-3 Diagram of freeze-thaw induced track crack (After Tong, F et al., 2019)

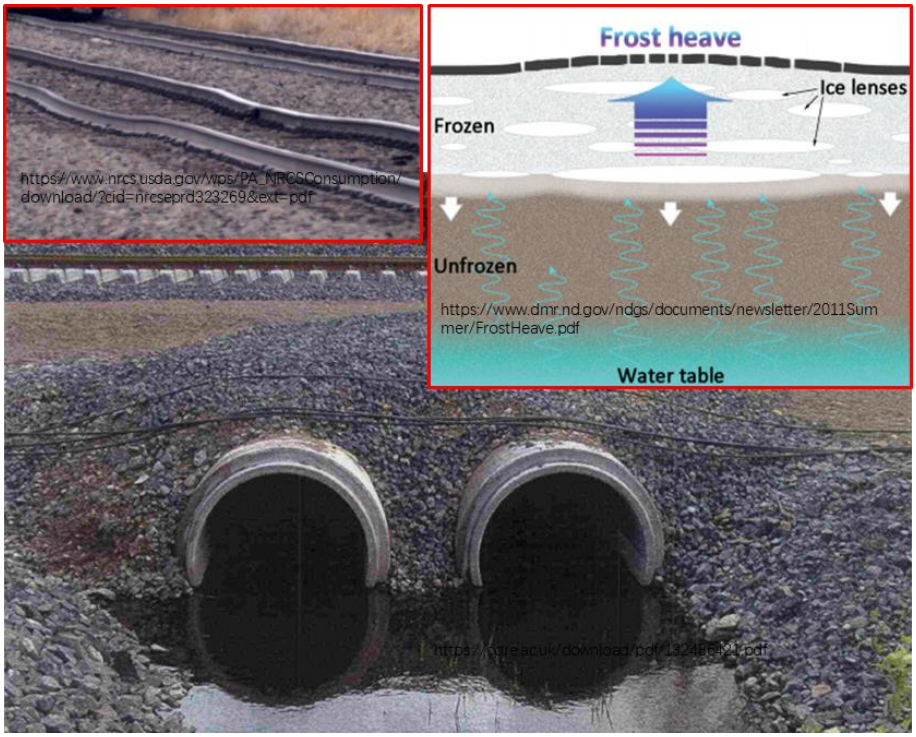

Figure 1-4 Diagram of freeze-thaw induced track deformation

1.2 Literature Review

1.2.1 Track deformation induced by freeze-thaw

A large portion of the land surface on earth is seasonally frozen ground, which may seriously affect the stability of engineered structures due to freeze-thaw process. In cold regions railway engineering, the freeze-thaw of subgrade layer has a significant influence on the railway structure. For example, the recent built Harbin-Dalian and Lanzhou-Xinjiang high-speed railway in China have a significant portion of track foundation located on seasonally frozen ground (Lin et al., 2018, Zhang et al., 2016) It has been reported that wide-spread frost heave was observed during the first winter of their operation, and the heave occurred mainly in coarse-grained fills that were typically considered non-frost susceptible (Zhang et al., 2016). In addition, it has also been shown that the frost heave which deforms railway track not only occurred in subgrade layers but also in the ballast layers if they contain frost susceptible fine materials. Akagawa et al. (2017) present that if the ballast layer contains fines such as clay and/or silt, which are commonly frost susceptible materials, it may vertically expand by frost heaving in winter.

To limit frost heave in railway engineering, researches have been mainly focused on controlling fine particle content, soil moisture content, and lowering the groundwater table. According to Niu et al. (2017), the ground temperatures, frost heave, and moisture content in 2013–2014 were examined at two sites along the embankment of the Harbin-Dalian Passenger Dedicated Line railway. They concluded that the frost heave of embankment due to temperature and moisture variation should be critically considered when designing and constructing railways in seasonally frozen regions. Zhang et al. (2016) presented a likely explanation for the unexpected frost heave, which can be attributed to the combination of different mechanisms (e.g., bottom-up water supply). Liu and Wang (2014, 2018) investigated the frost heave in transition section along a high-speed railway. In their corresponding study, temperature distribution, variable characteristics, and track settlement of roadbed surrounding the culvert were analyzed by site monitoring and numerical simulation.

1.2.2 Model for freeze-thaw

In addition, a number of studies were conducted to simulate the behavior of freeze-thaw for soil (Ishikawa et al., 2016; Ishikawa et al., 2014; Tai et al., 2017; Wu et al., 2018). For instance, to study subgrade frost heave and anti-frost heave measures, Tai et al. (2017) established a moisture-heat coupling differential equation for frozen soils and realized a coupling of the temperature and moisture fields of frozen soils. Rempel et al. (2004) develop a simple model describing the formation and evolution of the ice lenses that drive heave, based on integral force balances. Their model describe the fundamental interactions between phase change and fluid flow in partially frozen, saturated porous media (soils) that are responsible for frost heave. Ishikawa et al. (2016, 2014) presented numerical simulations of the frost heave phenomenon in pavement structure by conducting coupled thermo-hydro-mechanical (THM) finite element (FE) analysis, which reproduces frost heave of soils under unsaturated conditions based on the results of frost heave tests. Nishimura et al. (2009) presented a fully coupled thermo-hydro-mechanical (THM) finite element (FE) formulation considering freezing and thawing in water-saturated soils. Important frozen soil features such as temperature and porosity dependence of shear strength are captured inherently by the model. Liu et al. (2019) presented a fully coupled thermo-hydro-mechanical model in the theory of poroelasticity and a porosity rate function aiming to predict frost heave, temperature distribution, and pore water pressure in frost-susceptible soils. Amiri et al. (2021) developed a new thermo-hydro-mechanical (THM) model to capture the formation and growth of multiple ice lenses in frozen ground. The non-equilibrium thermodynamic theory was used to derive the coupled transport equations of heat and mass. Fracture mechanics was employed to handle the mechanical requirements for the ice lens position and growth. Dong et al. (2018) established a holistic model to simulate the temperature, stress, and deformation in frozen soil and implement a model to simulate frost heave and stress on water pipelines. Lai et al. (2014) proposed a mathematical model of frost heave with the variables of temperature, porosity and displacement, in which Clapeyron equation is employed as the phase equilibrium condition of water and ice in soil. A comprehensive criterion for the formation and end of new ice lens is presented according to the mechanical and physical characteristics.

1.2.3 Model for train vibration

The running speed and safety operation of trains will be seriously affected due to the frost heave and thaw settlement of high-speed railway subgrade. Furthermore, the wheel-rail contact force acting on the track structure will be increased significantly when it passes these subgrade frost heave areas. Simultaneously, the maintenance work will increase drastically. The vibration of the vehicle-track coupling system becomes intensified with the increase of train speed. It has been shown that the design train speed of the Harbin-Dalian high-speed railway was lowered from 350 to 200 km/h in winter (Cai et al., 2019).

In the winters of 2010 and 2011, several hundred kilometers of the Finnish railway network had decreased speed limits due to frost heave induced rail unevenness (Pylkkänen et al., 2012). Scholars have conducted plentiful research on vehicle dynamics behavior based on the vehicle-track coupling system. Cheli et al. (2011) investigated the excitation mechanisms for the vehicle-track vibrations caused by track unevenness. The results show that the highest critical velocities are the most important factors which are likely to cause high vibration levels. In addition, it was shown that the dynamic phenomena have a great influence on the vehicle's ride comfort performance. The subgrade frost heave is a key factor that limits train speed in cold regions. The influence of frost heave induced track deformation on train vibration has been widely studied in the literatures (Cai et al., 2019; Luo et al., 2017). For example, Cai et al. (2019) investigated train vibration under different speed levels, from the aspects of wavelength and amplitude of the track deformation. In addition, an evaluation of train vibration was conducted in terms of train operation safety and stability. Germonpré (2018) investigated the vibration induced by track unevenness and track stiffness variation. The main conclusion is the observation that the interaction forces due to the track stiffness variation are much lower than those due to track unevenness. Youcef et al. (2013) conducted a dynamic analysis on train-bridge system and investigated the riding comfort while considering the rail irregularities. Dynamic responses of the train under different train speeds were computed with random and non-random rail irregularities. On the other hand, Zhu (2010) and Zhai et al. (2010) investigated the influence of wheel-rail dynamic interaction on the subgrade. The results show that the wheel-rail dynamic interaction induced by track irregularities has

a significant influence on the ground acceleration and displacement.

1.2.4 Model for track settlement

Researchers proposed many semi-empirical model for estimating the accumulative strain of geomaterials (e.g. Sato et al., 1995; Monismith et al., 1975; Qamhia et al., 2016). Monismith et al. (1975) proposed an exponential model for practical application based on the indoor test. On this basis, Li and selig et.al. (1995) theoretically analyzed the soil settlement under road traffic load while considering static strength parameters and the influence of soil type and state is indirectly considered. Thom (2006) describes an analysis approach to predicting the settlement and differential settlement of a railway trackbed under the action of moving train traffic. Qamhia et al. (2016) established the UIUC model to estimate permanent deformation of pavement materials, the result indicates that the UIUC model adequately characterize and predict the performance of pavements under repeated traffic loads. Table 1-1 list several semi-empirical model for estimating the accumulative strain.

Table 1-1 Semi-empirical model for accumulative strain of geomaterials

Researchers	Model	Parameters
Monismith et al., 1975	$S = AN^b$	a, b : regression parameters N: number of load cycles
Sato et al., 1995	$S = \gamma[1\text{-}e^{-\alpha N}] + \beta N$	α, β, γ : regression parameters N: number of load cycles
Hecke et al., 1998	$S = S_0 + \alpha P^3 N$	S_0 : initial settlement P : axle load N : number of load applications α : regression parameters
Selig et al., 1995	$\varepsilon_p = a\left(\frac{\sigma_d}{\sigma_s}\right)^m N^b$	σ_d : deviator stress σ_s : soil static strength N : number of load applications a, b, m: regression parameters
Thom et al. 2006	$S = (\log_{10}(N) - 2.4)^2 (\frac{\sigma_b}{160})(\frac{47}{k})$	N: number of load cycles σ_b: pressure on ballast from sleeper k: subgrade reaction modulus

Qamhia et al., 2016	$\varepsilon_p(N) = AN^B\sigma_d^C SSR^D$	N: number of load cycles A,B,C,D: regression parameters σ_d : applied deviator stress SSR: shear stress ratio

In addition, various constitutive models for granular materials have been developed used in the numerical simulations. (Yang et al; 2021; Iwan, 1967; Okayasu et al., 2014; Niemunis et al., 2005). Iwan (1967) proposed a class of one-dimensional models for the yielding behavior of materials and structures has been examined. This class consists of a collection of ideal slip and elastic elements. As per Yang's (2021) research, the permanent axial deformation of clean and aged ballasts can well predict in CD tests by using subloading surface extension (SSE) model. The validity of SSE model in predicting the permanent deformation of air-dried clean ballast under cyclic loading was verified by comparing the test results with the numerical results (Okayasu et al., 2014). In the simulation, constitutive models can track each cyclic loading process, which is suitable for describing the real deformation characteristics of soil under cyclic loading. However, it is impossible to achieve millions of times calculations due to the traditional small-step integration method, each cyclic loading process needs to be calculated in several steps.

1.3 Thesis Objectives

There is a rare study to investigate the relationship between the freeze-thaw and train vibration. Due to the different geological and geotechnical conditions (e.g., groundwater level, soil physical properties, moisture condition, and the existence of underground structures) along the track line, it can result in track unevenness when the freeze-thaw occurs. For instance, the culvert transition section experiences non-uniform spatial frost heaving and thaw settlement, resulting in track deformation. Luo et al. (2017) studied the influence of frost heave at a culvert transition section of ballasted track on train vibration and gave a preliminary evaluation of the vehicle dynamic behavior. However, Luo et al. (2017) does not investigate the relationship between the influence factor of frost heave and train vibration.

The present study employed a culvert transition section of a ballasted track as the research object. The objective of this study is to qualitatively and quantitatively study the influence of freeze-thaw induced track surface deformation on the train vibration,

and provide effective countermeasures for the train operation management and the controlling of freeze thaw induced track surface deformation.

For this end, in this study, the influences of different groundwater level (GWL), culvert types, and variation of season temperature on track surface deformation during the freeze-thaw were examined by performing freeze-thaw analysis of ballasted track at the culvert transition section.

Second, to investigate the influence of track surface deformation induced by freeze-thaw of subgrade on train operation, a vehicle dynamic analysis was conducted by taking it as an excitation into the vehicle-track model.

Third, the influence of the track surface deformation evaluated from the aspect of wavelength and amplitude on train vibration was evaluated in terms of stability and safety of train operation.

Finally, the influence of the track surface deformation induced by freeze-thaw on the ballast settlement was evaluated.

1.4 Thesis Organization

This dissertation is divided into seven chapters as follows:

Chapter 1 introduces the background, literature review, objectives, and organization of this study.

Chapter 2 introduces the Freeze-thaw analysis, include the definition of track model, governing equations in the thermal field, hydraulic field, and mechanical field, parameters and boundary conditions.

Chapter 3 describes the train vibration analysis on ballasted track during freeze-thaw, separately introduces the vehicle model, wheel-rail contact model, substructure model, model validation and simulation condition.

Chapter 4 discusses the results of freeze-thaw analysis. The results is consist of influence of temperature, influence of GWL, evaluation of amplitude and wavelength.

Chapter 5 discusses the result of train vibration analysis. The discussion was conducted from the safety evaluation and stability evaluation.

Chapter 6 investigated differential plastic deformation of ballasted track under cyclic load. The stress below sleeper and ballast settlement was studied with considering different GWL and train speed.

Chapter 7 summarizes the conclusion obtained in this study.

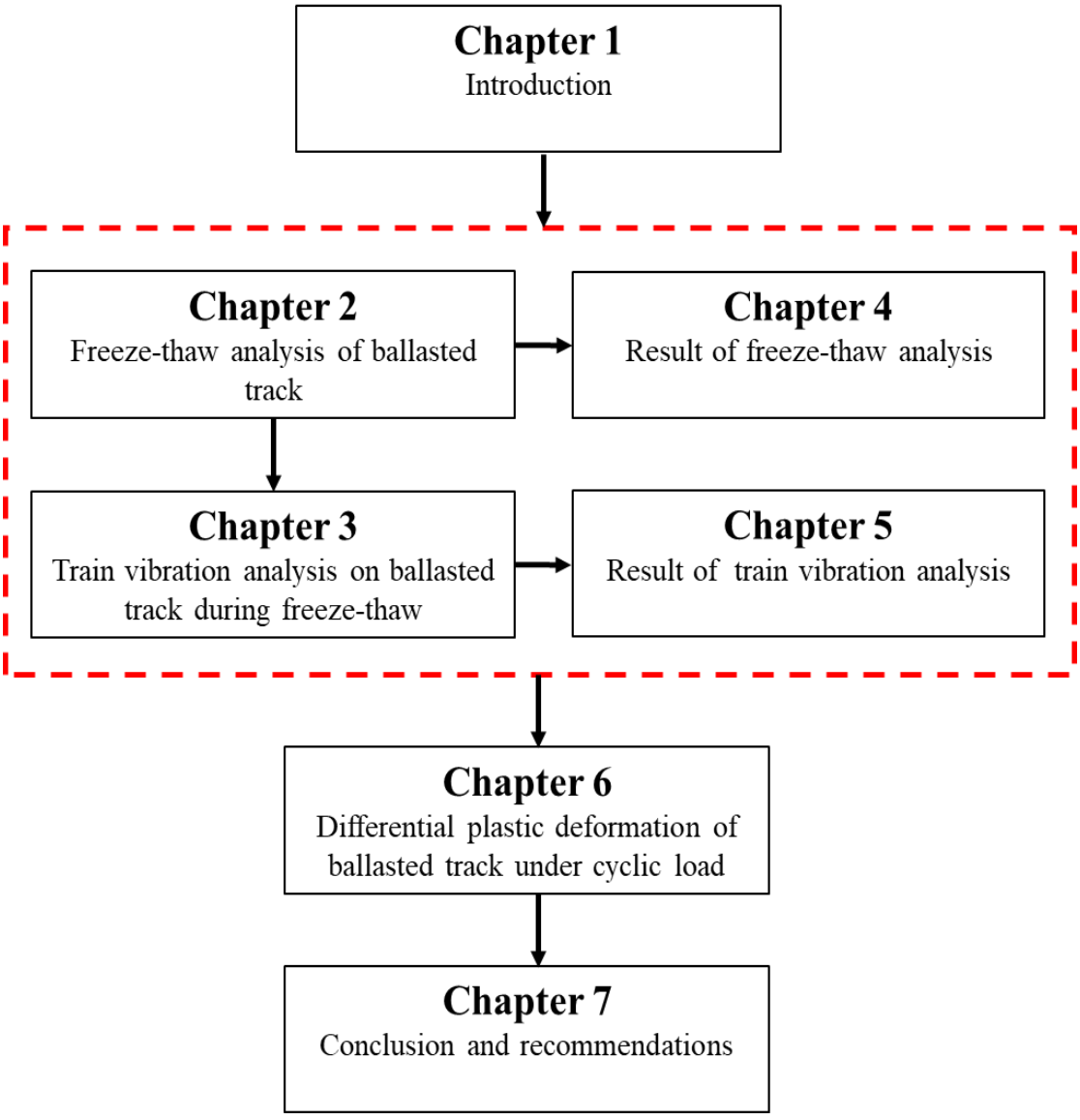

Figure 1-5 Flowchart of this study

2. FREEZE-THAW ANALYSIS OF BALLASTED TRACK

2.1 Model Definition

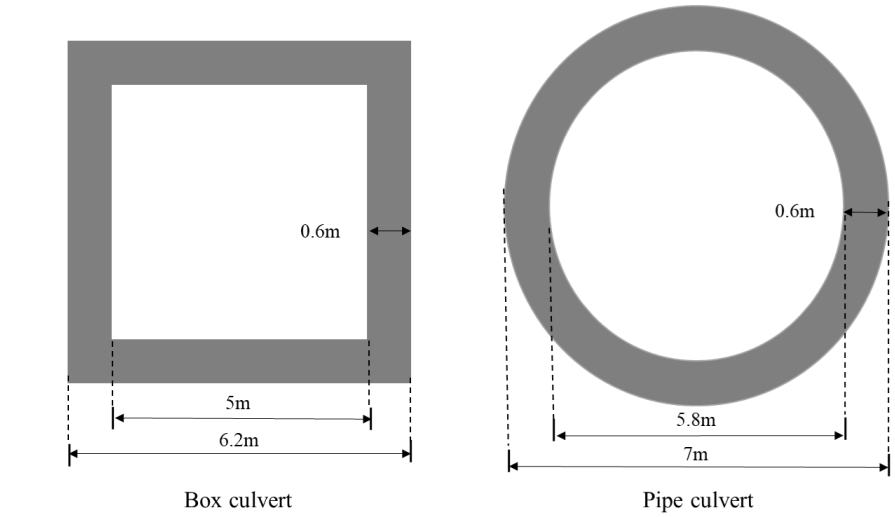

(a)

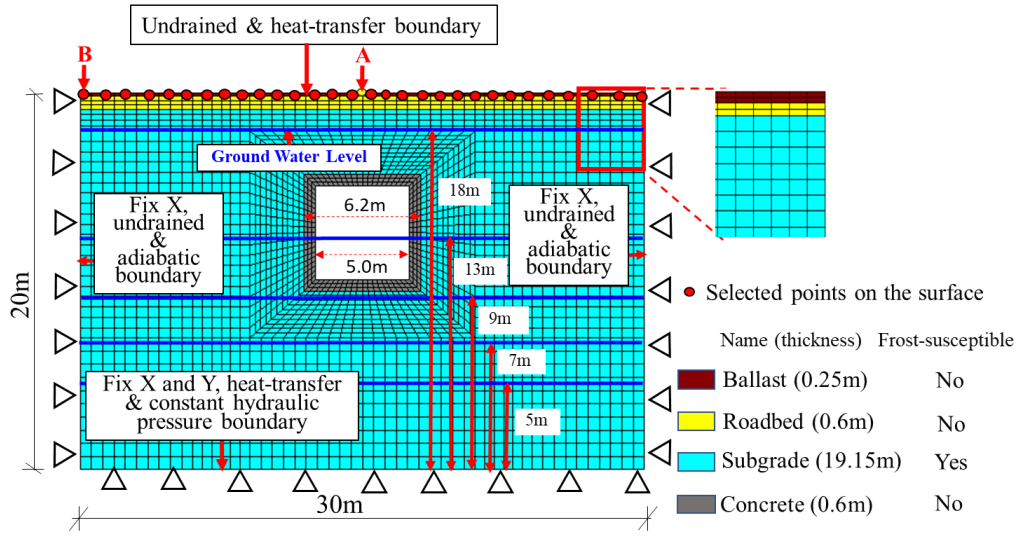

(b)

Figure 2-1 Model diagram (a) Size of buried structure (b) Model of culvert transition section

The culvert transition section will experience non-uniform spatial frost heaving and thaw settlement, resulting in track deformation and affecting train vibration while the train passes the transition section. The present study employed a culvert transition

section of a ballasted track as the research object. The parameters of a typical Hokkaido track are used in this study. To evaluate the influence of different buried structure types, two types of buried structures, the box culvert and the pipe culvert, are studied in this study. Referring to the Road Earthwork and Culvert Construction Guiding Principle (Yatsumoto et al., 2019), a 6.2m×6.2m (external length) box culvert is used in the simulation. For the pipe culvert, the size of the pipe culvert is determined by using the method of area equivalent radius. Namely, the cross-sectional area of the box culvert is equal to the cross-sectional area of the pipe culvert. The thickness was set as 0.6m for both two types of culvert, and their sizes are depicted in Figure 2-1 (a). Two types of culverts have the same buried depth.

As shown in Figure 2-1 (b), a 20m×30m transition section with a culvert (i.e., box culvert and pipe culvert) in the center is built with a thermal-hydro-mechanical (THM) FE model. The model consists of the ballast, roadbed (graded gravel), and subgrade layers. The subgrade is a typical frost-susceptible material found in Hokkaido, i.e., the Touryo soil. The linear elastic stress-strain behavior and non-linear unsaturated water retention relationship are defined in the quadrilateral elements of the mesh. A series of nodes on the surface is selected to monitor the vertical displacement variation. Rainfall is a complex influence factor for the freeze-thaw, only one aspect of rainfall (i.e., change in groundwater level) on the influence of freeze-thaw is considered in this study. In order to investigate the influence of GWL, different GWLs (i.e., 5m, 7m, 9m, 13m, and 18m) are used in the freeze-thaw analysis. The GWL used in this study is defined as the distance from the bottom surface. Note that these values refer to the GWL close to the model bottom, at and below the culvert bottom, at the middle of the culvert, and the average GWL (Fukami et al., 2012) in Hokkaido, respectively. This means that different constant GWLs are considered assuming various locations along a railway line.

As we all know, the measured and in-situ data reflect more realistic conditions but are usually hard to come by. Due to the lack of measured and in-situ data, the current study is based on all the boundary conditions shown in Figure 2. To simplify the analytical procedures, several assumptions are considered: (1) the rail and sleeper are not modeled since their unit weights are much smaller than the dead weight of soil above the frost susceptible subgrade, (2) the ballast, roadbed, and concrete are considered not to cause any frost heave, and only the frost heave of the frost-susceptible

subgrade is considered, (3) the wall of the culvert is assumed to be bond with the fill materials firmly, and the relative motion in the tangential direction is neglected; and (4) the influence of low culvert temperature-induced modulus change and the dependence of subgrade modulus on low temperature are not considered. (5) The track surface deformation is taken as the track deformation induced by freeze-thaw. (6) The influence of buoyancy may exist when the GWL is above the culvert bottom. In current research, the buoyancy of culvert is not considered.

2.2 Governing Equation

The FE analysis was performed using a coupled THM model (Ishikawa et al., 2015; Luo et al., 2017) to predict the freeze-thaw behavior of unsaturated soil. The governing equations for the coupled THM model are written separately in terms of hydraulic, thermal, and mechanical fields as follows.

Mass conservation equation for the hydraulic field is written as:

$$\frac{\partial m}{\partial t} = \frac{1}{K_b}\frac{\partial u_w}{\partial t} + S_w n \alpha_{Tw}\frac{\partial T}{\partial t} - S_w \frac{\partial \varepsilon_v}{\partial t} \tag{2.1}$$

$$\frac{S_w - S_{rr}}{S_{rs} - S_{rr}} = \left[1 + (\alpha\psi)^{\lambda}\right]^{\frac{1-\lambda}{\lambda}} \tag{2.2}$$

$$\frac{\partial \varepsilon_v}{\partial t} = \alpha_{Tu}\frac{\partial T}{\partial t} \tag{2.3}$$

$$k_s = \left(\sigma_m^{'}\right)^a k_0 \tag{2.4}$$

Where m is storage volume of water per unit volume; t is time; K_b is a physical property equivalent to the reciprocal of volume elastic constant of the pore water in the unsaturated region; u_w is pore-water pressure; S_w is degree of saturation for liquid water; n is porosity; α_{Tw} is thermal expansion coefficient of water; T is temperature; ε_v is volumetric strain of soil element; S_{rs} is saturated degree of saturation; S_{rr} is residual degree of saturation; ψ is matric suction; α and λ are Van Genuchten-Mualem fitting parameter; α_{Tu} is thermal expansion coefficient under undrained condition; $\sigma_m^{'}$ mean

effective stress; k_0 is coefficient of water permeability when the mean effective stress equals 0; a is a fitting parameter.

Energy conservation equation for the thermal field is written as:

$$(C_T + L\frac{\partial \theta_i}{\partial T})\frac{\partial T}{\partial t} = \nabla \cdot (-\lambda_T \nabla T) - C_{Tw}\nabla \cdot (v_w T) \tag{2.5}$$

$$\rho = \rho_d + nS_w\rho_w \tag{2.6}$$

Where C_T is volumetric heat capacity of soil; θ_i is volumetric ice content; L is latent heat of fusion of water; λ_T is thermal conductivity of soil; C_{Tw} is volumetric heat capacity of water; v_w is flux vector of water; ρ is wet density of soil; ρ_d is dry density of soil; ρ_w is density of water.

Equilibrium equation for the mechanical field is written as:

$$\frac{\partial \sigma_m}{\partial t} = K\frac{\partial \varepsilon_v}{\partial t} + K_b S_w \frac{\partial m}{\partial t} - K_u \alpha_{Tw}\frac{\partial T}{\partial t} - K_d \frac{\partial \varepsilon_f}{\partial t} \tag{2.7}$$

$$\left(\frac{1}{2}D_{ijkl}\left(\frac{\partial u_{k,l}}{\partial t} + \frac{\partial u_{l,k}}{\partial t}\right) + \frac{\partial \sigma_0}{\partial t}\delta_{ij}\right)_{,j} + \rho g_i = 0 \tag{2.8}$$

Where σ_m is mean total normal stress; K is bulk modulus for the soil structure; K_u is bulk modulus for the soil structure under undrained condition; K_d is bulk modulus for the soil structure under drained condition; ε_f is frost heave or thaw settlement strain; D_{ijkl} is elastic constant tensor; $u_{k,l}$ and $u_{l,k}$ denote displacement tensor; δ_{ij} is Kronecker delta; g_i is acceleration in the i direction.

2.3 Parameters and Boundary Conditions

The freeze-thaw analysis was performed via a coupled THM finite element program (Ishikawa et al., 2015; Luo et al., 2017) to predict the freeze-thaw behavior of unsaturated soil ground. It should be noted that Luo et al. (2017) and Ishikawa et al. (2015) verified the reliability of the finite element program by performing a series of numerical simulations for indoor frost heave tests of the subgrade material in this study. The frost heave tests and its numerical simulations were conducted in accordance with

the standard "Test Method for Frost Heave Prediction of Soils" (JGS 0171-2003) of the Japanese Geotechnical Society (2015). The variation trend of the axial strain and the water absorption and drainage in the freeze-thaw process were investigated under different average initial degrees of saturation (S_0 = 70~100%), different overburden pressure (σ_a = 2.5~100.0 kPa), and different cooling rates (U = 0.2~0.8°C/h). As a result, they showed that under the same experimental conditions, the numerical simulations by FE analysis matched well with the actual test results in the freeze-thaw process, which indicates that the finite element program has high validity and reliability and reasonably reproduces the freeze-thaw behavior of the unsaturated subgrade material.

2.3.1 Modeling of frost heave

Based on the result of frost heave test, the frost expansion strain (ε_f) can be expressed as (Ishikawa et al., 2015; Luo et al., 2017):

$$\varepsilon_f = k_f \left[\frac{\varepsilon_{fmax} S_{w0}}{\varsigma \sigma_n' + 1} + 1.09 m_w \right] \tag{2.9}$$

Where ε_{fmax} is maximum frost expansion strain of saturated soil without overburden pressure; S_{w0} is initial degree of saturation; σ'_n is effective stress at the direction of heat flow; k_f and ς are fitting parameters; m_w is water absorption.

2.3.2 Modeling of thaw settlement

According to results of frost heave test, thaw contraction strain (ε_t) during the thawing process given as (Ishikawa et al., 2015; Luo et al., 2017):

$$\varepsilon_t = \left(c + d \ln \sigma_n \right) \varepsilon_f \tag{2.10}$$

Where σ_n is total stress at the direction of heat flow; c and d are fitting parameters.

2.3.3 Boundary temperature setting

The bottom of the finite element model was set as heat-transfer, constant hydraulic pressure boundary while both horizontal and vertical directions were fixed. The lateral sides were set as undrained and adiabatic boundaries and fixed horizontally. Varying temperature boundary was applied to the ground surface and the outside surface

of the box culvert. Based on long-term air temperature monitoring data, the temperature of the ground surface and culvert (see Figure 2-2) can be simplified into the following sinusoidal function (Andersland et al., 2003; Luo et al., 2017) like Eq. (2.11):

$$T_s = T_m + A \cdot \sin\left[\frac{2\pi(t - t_0)}{p}\right] + \Delta T \tag{2.11}$$

Where T_m is mean annual air temperature. A is surface temperature amplitude. T_m and A are equal to 5.5 and 16.3 degrees Celsius, respectively, as per typical meteorological data in Hokkaido (Luo et al., 2017). t is time (day). p is a corresponding period, 365 days, and t_0 is an initial phase, considered 160 days. ΔT is temperature increment induced by the boundary layer, considered 3 degrees Celsius.

The temperature of the bottom surface (see Figure 2-2) is a function of the ground surface temperature, soil property, and depth. It can be expressed as Eq. (2.12) (Andersland et al., 2003; Luo et al., 2017):

$$T_s = T_m + A \cdot \exp(-z\sqrt{\frac{\pi}{\alpha_u p}}) \cdot \sin(\frac{2\pi(t - t_0)}{p} - z\sqrt{\frac{\pi}{\alpha_u p}}) \tag{2.12}$$

Where z is depth below the air temperature boundary, i.e., from the inner wall of the culvert bottom to the model bottom, and α_u is thermal diffusivity, 3.82×10^{-7} W/m^2 ℃ (Luo et al., 2017).

The values of various material properties included in the THM finite element analysis were obtained from laboratory tests and typical values that were used in previous research (Ishikawa et al., 2015; Ishikawa et al., 2015; Luo et al., 2017; Tokoro et al., 2016). These parameters and values are summarized in Table 2-1. The influence of temperature was not considered on account that the mass, modulus of elasticity and Poisson's ratio of track structures change little at low temperature (Cai et al., 2019). In this study, different constant GWLs are considered in different cases. Before the freeze-thaw analysis, the initial stress state is obtained by a short-term analysis using gravity. Subsequently, the freeze-thaw analysis is performed for 12 months starting from December 1st (shown in Figure 2-2).

Table 2-1 Parameters in THM analysis

Parameters	Ballast	Roadbed	Subgrade	Concrete
Dry density of soil (ρ_d) kg/m^3	1700	2000	1400	2300
Porosity (n)	0.32	0.26	0.45	0.050
Final freezing temperature (T_f) °C	-0.2	-0.2	-0.2	-0.2
Thermal conductivity of soil (λ_T) W/m°C	1.7	0.6	1.61	0.94
Volumetric heat capacity of soil particles (C_T) J/m^3 °C	1.7E6	1.8E6	1.8E6	2.0E6
Van Genuchten-Mualem fitting parameter (α) 1/MPa	846.6	846.6	93.2	—
Van Genuchten-Mualem fitting parameter (λ)	1.36	1.36	1.596	—
Saturated degree of saturation (S_{rs}) %	94.9	94.9	100	—
Residual degree of saturation (S_{rr}) %	23.9	23.9	43.3	—
Permeability(k_s) m/s	5E-4	5E-5	1.0E-8	1.0E-10
Fitting parameter (a)	—	—	1.024	—
Thermal expansion coefficient under undrained condition (α_{Tu}) 1/°C	1E-5	1E-5	1.2E-5	1.0E-5
Young's modulus (E) MPa	300	180	40	21700
Poisson's ratio (υ)	0.35	0.35	0.4	0.2
Fitting parameter (k_f)	—	—	0.749	—
Maximum frost expansion strain (ε_{fmax})	—	—	0.306	—
Fitting parameter (ς) 1/MPa	—	—	28.64	—
Fitting parameter (c)	—	—	1.343	—
Fitting parameter (d) 1/MPa	—	—	0.085	—

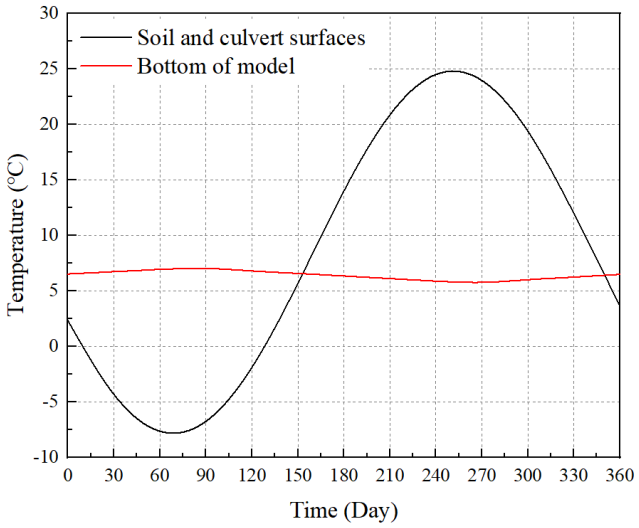

Figure 2-2 Variation of boundary temperature in one year

3. TRAIN VIBRATION ANALYSIS ON BALLASTED TRACK DURING FREEZE-THAW

3.1 Vehicle Model

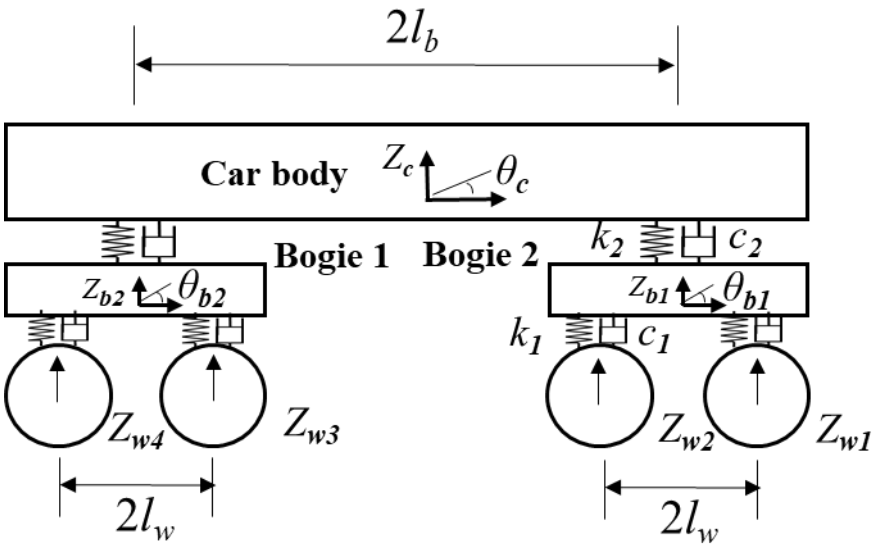

Figure 3-1 Vehicle model

The vehicle-track coupled system is a widely adopted model to conduct train vibration analysis (Guo et al., 2018; Germonpré et al., 2018; Hirotsu et al., 1991; Lei et al., 2002; Luo et al., 2018; Zhai et al., 2010; Zhai 2015; Zhang et al., 2012). Freeze-thaw induced track surface deformation is inputted as the initial displacement on the rail. The car body acceleration and displacement will be obtained as a result of solution. According to field test data, the subgrade frost heave has a significant influence on the vertical track surface deformation while little influence on alignment, gauge, and horizontal level (Cai et al., 2019). For this reason, only the vertical track surface deformation is considered in this study. As the vehicle model is symmetrical along the track, only a half model is considered in this study. As depicted in Figure 3-1, the vehicle model is a ten degree of freedom (DOF) system which consists of car body, two bogies, and two pairs of wheels. Ten degrees of freedom are composed of the vertical displacement of vehicle body, vertical displacement of two bogies, vertical displacement of four wheels, the pitch of two bogies, and the pitch of vehicle body.

Suspensions at all levels are connected by springs and dampers (Ferrara 2014; Zhai 2015). The equation of motion for vehicle can be separately written as:

Car body vertical motion equation:

$$m_c \frac{\partial^2 z_c}{\partial t^2} + c_2\left(\frac{\partial z_c}{\partial t} - \frac{\partial z_{b1}}{\partial t}\right) + c_2\left(\frac{\partial z_c}{\partial t} - \frac{\partial z_{b2}}{\partial t}\right) + k_2(z_c - z_{b1}) + k_2(z_c - z_{b2}) = m_c g \tag{3.1}$$

Car body pitch motion equation:

$$J_c \frac{\partial^2 \theta_c}{\partial t^2} + c_2\left(\frac{\partial \theta_c}{\partial t} l_b + \frac{\partial z_{b1}}{\partial t}\right) l_b + c_2\left(\frac{\partial \theta_c}{\partial t} l_b - \frac{\partial z_{b2}}{\partial t}\right) l_b + k_2(\theta_c l_b + \theta_{b1}) l_b + k_2(\theta_c l_b - \theta_{b2}) l_b = 0 \tag{3.2}$$

Front bogie vertical motion equation:

$$m_b \frac{\partial^2 z_{b1}}{\partial t^2} + (2c_1 + c_2)\frac{\partial z_{b1}}{\partial t} + (2k_1 + k_2)\frac{\partial z_{b1}}{\partial t} - c_2 \frac{\partial z_c}{\partial t} - k_2 z_c - c_1 \frac{\partial z_{w1}}{\partial t} - c_1 \frac{\partial z_{w2}}{\partial t} - k_1 z_{w1} - k_1 z_{w2} + c_2 l_b \frac{\partial \theta_c}{\partial t} + k_2 l_b \theta_c = m_b g \tag{3.3}$$

Front bogie pitch motion equation:

$$J_b \frac{\partial^2 \theta_{b1}}{\partial t^2} + 2c_1 l_w^2 \frac{\partial \theta_{b1}}{\partial t} + 2k_1 l_w^2 \theta_{b1} + c_1 l_w \frac{\partial z_{w1}}{\partial t} - c_1 l_w \frac{\partial z_{w2}}{\partial t} + k_1 l_w z_{w1} - k_1 l_w z_{w2} = 0 \tag{3.4}$$

Rear bogie vertical motion equation:

$$m_b \frac{\partial^2 z_{b2}}{\partial t^2} + (2c_1 + c_2)\frac{\partial z_{b2}}{\partial t} + (2k_1 + k_2)\frac{\partial z_{b2}}{\partial t} - c_2 \frac{\partial z_c}{\partial t} - k_2 z_c - c_1 \frac{\partial z_{w3}}{\partial t} - c_1 \frac{\partial z_{w4}}{\partial t} - k_1 z_{w3} - k_1 z_{w4} - c_2 l_b \frac{\partial \theta_c}{\partial t} - k_2 l_b \theta_c = m_b g \tag{3.5}$$

Rear bogie pitch motion equation:

$$J_b \frac{\partial^2 \theta_{b2}}{\partial t^2} + 2c_1 l_w^2 \frac{\partial \theta_{b2}}{\partial t} + 2k_1 l_w^2 \theta_{b2} + c_1 l_w \frac{\partial z_{w3}}{\partial t} - c_1 l_w \frac{\partial z_{w4}}{\partial t} + k_1 l_w z_{w3} - k_1 l_w z_{w4} = 0 \tag{3.6}$$

The 1_{st} wheel vertical motion equation:

$$m_w \frac{\partial^2 z_{w1}}{\partial t^2} + c_1 \frac{\partial z_{w1}}{\partial t} + k_1 \frac{\partial z_{w1}}{\partial t} - c_1 \frac{\partial z_{b1}}{\partial t} - k_1 z_{b1} + c_1 l_w \frac{\partial \theta_{b1}}{\partial t} + k_1 l_w \theta_{b1} + R_{r/w1}(t) = m_w g \tag{3.7}$$

The 2_{nd} wheel vertical motion equation:

$$m_w \frac{\partial^2 z_{w2}}{\partial t^2} + c_1 \frac{\partial z_{w2}}{\partial t} + k_1 \frac{\partial z_{w2}}{\partial t} - c_1 \frac{\partial z_{b1}}{\partial t} - k_1 z_{b1} + c_1 l_w \frac{\partial \theta_{b1}}{\partial t} + k_1 l_w \theta_{b1} + R_{r/w2}(t) = m_w g \tag{3.8}$$

The 3_{rd} wheel vertical motion equation:

$$m_w \frac{\partial^2 z_{w3}}{\partial t^2} + c_1 \frac{\partial z_{w3}}{\partial t} + k_1 \frac{\partial z_{w3}}{\partial t} - c_1 \frac{\partial z_{b2}}{\partial t} - k_1 z_{b2} + c_1 l_w \frac{\partial \theta_{b2}}{\partial t} + k_1 l_w \theta_{b2} + R_{r/w3}(t) = m_w g \tag{3.9}$$

The 4_{th} wheel vertical motion equation:

$$m_w \frac{\partial^2 z_{w4}}{\partial t^2} + c_1 \frac{\partial z_{w4}}{\partial t} + k_1 \frac{\partial z_{w4}}{\partial t} - c_1 \frac{\partial z_{b2}}{\partial t} - k_1 z_{b2} + c_1 l_w \frac{\partial \theta_{b2}}{\partial t} + k_1 l_w \theta_{b2} + R_{r/w4}(t) = m_w g \tag{3.10}$$

In Figure 3-1, z_c denotes vertical displacement of vehicle body, z_{b1} and z_{b2} respectively denote vertical displacement of bogies. z_{w1}, z_{w2}, z_{w3} and z_{w4} denote vertical displacements of the four wheels, respectively. θ_c, θ_{b1}, θ_{b2} respectively denote the pitch of vehicle body and the pitch of bogies. m_c, m_b, m_w respectively denote car body mass, bogie mass and wheel mass. J_c and J_b respectively denote the car body pitch inertia and bogie pitch inertia. $2l_b$ denote the distance between the bogies pivot points. $2l_w$ denote the wheelbase. $R_{r/w1}$, $R_{r/w2}$, $R_{r/w3}$, $R_{r/w4}$ respectively denote the contact force of 1^{st} , 2^{nd} , 3^{rd} , 4^{th} wheel.

For simplicity, the equation of motion for the vehicle in matrix form is written as:

$$M_v \frac{\partial^2 z_v}{\partial t^2} + C_v \frac{\partial z_v}{\partial t} + K_v z_v - f_{sub/v}(z_v, z_{sub}) = g_v \tag{3.11}$$

Where z_v is vehicle displacement vector; z_{sub} is substructure displacement vector; M_v is vehicle mass matrix; K_v and C_v respectively denote vehicle stiffness matrix and vehicle damping matrix; $f_{sub/v}$ is forces vector; g_v is gravity matrix.

$$z_v = [z_c;\ \theta_c;\ z_{b1};\ \theta_{b1};\ z_{b2};\ \theta_{b2};\ z_w;\ z_w;\ z_w;\ z_w]_{10\times 1} \tag{3.12}$$

$$q_v = [m_c g;\ 0;\ m_b g;\ 0;\ m_b g;\ 0;\ m_w g;\ m_w g;\ m_w g;\ m_w g]_{10\times 1} \tag{3.13}$$

$$f_{sub/v} = [0;\ 0;\ 0;\ 0;\ 0;\ 0;\ -R_{r/w1};\ -R_{r/w2};\ -R_{r/w3};\ -R_{r/w4}]_{10\times 1} \tag{3.14}$$

$$M_v = diag[m_c\ J_c\ m_t\ J_t\ m_t\ J_t\ m_w\ m_w\ m_w\ m_w]_{10\times 10} \tag{3.15}$$

$$K_v=\begin{bmatrix}
2k_2 & 0 & -k_2 & 0 & k_2 & 0 & 0 & 0 & 0 & 0\\
0 & 2k_2l_b^2 & -k_2l_b & 0 & k_2l_b & 0 & 0 & 0 & 0 & 0\\
-k_2 & -k_2l_b & k_2+2k_1 & 0 & 0 & 0 & -k_1 & -k_1 & 0 & 0\\
0 & 0 & 0 & 2k_1l_w^2 & 0 & 0 & -k_1l_w & k_1l_w & 0 & 0\\
-k_2 & k_2l_b & 0 & 0 & k_2+2k_1 & 0 & 0 & 0 & -k_1 & -k_1\\
0 & 0 & 0 & 0 & 0 & 2k_1l_w^2 & 0 & 0 & -k_1l_w & k_1l_w\\
0 & 0 & -k_1 & -k_1l_w & 0 & 0 & k_1 & 0 & 0 & 0\\
0 & 0 & -k_1 & -k_1l_w & 0 & 0 & 0 & k_1 & 0 & 0\\
0 & 0 & 0 & 0 & -k_1 & -k_1l_w & 0 & 0 & k_1 & 0\\
0 & 0 & 0 & 0 & -k_1 & -k_1l_w & 0 & 0 & 0 & k_1
\end{bmatrix}_{10\times10} \tag{3.16}$$

$$C_v=\begin{bmatrix}
2c_2 & 0 & -c_2 & 0 & c_2 & 0 & 0 & 0 & 0 & 0\\
0 & 2c_2l_b^2 & -c_2l_b & 0 & c_2l_b & 0 & 0 & 0 & 0 & 0\\
-c_2 & -c_2l_b & c_2+2c_1 & 0 & 0 & 0 & -c_1 & -c_1 & 0 & 0\\
0 & 0 & 0 & 2c_1l_w^2 & 0 & 0 & -c_1l_w & c_1l_w & 0 & 0\\
-c_2 & c_2l_b & 0 & 0 & c_2+2c_1 & 0 & 0 & 0 & -c_1 & -c_1\\
0 & 0 & 0 & 0 & 0 & 2c_1l_w^2 & 0 & 0 & -c_1l_w & c_1l_w\\
0 & 0 & -c_1 & -c_1l_w & 0 & 0 & c_1 & 0 & 0 & 0\\
0 & 0 & -c_1 & -c_1l_w & 0 & 0 & 0 & c_1 & 0 & 0\\
0 & 0 & 0 & 0 & -c_1 & -c_1l_w & 0 & 0 & c_1 & 0\\
0 & 0 & 0 & 0 & -c_1 & -c_1l_w & 0 & 0 & 0 & c_1
\end{bmatrix}_{10\times10} \tag{3.17}$$

The influence of temperature was not considered on account that the mass, modulus of elasticity and Poisson's ratio of vehicles and track structures change little at low temperature (Cai et al., 2019). In addition, the rubber pad, sleeper, ballast layer (not fouled, i.e., no fine materials), and roadbed layer (not fouled graded gravel, i.e., no fine materials) are considered as no-frost susceptible material. There is no frozen phenomenon in these materials. So, their stiffness will not change during the freeze-thaw period, and the same input parameters are used for both freezing period and thawing period.

Table 3-1 Parameters in vehicle-track model

Vehicle parameters	
Car body mass (kg)	48000
Bogie mass (kg)	3200
Wheel set mass (kg)	2400

Vertical stiffness of primary suspension (N/m)	1.04×10^6
Vertical stiffness of secondary suspension (N/m)	0.4×10^6
Vertical damping of primary suspension (Ns/m)	4.5×10^4
Vertical damping of secondary suspension (Ns/m)	5×10^4
Substructure parameters	
Rubber pad stiffness (N/m)	6.5×10^7
Rubber pad damping (Ns/m)	7.5×10^4
Sleeper mass (kg)	251
Width of sleeper underside (m)	0.33
Mass of vibrating ballast (kg)	341.5
Ballast stress distribution angle (deg)	35
Sleeper spacing (m)	0.6
Ballast density (kg/m^3)	1.8×10^3
Young's modulus of ballast (N/m^2)	3.0×10^8
Vertical ballast stiffness (N/m)	3.51×10^8
Vertical ballast damping (Ns/m)	58.8×10^3
Horizontal ballast stiffness (N/m)	1.12×10^8
Horizontal ballast damping (Ns/m)	17.64×10^3
Roadbed stiffness (N/m)	6.5×10^7
Roadbed damping (Ns/m)	3.12×10^4

3.2 Wheel-rail Contact Model

The wheel-rail forces between the wheel and rail are computed by the non-linear Hertz model (Lei et al., 2002; Zhai 2015).

$$R_{w/r}=\begin{cases}k_h z_h^{3/2} & (z_h>0)\\ 0 & (z_h<0)\end{cases} \tag{3.18}$$

$$z_h = z_{wj} - z_{rj} - z_{rdj} \tag{3.19}$$

Where z_h is the total deflection of wheel and rail at the contact point; k_h is the Hertzian contact stiffness coefficient. Z_{wj} is vertical displacement of the j^{th} wheel, Z_{rj} vertical displacement of the rail at the contact point, Z_{rdj} is vertical defect of the rail at the contact point.

3.3 Substructure Model

3.3.1 Rail model

According to the study of Ferrara (2014), the rail is applicable for "thick" beams and modeled as a Timoshenko beam connected to pads as shown in Figure 3-2. A finite element method is used to model the rail. Considering the insignificant axial displacement, the rail is discretized with finite beam elements with two degrees of freedom for every node: rotation (θ) and vertical displacement (v). The algorithm allows choosing the number of beam elements between two sleepers and the number of beam elements vertically connected to the sleeper by pads.

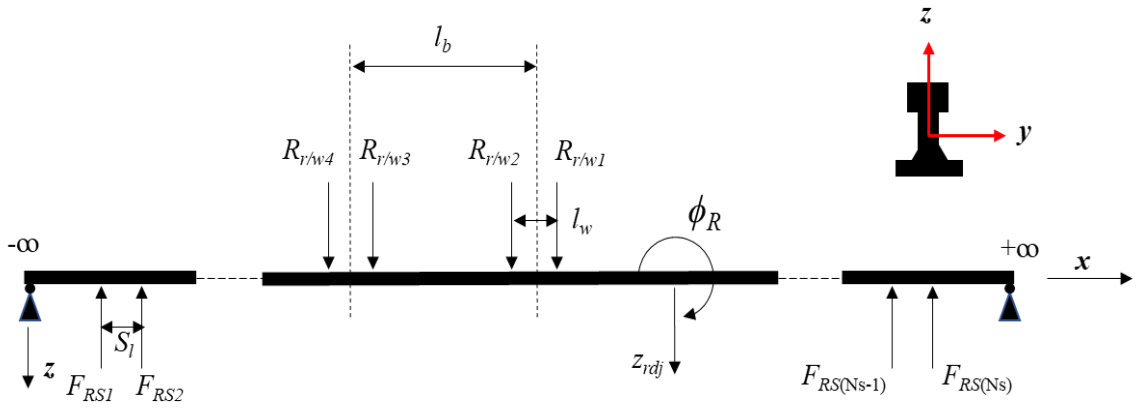

Figure 3-2 Timoshenko Beam Model (Sun et al., 2002)

Finite beam Elements are two-node Timoshenko finite beam elements as shown in Figure 3-3. Only vertical displacement ($v=z_{rdj}$) and rotation ($\theta=\phi_R$) at nodes is considered. Axial deformation has been neglected.

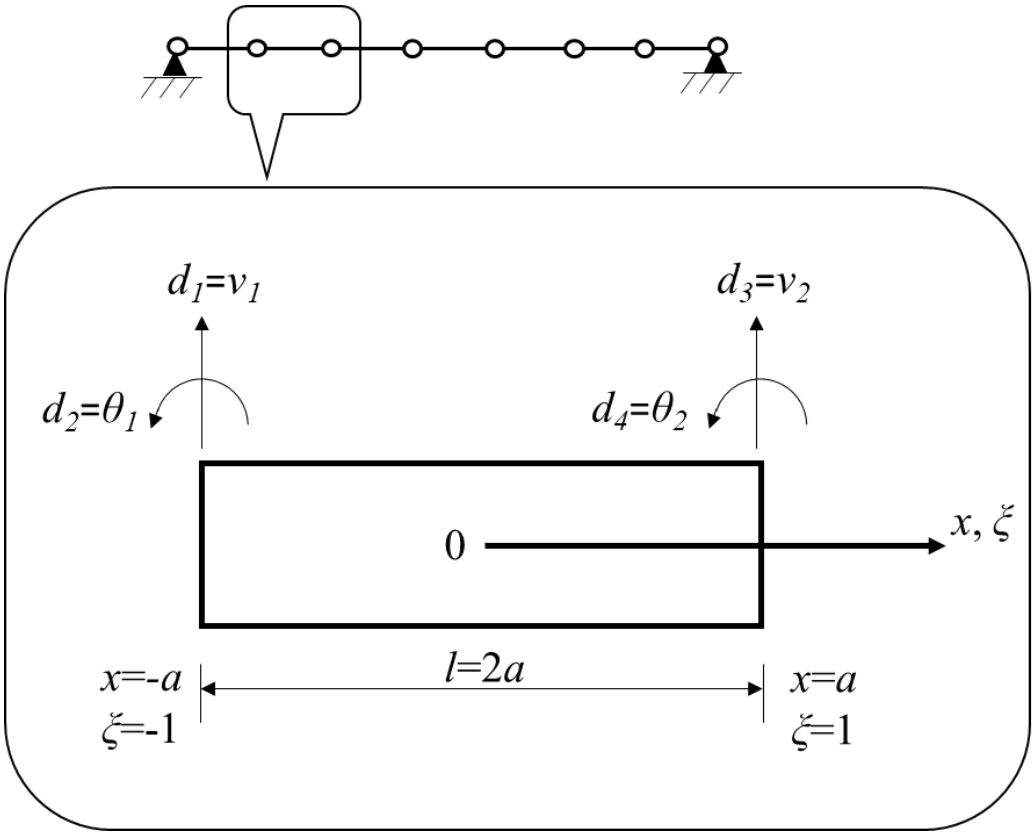

Figure 3-3 Beam element and its local coordinate systems: physical coordinates x, and natural coordinates ξ. (Eugenio, 2016)

The bending strain ε_{xx} and the transverse shear strain γ_{xz} are expressed as:

$$\varepsilon_{xx} = \frac{d\theta}{dx} = \frac{\partial N_r}{\partial X} S = \mathrm{B}_b S \tag{3.20}$$

$$\gamma_{xz} = \frac{d\theta}{dx} - \theta = (\frac{\partial N_b}{\partial X} - N_r) S = \mathrm{B}_s S \tag{3.21}$$

$$S^T = \left[v_1,\ \theta_1,\ v_2,\ \theta_2 \right] \tag{3.22}$$

The shape functions vector due to bending (N_b) is written as:

$$N_b = \left[n_{b1},\ n_{b2},\ n_{b3}, n_{b4} \right] \tag{3.23}$$

$$n_{b1} = \frac{1}{1+\phi}(1 + 2\xi^3 - 3\xi^2 + \phi(1-\xi)) \tag{3.24}$$

$$n_{b2} = \frac{1}{1+\phi}(\xi + \xi^3 - 2\xi^2 + \frac{\phi}{2}(\xi - \xi^2)) \tag{3.25}$$

$$n_{b3} = \frac{1}{1+\phi}(-2\xi^3 + 3\xi^2 + \phi\xi) \tag{3.26}$$

$$n_{b4} = \frac{1}{1+\phi}(\xi^3 - \xi^2 + \frac{\phi}{2}(\xi^2 - \xi)) \tag{3.27}$$

$$\phi = \frac{12}{l^2}\frac{EI}{GA\chi} \tag{3.28}$$

Where, A is the rail section area, G is the shear modulus, I is the bending inertia, E is the rail modulus, l is the length of beam element (in this case, l = 2a), χ (=0.34) is the Timoshenko Beam Coefficient (Ferrara, 2014). The shape functions vector due to rotation (N_r) is written as:

$$N_r = \left[n_{r1},\ n_{r2},\ n_{r3}, n_{r4}\right] \tag{3.29}$$

$$n_{r1} = \frac{6}{(1+\phi)l}(\xi - \xi^2) \tag{3.30}$$

$$n_{r2} = \frac{1}{1+\phi}(3\xi^2 - 4\xi + 1 + \phi(1-\xi)) \tag{3.31}$$

$$n_{r3} = \frac{1}{(1+\phi)l}(6\xi - 6\xi^2) \tag{3.32}$$

$$n_{r4} = \frac{1}{1+\phi}(3\xi^2 - 2\xi + \phi\xi) \tag{3.33}$$

The element stiffness matrix is:

$$K_e = K_b + K_s \tag{3.34}$$

$$K_b = \int_V B_b^T E B_b dA dx \tag{3.35}$$

$$K_s = \int_V B_s^T E B_s dA dx \tag{3.36}$$

The element stiffness and mass matrix can be written as:

$$K_e = \frac{EI}{l^3(1+\phi)}\begin{bmatrix} 12 & 6l & -12 & -6l \\ 6l & (4+\phi)l^2 & -6l & (2-\phi)l^2 \\ -12 & -6l & 12 & -6l \\ 6l & (2-\phi)l^2 & -6l & (4+\phi)l^2 \end{bmatrix} \tag{3.37}$$

$$M_e = \begin{bmatrix} \frac{13}{35}l+\frac{7}{10}l\phi+\frac{l\phi^2}{3} & \frac{11}{210}l^2+\frac{11}{120}l^2\phi+\frac{l^2\phi^2}{24} & \frac{9}{70}l+\frac{3}{10}l\phi+\frac{1}{6}l\phi^2 & -\frac{13}{420}l^2-\frac{3}{40}l^2\phi-\frac{1}{24}l^2\phi^2 \\ \frac{11}{210}l^2+\frac{11}{120}l^2\phi+\frac{l^2\phi^2}{24} & \frac{1}{105}l^3+\frac{1}{60}l^3\phi+\frac{l^3\phi^2}{120} & \frac{13}{420}l^2+\frac{3}{40}l^2\phi+\frac{l^2\phi^2}{24} & -\frac{1}{140}l^3-\frac{1}{60}l^3\phi-\frac{l^3\phi^2}{120} \\ \frac{9}{70}l+\frac{3}{10}l\phi+\frac{1}{6}l\phi^2 & \frac{13}{420}l^2+\frac{3}{40}l^2\phi+\frac{l^2\phi^2}{24} & \frac{13}{35}l+\frac{7}{10}l\phi+\frac{l\phi^2}{3} & -\frac{11}{210}l^2-\frac{11}{120}l^2\phi-\frac{l^2\phi^2}{24} \\ -\frac{13}{420}l^2-\frac{3}{40}l^2\phi-\frac{1}{24}l^2\phi^2 & -\frac{1}{140}l^3-\frac{1}{60}l^3\phi-\frac{l^3\phi^2}{120} & -\frac{11}{210}l^2-\frac{11}{120}l^2\phi-\frac{l^2\phi^2}{24} & \frac{1}{105}l^3+\frac{1}{60}l^3\phi+\frac{l^3\phi^2}{120} \end{bmatrix} \tag{3.38}$$

The damping matrix was evaluated by using Rayleigh's theory as:

$$C_e = \alpha M_e + \beta K_e \tag{3.39}$$

Where, α, β are Rayleigh's coefficients. Ekevid et al. (2001) suggest that α=β=0.005. It was found that the rail offered negligible damping. Damping occurred mainly through rubber pads, sleepers and ballast, so damping of the rail has been neglected in this model.

3.3.2 Local stiffness and damping matrices of the rail

The local stiffness and damping matrix for a beam element not connected to a sleeper can be written as:

$$K_{ij} = K_e, \quad C_{ij} = C_e \tag{3.40}$$

The local stiffness matrix of the beam element connected to a sleeper in the first node can be written as:

$$K_{sj} = K_e + \frac{k_p}{n}\begin{bmatrix} 1 & 0 & 0 & 0 \\ 0 & 0 & 0 & 0 \\ 0 & 0 & 0 & 0 \\ 0 & 0 & 0 & 0 \end{bmatrix}, \qquad C_{sj} = C_e + \frac{c_p}{n}\begin{bmatrix} 1 & 0 & 0 & 0 \\ 0 & 0 & 0 & 0 \\ 0 & 0 & 0 & 0 \\ 0 & 0 & 0 & 0 \end{bmatrix} \tag{3.41}$$

The local stiffness and damping matrix for a beam element connected to a sleeper in the last node can be written as:

$$K_{is} = K_e + \frac{k_p}{n}\begin{bmatrix} 0 & 0 & 0 & 0 \\ 0 & 0 & 0 & 0 \\ 0 & 0 & 1 & 0 \\ 0 & 0 & 0 & 0 \end{bmatrix}, \qquad C_{is} = C_e + \frac{c_p}{n}\begin{bmatrix} 0 & 0 & 0 & 0 \\ 0 & 0 & 0 & 0 \\ 0 & 0 & 1 & 0 \\ 0 & 0 & 0 & 0 \end{bmatrix} \tag{3.42}$$

The local stiffness and damping matrix for a beam element on top of sleeper can be written as:

$$K_{ss} = K_e + \frac{k_p}{n}\begin{bmatrix} 1 & 0 & 0 & 0 \\ 0 & 0 & 0 & 0 \\ 0 & 0 & 1 & 0 \\ 0 & 0 & 0 & 0 \end{bmatrix}, \qquad C_{ss} = C_e + \frac{c_p}{n}\begin{bmatrix} 1 & 0 & 0 & 0 \\ 0 & 0 & 0 & 0 \\ 0 & 0 & 1 & 0 \\ 0 & 0 & 0 & 0 \end{bmatrix} \tag{3.43}$$

Where k_p and c_p are the rubber pad stiffness and damping constants and n is the number of the beam elements represented by area-contact model. The rail between two sleepers is considered as one beam, and the sleeper interval is 0.6 m. There are 15 beam elements in one sleeper interval (0.6 m). In this case, the length of beam element is 4cm.

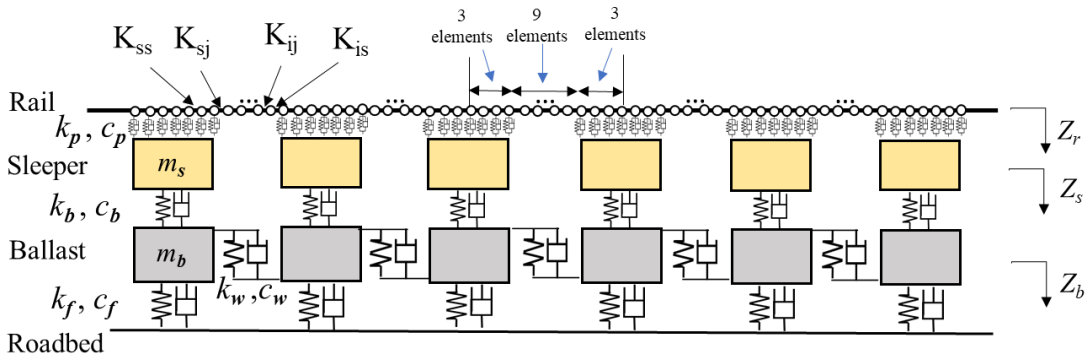

Figure 3-4 Substructure model

3.3.3 Local stiffness and damping matrices of sleeper and ballast

The load transmitting from a sleeper to the ballast approximately coincides with the cone distribution (Zhai 2015). The vibrating mass of ballast under each sleeper (Zhai 2015; Zhai 2004) can be evaluated by Eq. (3.44), as shown in Figure 3-5.

$$M_b = \rho_b \left[h_b l_b \left(l_e + h_b \tan\alpha \right) + l_e \left(h_b^2 - h_0^2 \right) \tan\alpha + \frac{4}{3} \left(h_b^3 - h_0^3 \right) \tan^2 \alpha \right] \tag{3.44}$$

$$h_0 = h_b - \frac{l_s - l_b}{2 \tan\alpha} \tag{3.45}$$

Where l_s is sleeper spacing. ρ_b is density of ballast, h_b is thickness of ballast, l_e is effective supporting length of half sleeper ($l_e = 2l'$, Figure 3-6), l_b is width of sleeper underside, and φ is ballast stress distribution angle (Zhai 2015; Zhai 2004).

The supporting stiffness of a ballast mass can be evaluated as (Zhai 2015; Zhai 2004):

$$K_b = \frac{K_{b1} K_{b2}}{K_{b1} + K_{b2}} \tag{3.46}$$

$$K_{b1} = \frac{2(l_e - l_b) tg\alpha}{\ln[(l_e l_s) / (l_b (l_e + l_s - l_b))]} E_b \tag{3.47}$$

$$K_{b2} = \frac{l_s (l_s - l_b + 2l_e + 2h_b tg\alpha) tg\alpha}{l_b - l_s + 2h_b tg\alpha} E_b \tag{3.48}$$

Where E_b is Young's modulus of ballast. The horizontal ballast stiffness is obtained by multiplying vertical ballast stiffness by a factor of 0.3.

The roadbed stiffness can be calculated as the product of cone base area and roadbed modulus,

$$K_f = l_s (l_e + 2h_b tg\alpha) E_f \tag{3.49}$$

Where E_f is the K_{30} modulus of roadbed. Other substructure parameters are listed in Table 3-1 (Zhai 2015; Zhai 2004).

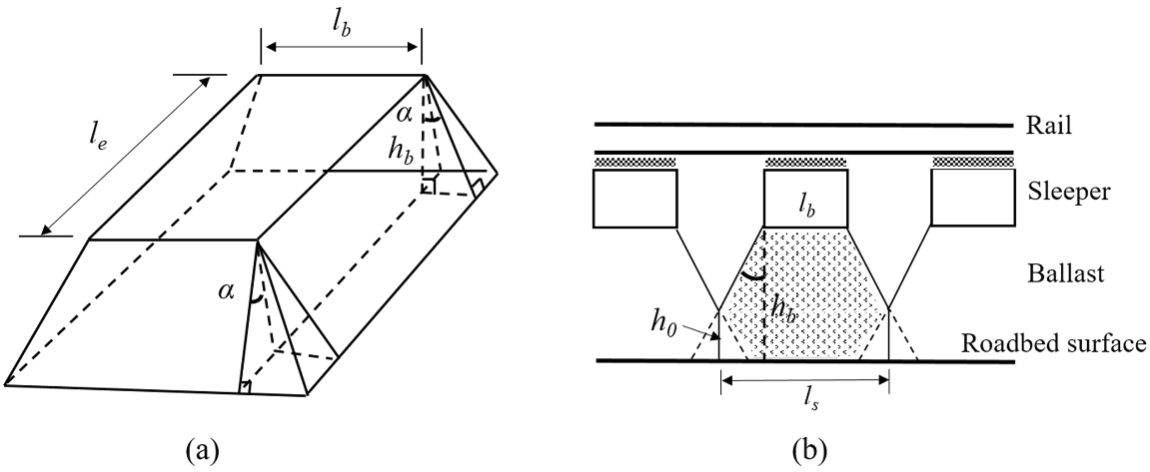

Figure 3-5 Model diagram (a) model of the ballast under one rail support point (b) The longitudinal section of ballasted track (after Zhai et al., 2004)

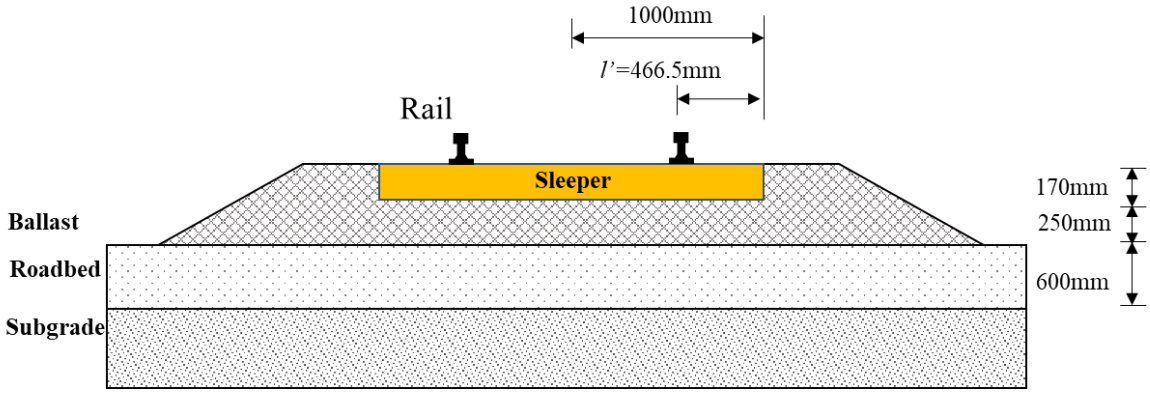

Figure 3-6 Schematic diagram of ballasted track structure (Yang et al., 2021; Sayeed et al., 2018)

Let n be the number of rail nodes and m be the number of sleepers in the track section considered. Then, assembled mass and stiffness matrix of the substructure is:

$$M_s = diag\left[m_s \ \ldots m_s\right]_{m\times m}, \quad K_s = diag\left[k_b + k_p \ \ldots k_b + k_p\right]_{m\times m} \tag{3.50}$$

$$M_b = diag\left[m_b \ \ldots m_b\right]_{m\times m}, \quad \mathrm{K}_b = \begin{bmatrix} k'_{wbf} & -k_w & 0 & \ldots & \ldots & \ldots & 0 \\ -k_w & k_{wbf} & -k_w & 0 & \ldots & \ldots & 0 \\ 0 & -k_w & k_{wbf} & -k_w & 0 & \ldots & 0 \\ \vdots & 0 & -k_w & \ddots & \ddots & \ddots & \vdots \\ \vdots & \vdots & 0 & \ddots & \ddots & \ddots & 0 \\ \vdots & \vdots & \vdots & \ddots & \ddots & k_{wbf} & -k_w \\ 0 & 0 & 0 & \ldots & 0 & k'_{wbf} & k'_{wbf} \end{bmatrix}_{m\times m} \tag{3.51}$$

Where,

$$k'_{wbf} = k_w + k_b + k_f, \quad k_{wbf} = 2k_w + k_b + k_f \tag{3.52}$$

The substructure consists of rail, rubber pad, sleeper mass, and ballast mass. As shown in Figure 3-4, the sleeper and rail are connected by a series of stiffness and damping supplied from the rubber pad. To consider the propagation of vibration along the track direction, the shear force is provided by a horizontal spring. The equation of motion for substructure is written as:

$$M_{sub}\frac{\partial^2 z_{sub}}{\partial t^2} + C_{sub}\frac{\partial z_{sub}}{\partial t} + K_{sub}z_{sub} - f_{v/sub}\left(z_v, z_{sub}\right) = \mathrm{g}_{sub} \tag{3.53}$$

Where z_{sub} is substructure displacement vector; M_{sub} is substructure mass matrix; K_{sub} and C_{sub} respectively denote substructure stiffness matrix and damping matrix; $f_{v/sub}$ is forces vector; g_{sub} is gravity matrix; all the parameters used in substructure model are listed in Table 3-2 (Cai et al., 2019; Zhai et al., 2004; Zhai 2015; Zhang et al., 2012). In Figure 3-4, k_p, k_b, k_g and k_w respectively denote rubber pad stiffness, ballast stiffness, ground stiffness, and horizontal ballast stiffness. c_p, c_b, c_g and c_w respectively denote rubber pad damping, ballast damping, ground damping and horizontal ballast damping. m_s and m_b denote sleeper mass and ballast mass. The parameters used for the vehicle model can be found in Table 3-1 (Cai et al., 2019; Fu et al., 2017). Z_r, Z_s, Z_b respectively denote the vertical displacement of the rail, sleeper, and ballast. The assembled damping matrix (C_{sub}) of the substructure is same as assembled stiffness matrix (K_{sub}) except substituting k terms with corresponding c terms.

$$M_{sub} = \begin{bmatrix} M_r & 0_{2n\times m} & 0_{2n\times m} \\ 0_{m\times 2n} & M_s & 0_{m\times m} \\ 0_{m\times 2n} & 0_{m\times m} & M_b \end{bmatrix}_{(2n+2m)\times(2n+2m)} \tag{3.54}$$

$$K_{sub} = \begin{bmatrix} K_r & B^T & 0_{2n\times m} \\ B & K_s & D \\ 0_{m\times 2n} & D & K_b \end{bmatrix}_{(2n+2m)\times(2n+2m)} \tag{3.55}$$

$$B = \begin{bmatrix} -k_p & 0 & 0 & 0 & 0 & 0 & \dots & \dots & \dots & 0 \\ 0 & 0 & 0 & 0 & -k_p & 0 & \dots & \dots & \dots & 0 \\ 0 & 0 & 0 & 0 & 0 & 0 & \ddots & \ddots & \ddots & \vdots \\ \vdots & \vdots & \vdots & \vdots & \vdots & \vdots & \ddots & \ddots & \ddots & \vdots \\ 0 & 0 & 0 & 0 & 0 & 0 & \ddots & 0 & -k_p & 0 \end{bmatrix}_{m\times 2n} \tag{3.56}$$

$$D = diag\left[-k_b \dots -k_b\right]_{m\times m} \tag{3.57}$$

$$z_{sub} = \begin{bmatrix} z_r \\ z_s \\ z_b \end{bmatrix}_{(2n+2m)\times 1} \tag{3.58}$$

Where,

$$z_s = \left[z_{s1} \dots z_{si} \dots z_{sm}\right]^T_{m\times 1} \tag{3.59}$$

$$z_b = \left[z_{b1} \dots z_{bi} \dots z_{bm}\right]^T_{m\times 1} \tag{3.60}$$

The assembled column matrix of forces on substructure due to vehicle wheel load can be written as:

$$f_{v/sub} = \begin{bmatrix} f_{v/r} \\ 0 \\ 0 \end{bmatrix}^T_{(2n+2m)\times 1} \tag{3.61}$$

The assembled column matrix of self-weight forces of substructure components

can be written as:

$$g_{sub} = \begin{bmatrix} g_r \\ g_s \\ g_b \end{bmatrix}^T_{(2n+2m)\times 1} \tag{3.62}$$

$$g_s = \left[m_s \ldots m_s \right]^T_{m\times 1} \tag{3.63}$$

$$g_b = \left[m_b \ldots m_b \right]^T_{m\times 1} \tag{3.64}$$

The basic simulation process can be easily understood by Figure 3-7. The process of calculation of safety indices and stability indices including vehicle-track model has been solved using MATLAB. The flowcharts mention the names of actual MATLAB scripts written for the simulation. The model requires inputs from the vehicle, substructure and other simulation parameters to start. In the simulation result, it gives wheel-rail forces, car body acceleration, which the safety and stability parameters can be determined. The main functions of the scripts are as follows:

Main program start: it start the program and calls the following scripts which perform specialized functions. It also plots the results of simulation.

VehicleProperties: In this script, the vehicle properties (the mass of car body and bogie, the primary and secondary stiffness and damping, etc.) are inputted into the model, and other simulation parameters (e.g. length of track) are assigned.

AssigningValues: This script is used for assigning the simulation parameters (e.g. the simulated length of track).

SubstructureProperties: This script is used for ipputing the substructure (rail, pad, sleeper, etc.) are inputted into the model.

VehicleMatrix: The vehicle matrices (i.e. mass matrix, stiffness matrix and damping matrix) are formed by using inputted vehicle properties of the model.

InitialCalculation: According to the inputted simulation and track parameters, the number of step required for simulation, number of sleepers, degrees of freedom of track, rail element size, etc. are calculated in this script.

SubMatrices: For the scripts of **BeamEleMatrix,** it forms local mass and stiffness matrix of an individual beam element which is combined to form global mass and stiffness matrix of rail. Then, the mass, stiffness, and damping matrices of individual of substructure components (e.g. rail, sleeper and ballast) are separately formed and assembled in the script of **SubMassMatrix** and **SubK_C_Matrix**.

PreMatrices: For this script, it is used to forms matrices which are constant. In each simulation step, these matrices are repeatedly used for Newmark-beta numerical integration method.

InitializingNodalDisplacements: In this script, it initializes the matrices and thus allocates memory for more efficiency processing. The initialized matrix are mainly used to store the nodal displacement, velocity and acceleration of both vehicle and substructure model.

MainStepsLoop: The executing times of this script equals the number of steps calculated in **InitialCalculations**. In each step it calculates the position of each wheel of the vehicle in **WheelPos_ShapeFunc** and also the shape functions for beam elements corresponding to wheel positions. The irregularity and track surface deformation are inputted in the script of **RailUnevenness**. In the script of **SubResolveLoop,** it solves the substructure equations of motion simultaneously with non-linear equations of motion of vehicle using Newton-Raphson method.

Acc_SperlingStability: This script is used to calculate the indices of safety and stability. These values are plotted against different freeze-thaw induced track surface deformation and different train speeds.

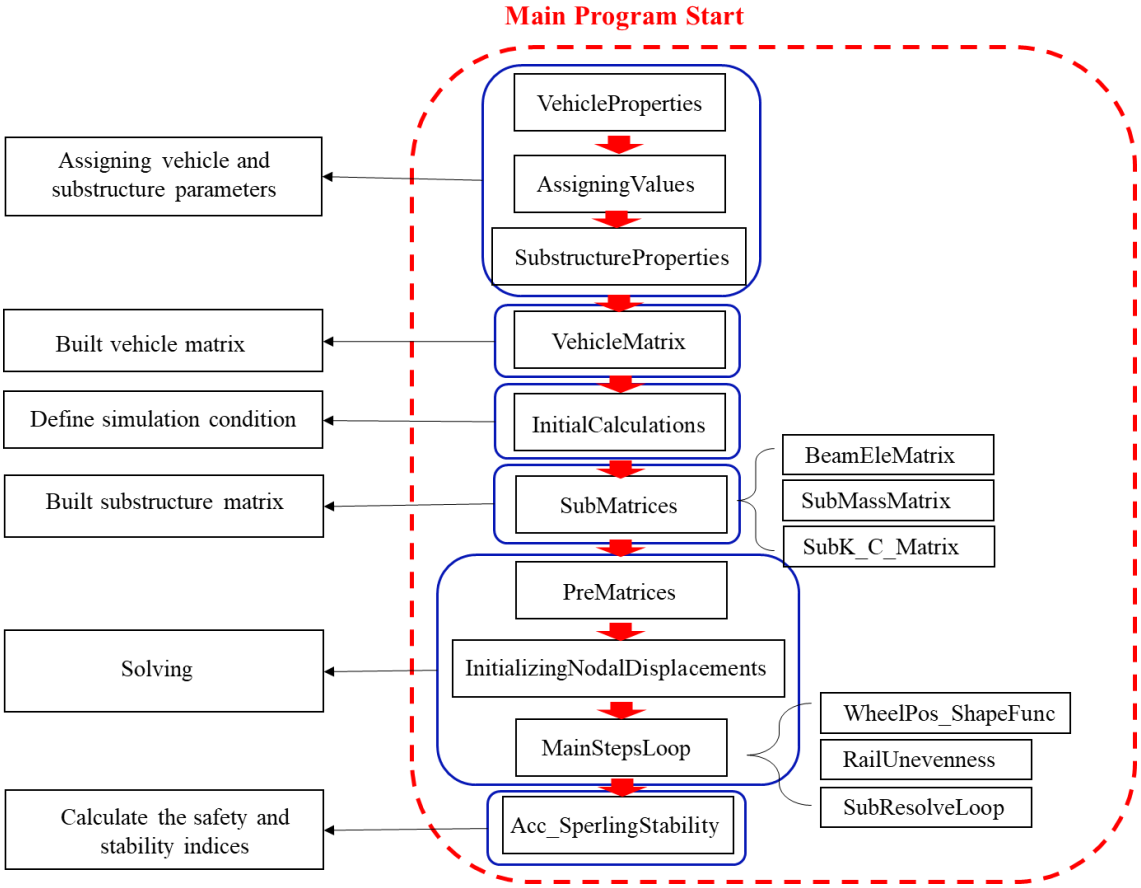

Figure 3-7 Flowcharts of vehicle-track model program

3.4 Model Validation

To investigate the model validation, the simulated result of this vehicle-track model is compared with the simulated results presented in the research paper by Zhai (1997). The model used in this thesis is similar to the one developed in the paper. Namely, in order to compare the former research results with the result of the current model, the parameters used in the validation are the same as those used in the former research. Both the vehicle and track parameters used in the simulation are listed in the Table 3-2. The comparison has been done for the following cases:

1. The peak vehicle wheelset acceleration due to a dipped joint of 0.02 rad.
2. The peak ballast acceleration due to a jagged joint of 1 mm differential height.

Table 3-2 Parameters used in model validation (Zhai et al., 1997)

Vehicle parameters	
Car body mass (kg)	77000
Bogie mass (kg)	1100
Wheel set mass (kg)	1200
Car body inertia (kgm^2)	1.2×10^6
Bogie inertia (kgm^2)	760
Vertical stiffness of primary suspension (N/m)	2.14×10^6
Vertical stiffness of secondary suspension (N/m)	5.32×10^6
Vertical damping of primary suspension (Ns/m)	4.9×10^4
Vertical damping of secondary suspension (Ns/m)	7×10^4
Substructure parameters	
Rubber pad stiffness (N/m)	1.2×10^8
Rubber pad damping (Ns/m)	1.24×10^5
Sleeper mass (kg)	237
Sleeper spacing (m)	0.545
Mass of vibrating ballast (kg)	683
Vertical ballast stiffness (N/m)	2.4×10^8
Vertical ballast damping (Ns/m)	5.88×10^4
Horizontal ballast stiffness (N/m)	7.84×10^7
Horizontal ballast damping (Ns/m)	8.0×10^4
Roadbed stiffness (N/m)	6.5×10^7
Roadbed damping (Ns/m)	3.12×10^4

3.4.1 The peak wheelset acceleration due to dipped Joint

In the case of dipped joints, the authors used the impact velocity as an input excitation to the rail joint similar to the concept presented by Zhai and Sun (1994) (shown in Figure 3-8.). The peak wheelset acceleration due to a dipped joint of 0.02 radian in the track at different vehicle speeds were calculated from the current model. The result is compared with the measured and calculated values given in the paper

(1997). The dipped joint has been modelled using in terms of its impulse velocity.

Seeing Figure 3-9, the values given by the current model fare reasonably well with the Zhai model values and measured values.

The wheel impulsive velocity (v_0) due to the dipped joint can be written as:

$$v_0 = (\alpha_1 + \alpha_2)v \tag{3.65}$$

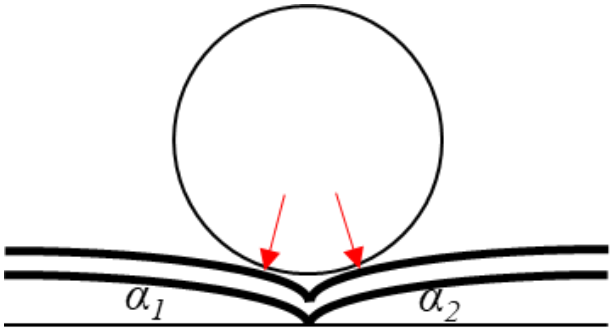

Figure 3-8 The diagram of dipped joint

Where dipped joint angle $\alpha = \alpha_1 + \alpha_2 = 0.02$, α_1, α_2 denotes the angles the dipped joint makes with the horizontal on either side of the dip, v denote the vehicle speed (m/s).

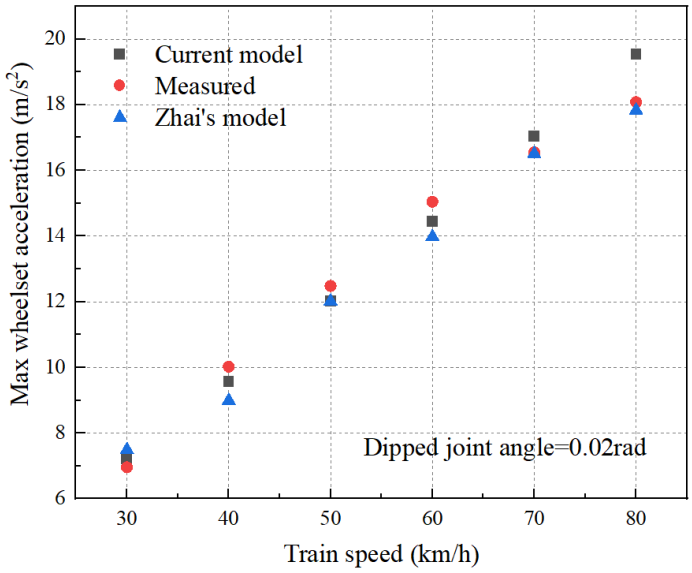

Figure 3-9 Max wheelset acceleration under different train speed

3.4.2 The peak ballast acceleration due to jagged joint

As shown in Figure 3-10, jagged rail joints characterized by the differential height (H) is a source of significant wheel impact.

The peak ballast acceleration at different vehicle speeds due to a jagged joint of 1 mm differential height (H=1mm) in the track were calculated from the model. These were plotted on the measured and calculated values given in the paper (Zhai et al., 1997) and is shown in Figure 3-11. The values from the current model show high consistence with measured values.

The wheel impulsive velocity (v_0) due to the jagged joint can be written as:

$$v_0 = v\left[\frac{2H}{r}\right]^{\frac{1}{2}} \tag{3.66}$$

Where H denotes differential height (m), r (=0.42m) denote the wheel radius, v denote the vehicle speed (m/s).

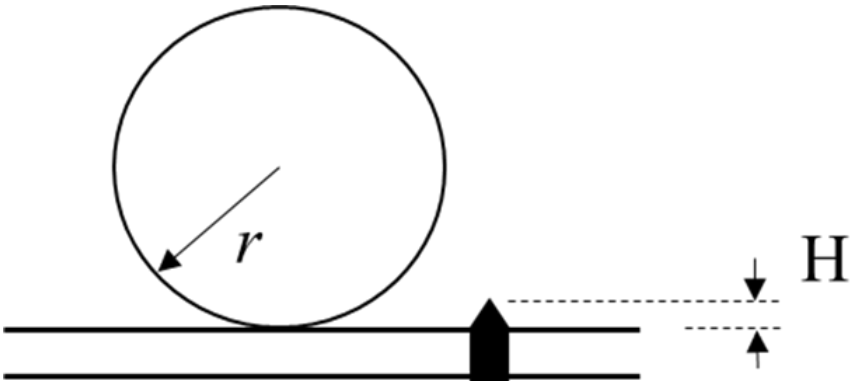

Figure 3-10 The diagram of jagged joint

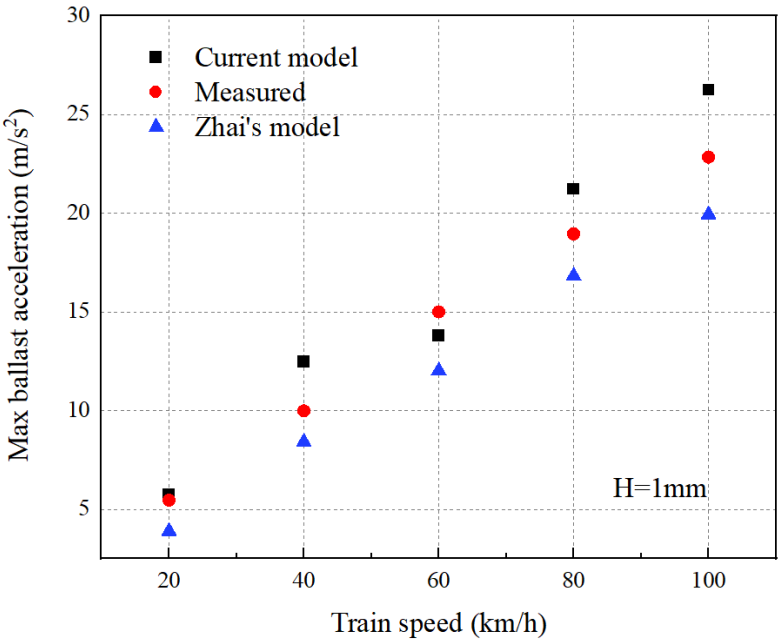

Figure 3-11 Max ballast acceleration under different train speed

3.5 Simulation condition

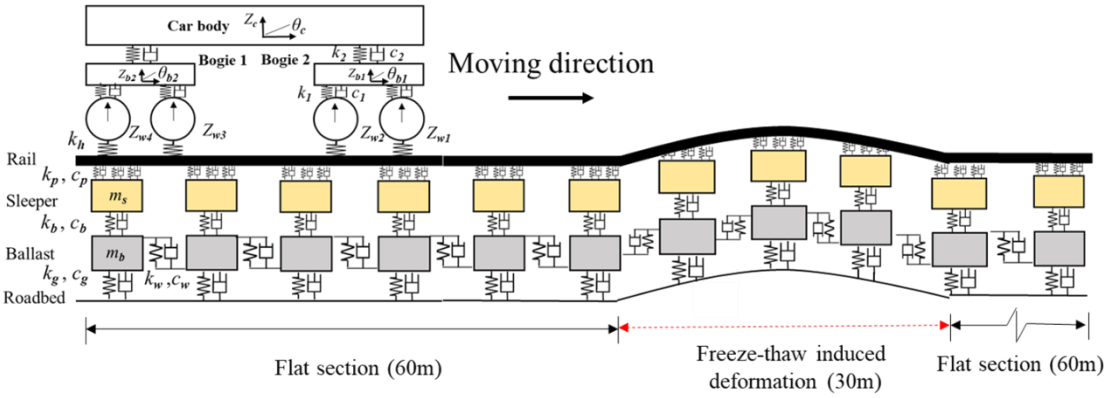

Figure 3-12 Diagram of simulation condition

In order to study the influence of freeze-thaw induced track surface deformation on train vibration, the simulated deformation of the surface is inputted to the vehicle track model. In the simulation, time step (t_{step}) equals 5×10^{-5} (s). To investigate the influence of a wide range of train speeds, the vehicle model runs under different train

speed (V=120, 140, 160, 180, 240, and 300 km/h) on the track model which total length (L_t) is 150m. After passing the 60m smooth track, the train begins to traverse the deformed track caused by freeze-thaw (see Figure 3-12). The dynamic vehicle response is evaluated under different train speeds, different GWLs, and different seasons (i.e. freezing and thawing period). In this study, other geometric and elastic irregularities are not considered except for the freeze-thaw-induced track surface deformation.

4. RESULTS OF FREEZE-THAW ANALYSIS

4.1 Influence of Temperature

To evaluate the influence of freeze-thaw on track surface deformation, point A, located in the middle of the top surface (see Figure 2-1), is selected as an observation point. Its deformation variation is compared with the trend of temperature change, as shown in Figure 4-1. The variation in the vertical displacement of point A coincides with the change in temperature. It is noticeable that in the early period of freezing, the deformation does not show a clear increasing trend before the frost penetration depth reach the subgrade. When the frost penetration depth reaches the subgrade, the vertical displacement increases significantly and reaches a peak of 25mm on the 120th day (as the pink dash line shown in Figure 4-1). After the surface temperature becomes positive, the vertical displacement decreases with the increase in surface temperature. It clearly depicts that the largest vertical displacement occurs during the freezing period. Figure 4-2 shows the temperature contour of the culvert transition section on the 120th day.

It can be seen that the frozen depth at the central area is deeper compared with the side area due to the existence of the culvert. This is because both the culvert and the ground surface boundary condition will influence the area above the culvert (i.e., central area) while the side area is only influenced by the ground surface boundary. For this reason, point B, located on the left side of the top surface (see Figure 2-1), is selected to compare with point A. Both displacement of point A and point B shows the same variation trend. Comparing the freeze-thaw induced displacement of point A and point B, the displacement difference of point A and point B reaches the maximum value on the 120th day in the freezing period. Besides, the displacement difference of these two points reaches a stable value on the 165th day in the thawing period. Therefore, the deformation values on these two days are used in the following analysis.

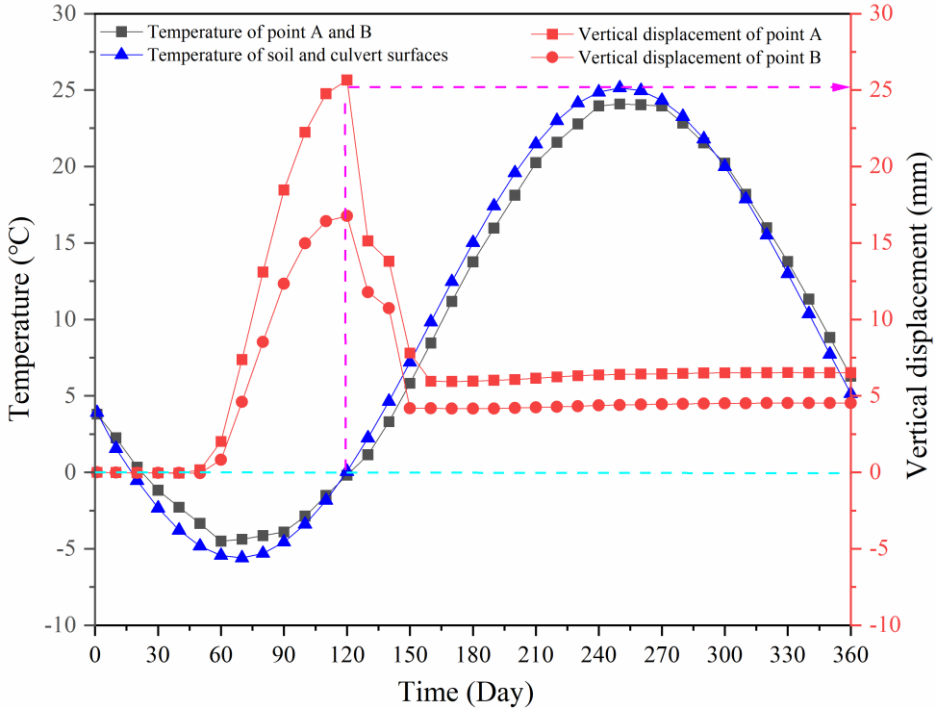

Figure 4-1 Change in vertical displacement of points A and B with surface temperature in one year (GWL=13m, Box culvert)

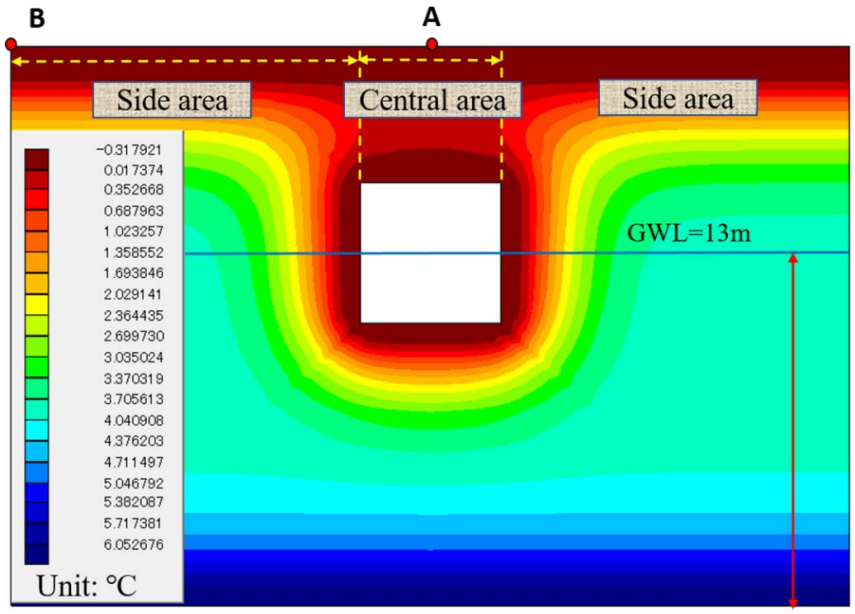

Figure 4-2 Temperature contour of the box culvert transition section (Day 120, GWL=13m)

4.2 Influence of GWL

The simulated track surface deformation of pipe culvert and box culvert transition section under different GWL are separately plotted in the Figure 4-3 and Figure 4-4. The total track surface deformation of the top surface after frost heave and thaw settlement for five different GWLs are shown in Figure 4-5 and Figure 4-7. In addition, the relative track surface deformation induced by freeze-thaw is depicted in Figure 4-6 and Figure 4-8. The total track surface deformation means the vertical displacement of each point on the surface calculated in the freeze-thaw analysis (the displacement calculated in the initial analysis is cleared before freeze-thaw analysis). The relative track surface deformation is calculated by subtracting the total track surface deformation of point B (see Figure 4-2, Point B is the endpoint in the FEM model without boundary effect, i.e., the total track surface deformation of point B is constant if expanding the model width.) from the total track surface deformation of each point on the surface. In the freezing period, Figure 4-5 illustrates that the total track surface deformation has a significant increase with GWL when the GWL is above the bottom of the buried structure in both culvert types. As shown in Figure 4-7, the same phenomenon can be seen in the thawing period. As shown in Figure 4-5, the wavelength for the pipe culvert case is larger than the wavelength for the box culvert case when the GWL is 18m in the freezing period. As a result, in the thawing period, a platform (shown in Figure 4-7(b) and Figure 4-8(b)) appeared in the central part for the pipe culvert case.

The total track surface deformation and relative track surface deformation of point A are shown in Figure 4-9. It can be seen that the both track surface deformations of point A during the freeze-thaw is positively related to the GWL. The vertical displacement of point A does not show an obvious increase with GWL when GWL is below the culvert bottom (i.e., 5m, 7m, and 9m). The vertical displacement of point A shows an obvious increase with GWL when GWL exceeds the culvert middle (i.e., 13m, 18m). Moreover, total track surface deformation and relative track surface deformation of point A in the freezing period are larger than those in the thawing period. It will have a severe impact on the vibration of the train when the subgrade deformation exceeds a particular value. Different countries have proposed corresponding deformation control standards; the settlements are limited to 12.5 mm (20 m chord), 15 mm (20 m chord), and 15 mm (20 m chord) in the Japanese, German, and Chinese specifications,

respectively (Cai et al., 2019). The water content will influence the deformation characteristics of the subgrade in the freeze-thaw period. In this way, controlling groundwater levels provides a feasible way to control the deformation of the subgrade.

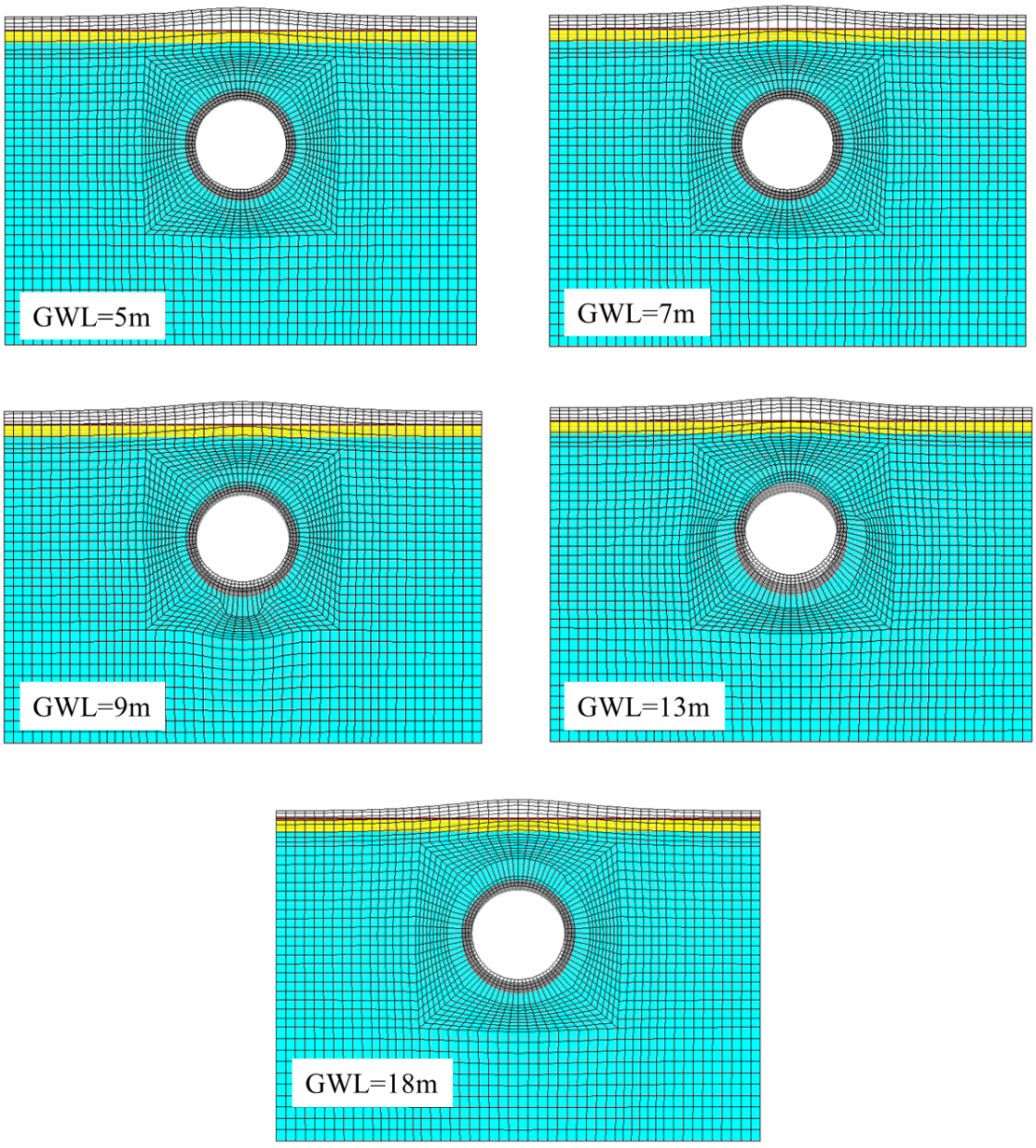

Figure 4-3 The surface deformation of pipe culvert transition section under different GWL (Day 120)

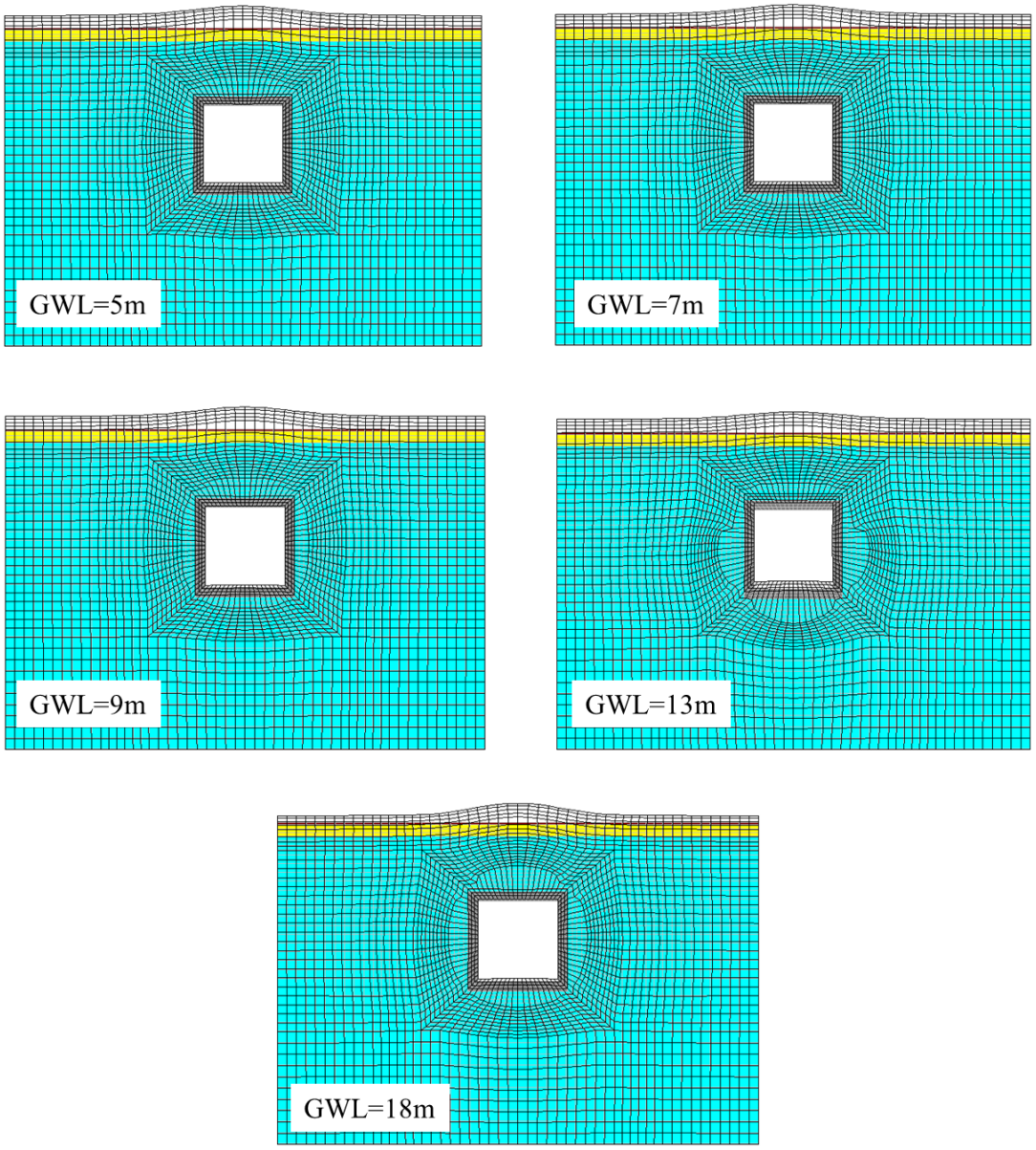

Figure 4-4 The track surface deformation of box culvert transition section under different GWL (Day 120)

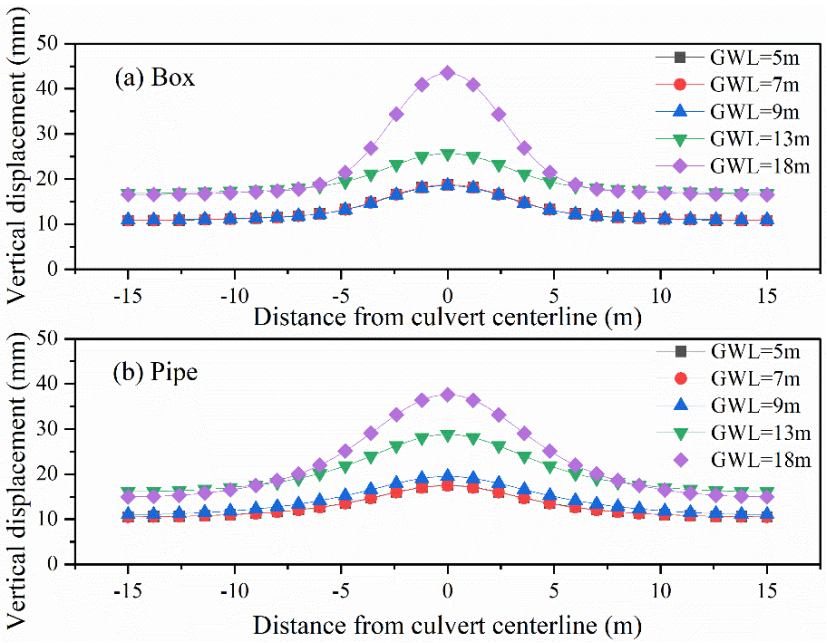

Figure 4-5 Total track surface deformation of surface in the freezing period (Day 120): (a) Box culvert (b) Pipe culvert

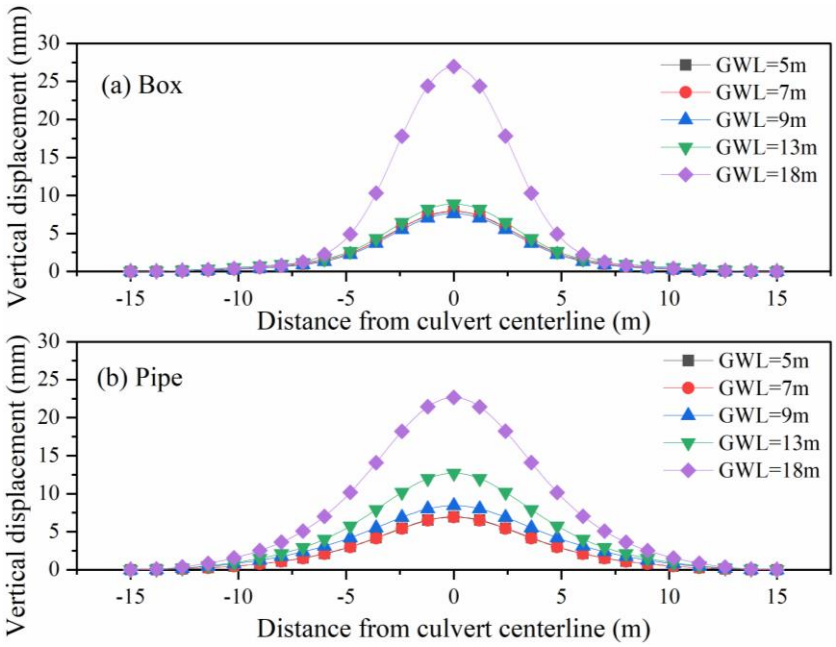

Figure 4-6 Relative track surface deformation of surface in the freezing period (Day 120): (a) Box culvert (b) Pipe culvert

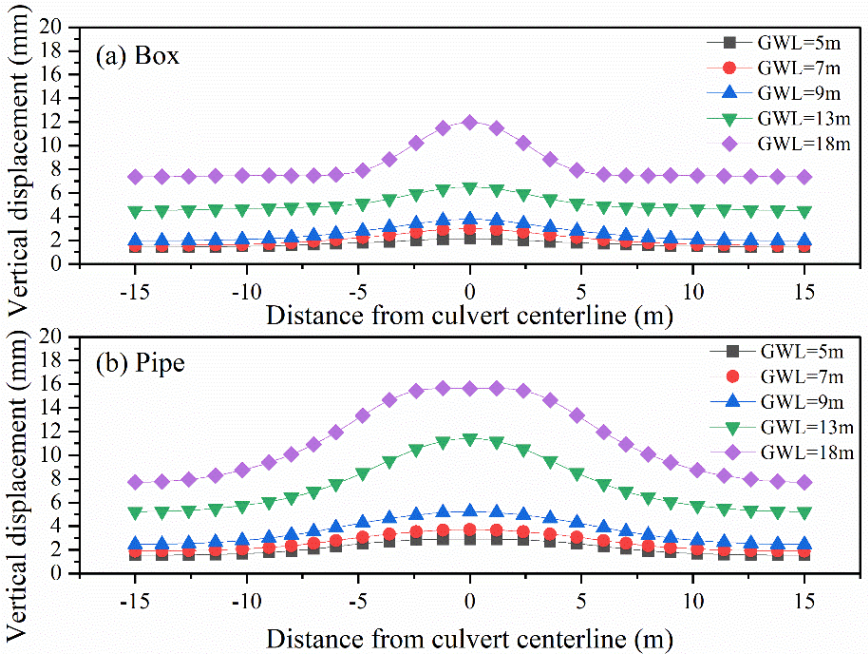

Figure 4-7 Total track surface deformation of surface in the thawing period (Day 165): (a) Box culvert (b) Pipe culvert

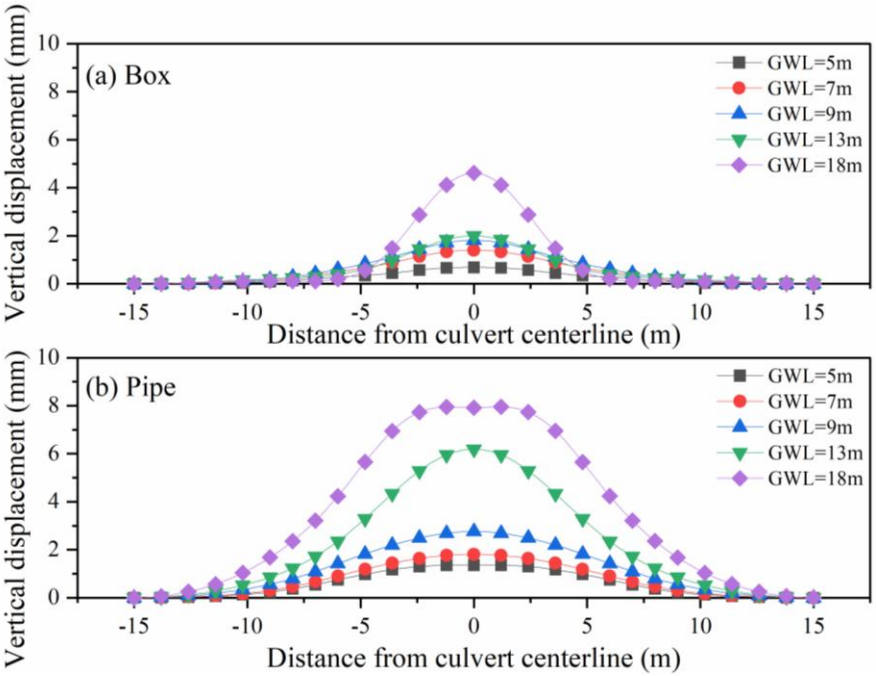

Figure 4-8 Relative track surface deformation of surface in the thawing period (Day 165): (a) Box culvert (b) Pipe culvert

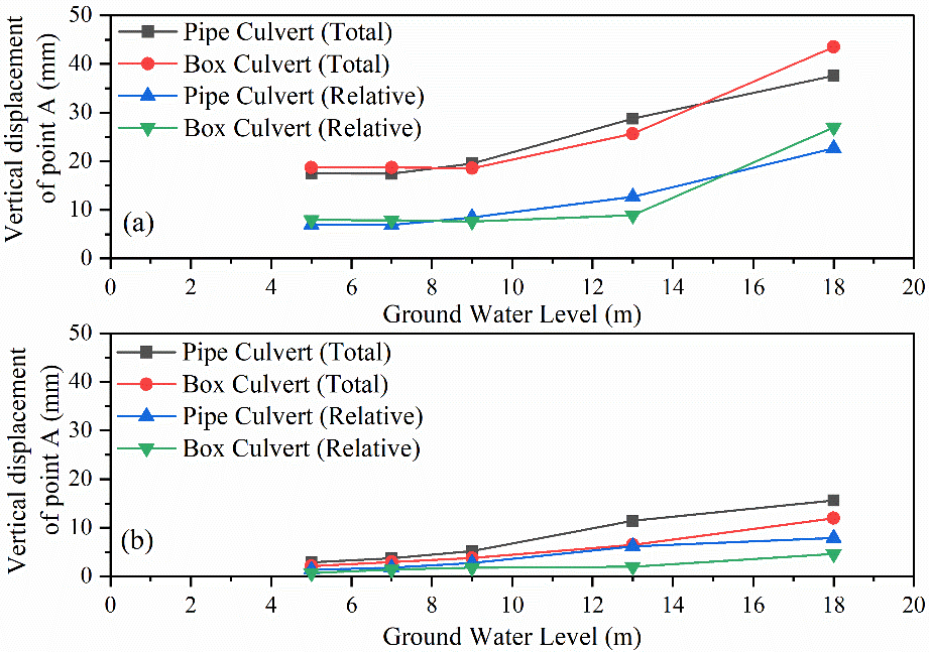

Figure 4-9 Total track surface deformation and relative track surface deformation of point A: (a) Freezing period (Day 120) (b) Thawing period (Day 165)

4.3 Evaluation of Amplitude and Wavelength

To quantitatively evaluate freeze-thaw-induced track surface deformation, the track surface deformation is estimated from the aspect of wavelength and amplitude. As per the study of former researchers, the subgrade deformation induced by the frost heave in the longitudinal direction can be estimated as a cosine curve function (Cai et al., 2019; Guo et al., 2018). Similarly, this study uses a sine curve function to estimate frost heave induced relative track surface deformation (y) as follows:

$$y = \begin{cases} y_0 + A_0 \sin\left(\pi\left(x - x_0\right)/l\right) & \left(x \in \textit{Deformation area}\right) \\ 0 & \left(x \in \textit{No deformation area}\right) \end{cases} \tag{4.1}$$

Where A_0 is the amplitude of frost heave, l is the wavelength of frost heave, and x is the longitudinal position of subgrade surface, x_0 and y_0 are fitting parameters. In this study, the side area is assumed as no deformation, and the deformation at the central

area is estimated as a sine curve. The whole relative track surface deformation is estimated by using the piecewise fitting method. The range of x is determined by the split point, where the coefficient of determination (R^2) has the best solution.

The freeze-thaw induced relative track surface deformation was fitted by Eq. (4.1). As shown in Figure 4-10, the deformation curve in the freezing period has a high coincidence with Eq. (4.1). In the thawing period, the estimated result by Eq. (4.1) also shows a high degree of agreement with the relative track surface deformation, though the result is not shown in this study. To show the variation trend of amplitude and wavelength, the polynomial formulas are used to fitting the variation trends. The variation of amplitude and wavelength is shown in Figure 4-11 and Figure 4-12. In the freezing period, for the pipe culvert case, both the amplitude and wavelength increase with the increase in GWL, while for the box culvert case, the wavelength decreases in the total trend but increases when the GWL is close to the middle of the culvert (GWL=13m). In the thawing period, for the pipe culvert case, both the amplitude and wavelength increase with the increase in GWL, while for the box culvert case, the amplitude increases with the increase in GWL, though the wavelength decreases with GWL. It is preliminarily inferred that these phenomena are caused by the different boundary conditions produced by different culvert shapes.

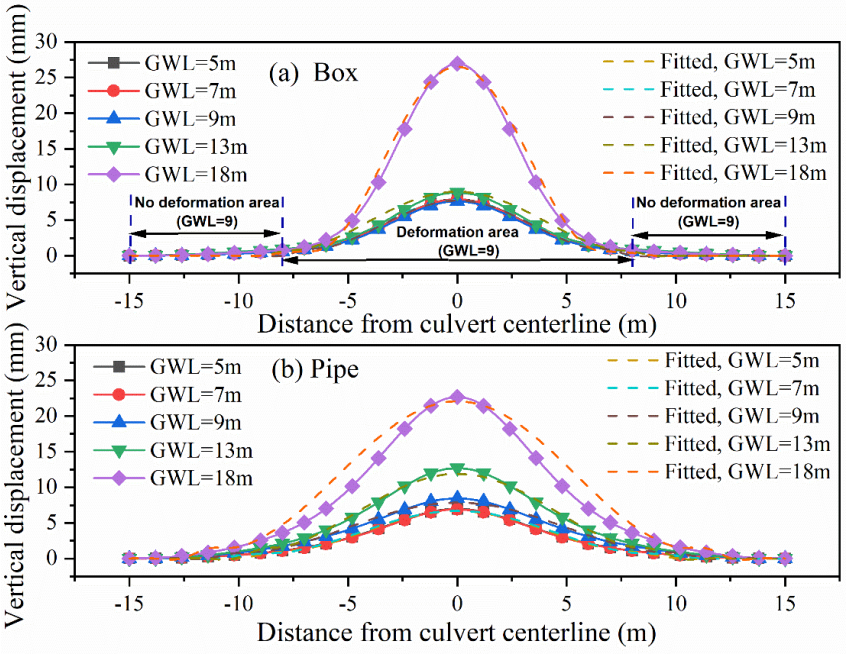

Figure 4-10 Fitted results of relative track surface deformation by Eq.10 in the

freezing period (Day 120): (a) Box culvert (b) Pipe culvert

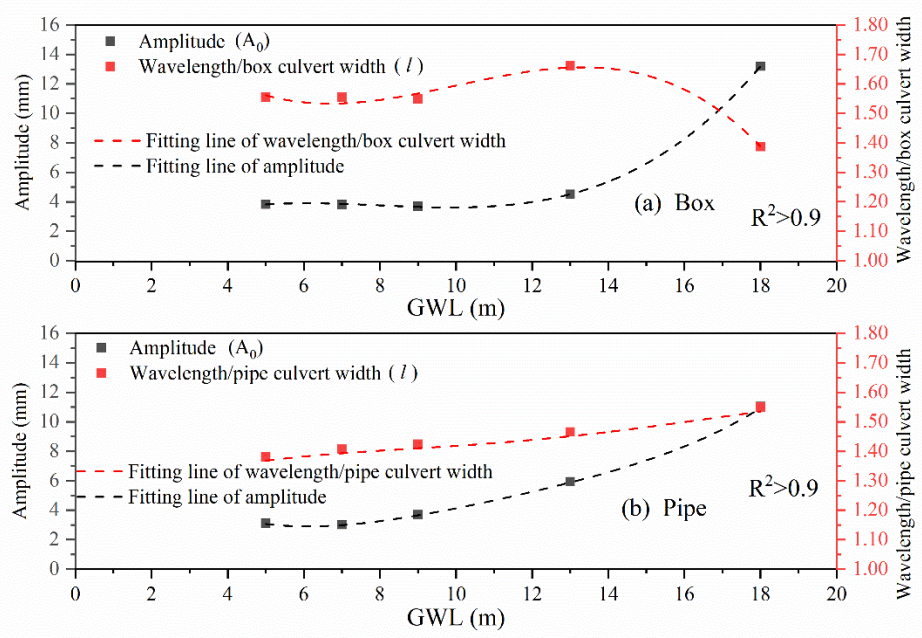

Figure 4-11 Amplitude and wavelength in the freezing period (Day 120): (a) Box culvert (b) Pipe culvert

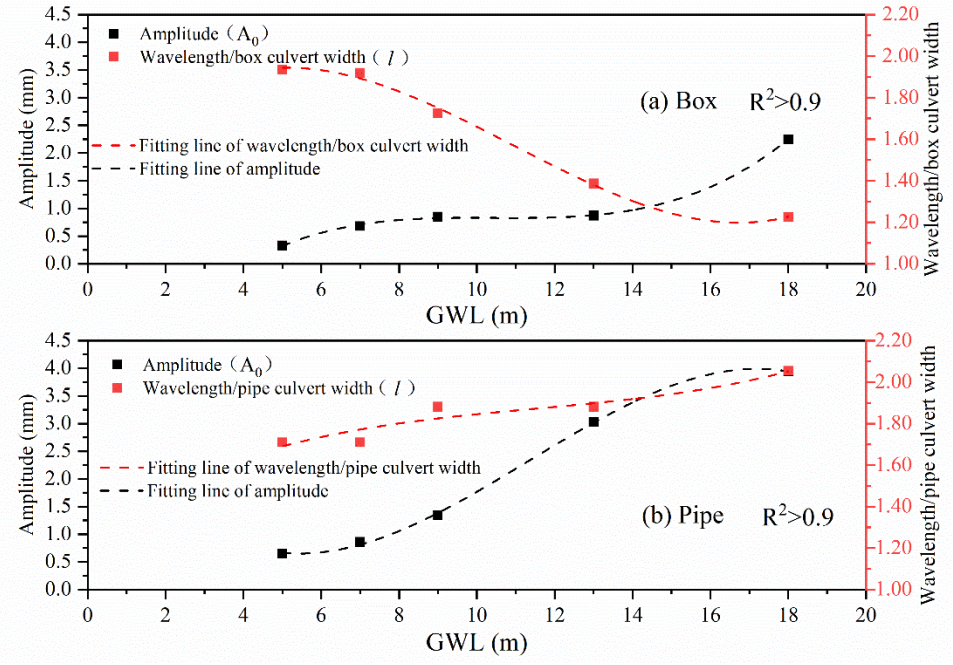

Figure 4-12 Amplitude and wavelength in the thawing period (Day 165): (a) Box culvert (b) Pipe culvert

4.4 Summary of This Chapter

In this chapter, the influence factors of temperature, GWL and buried structure type were investigated in the freeze-thaw analysis. The freeze-thaw induced track surface deformations were evaluated from the aspect of amplitude and wavelength. The following findings can be mainly observed:

(1) The maximum track surface deformation occurred in the freezing period in both cases of culvert. The amplitude located in the middle of the top surface (i.e. point A).

(2) The amplitude has no significant increase when the GWLs are below the bottom of the culvert. When the GWLs is higher than the bottom of culvert, the amplitude increase with GWLs in both cases of culvert.

(3) Comparing with the pipe culvert case, the box culvert case has a larger amplitude in both freezing and thawing period.

(4) In the freezing period, for the pipe culvert case, both the amplitude and wavelength increase with the increase in GWL, while for the box culvert case, the wavelength decreases in the total trend. In the thawing period, for the pipe culvert case, both the amplitude and wavelength increase with the increase in GWL. For the box culvert case, the amplitude increases with the increase in GWL, though the wavelength decreases with GWL.

5. RESULTS OF TRAIN VIBRATION ANALYSIS

The train vibration analysis is conducted from the aspect of safety evaluation and stability evaluation. For the vehicle running safety, three principal indices, minimum vertical wheel-rail force, maximum vertical wheel-rail force, and wheel load reduction rate are used for evaluation. For the vehicle running stability, the car body acceleration and the Sperling index are adopted to evaluate passenger ride comfort. Each of these two evaluations has two aspects, namely vertical and lateral evaluation. However, only the vertical stability evaluation is conducted for simplicity in this study.

5.1 Safety Evaluation

5.1.1 Minimum vertical wheel-rail force

The wheels move up and down during the vibration process when the vehicle is running at a high speed. Consequently, the wheel-rail force will either increase or decrease. In this case, the decrease of wheel-rail force will increase the wheel lift height, which means the derailment may easily occur (Wei et al., 2018; Zeng et al., 2008; Ishida et al., 1999). As one of safety index, this study investigated the minimum vertical wheel-rail force. Figure 5-1 shows the simulated wheel-rail force under different conditions (GWL, freeze-thaw), which was derived from the vehicle dynamic analysis where track displacement was inputted into the vehicle-track model. The decrement of vertical wheel-rail force equals the difference between static wheel load and minimum vertical wheel-rail force. The decrement of vertical wheel-rail force shows an increasing trend with the GWL increase. In the freezing period, at the train speed of V=300 km/h, the minimum wheel-rail force decreases to 0 kN (decrement equal to static wheel load of 78.15kN) and 34.82 kN (55.4% decrease compared with static wheel load) corresponding to the box culvert case and the pipe culvert case when the GWL is 18 m. In addition, in the freezing period, the decrement of minimum wheel-rail force for the box culvert case is less than the value for the pipe culvert case. A similar trend can also be found in the thawing period.

Figure 5-2 shows the results of decreased wheel-rail force under different conditions (train speed, freeze-thaw), which was derived from the vehicle dynamic analysis where track displacement was inputted into the vehicle-track model. As

depicted in Figure 5-2, in total, the decrement of minimum wheel-rail force increases with train speed in both cases of culvert.

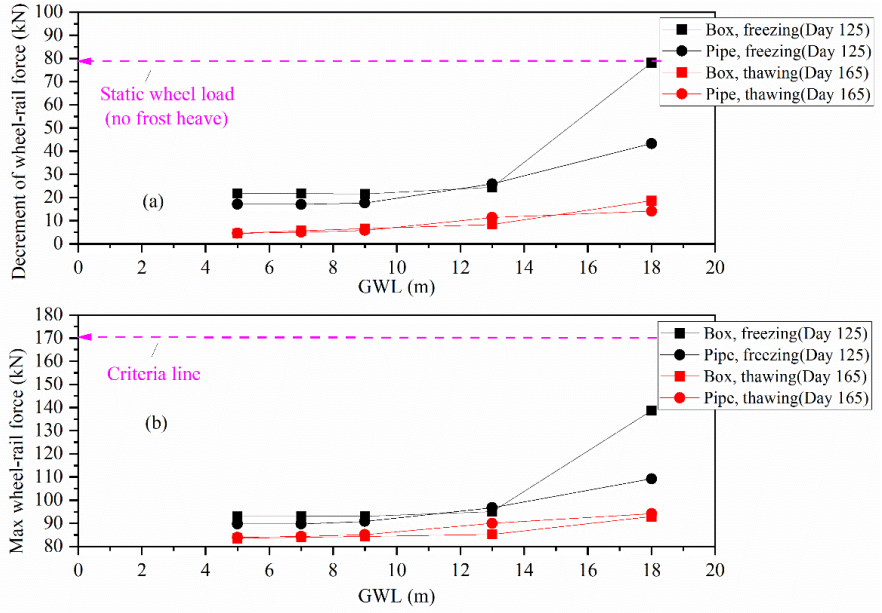

Figure 5-1 Safety under different GWL (V=300km/h): (a) Decrement of wheel-rail force (b) Max wheel-rail force

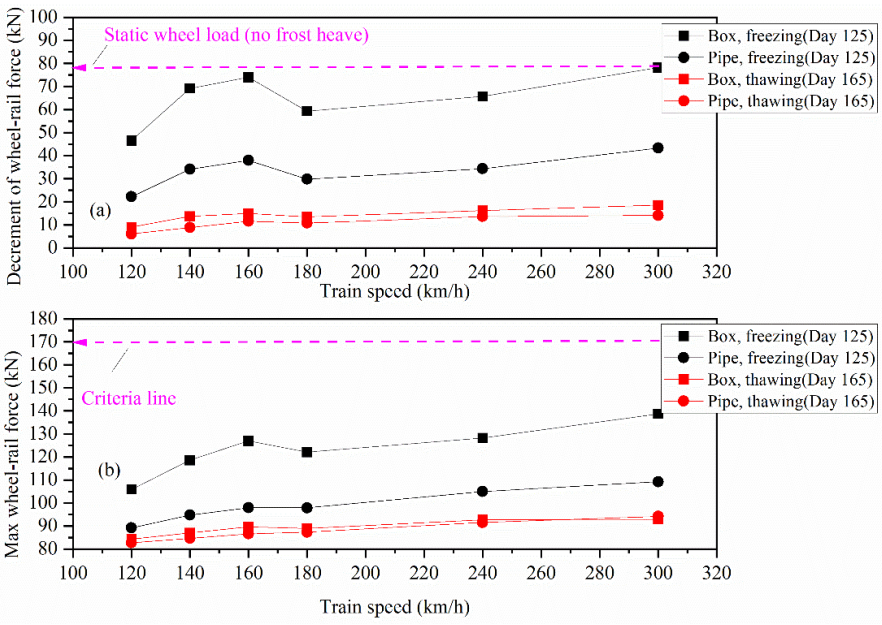

Figure 5-2 Safety under different train speed (GWL=18m): (a) Decrement of wheel-rail force (b) Max wheel-rail force

5.1.2 Maximum vertical wheel-rail force

The maximum vertical wheel-rail force is an essential indicator for evaluating the safety of train operation used in many countries. The maximum vertical wheel-rail force should not exceed the design loads for substructure components (Cai et al., 2019; Zhai 2015). As stipulated by the German federal railways, the maximum vertical wheel-rail force is not allowed to exceed the limit value of 170kN. According to the high-speed railway test specifications of China, the maximum wheel-rail vertical force is also 170kN (Zhai 2015).

Figure 5-1 also shows the maximum vertical wheel-rail forces obtained from the numerical simulations under different GWLs in both freezing and thawing periods. The maximum vertical wheel-rail forces in both periods increase with the GWL increase for both cases of culvert. Besides, Figure 5-2 shows the maximum vertical wheel-rail forces under different train speeds. The maximum vertical wheel-rail forces have a positive correlation with train speed. In other words, as the train speed increases, the maximum vertical wheel-rail force may exceed the control standard. The maximum wheel-rail force in the thawing period is lower than the criteria, while the maximum wheel-rail force in the freezing period is close to the criteria. In addition, the maximum wheel-rail force for the box culvert case is higher than that for the pipe culvert case. The reason is that different boundary conditions are produced by different culvert shapes, resulting in the amplitude increases with the increase in GWL for the box culvert case. In summary, the train speed and the amount of relative displacement seriously affect safety. In case not considering the deceleration, reducing the displacement caused by freeze-thaw is an effective way to improve the safety of train operation.

The objective of this research is to study the interaction between the influences factors of freeze-thaw of track and train vibration. As shown in Figure 5-2, the decrement of wheel-rail force and the maximum wheel rail force shows increase with train speed in the main variation trend. For the phenomenon of the peak value at the train speed 160km/h, it may be caused by the critical train speed, and further research is needed for the reason of this phenomenon.

5.1.3 Wheel load reduction rate

The wheels move up and down during the vibration process when the vehicle runs at a high speed. Consequently, the wheel load will either increase or decrease. In this case, the wheel load reduction rate is an important indicator for evaluating train operation safety and is commonly used to evaluate derailment in many countries. Here, the wheel load reduction rate is defined as $\Delta P/P_0$, ΔP is wheel load reduction defined as the difference between wheel-rail force in the frost heave section and the static wheel load, P_0 is the average static wheel load of wheel set (Cai et al., 2019; Zhai 2015; Sayeed et al., 2018).

Table 5-1 Criteria of wheel load reduction rate (Zhai 2015; Ishida et al., 1999)

Country	Standard
EURCODE	$\Delta P/P_0 \leqslant 0.6$
Japan	$\Delta P/P_0 \leqslant 0.6$
China	$\Delta P/P_0 \leqslant 0.6$

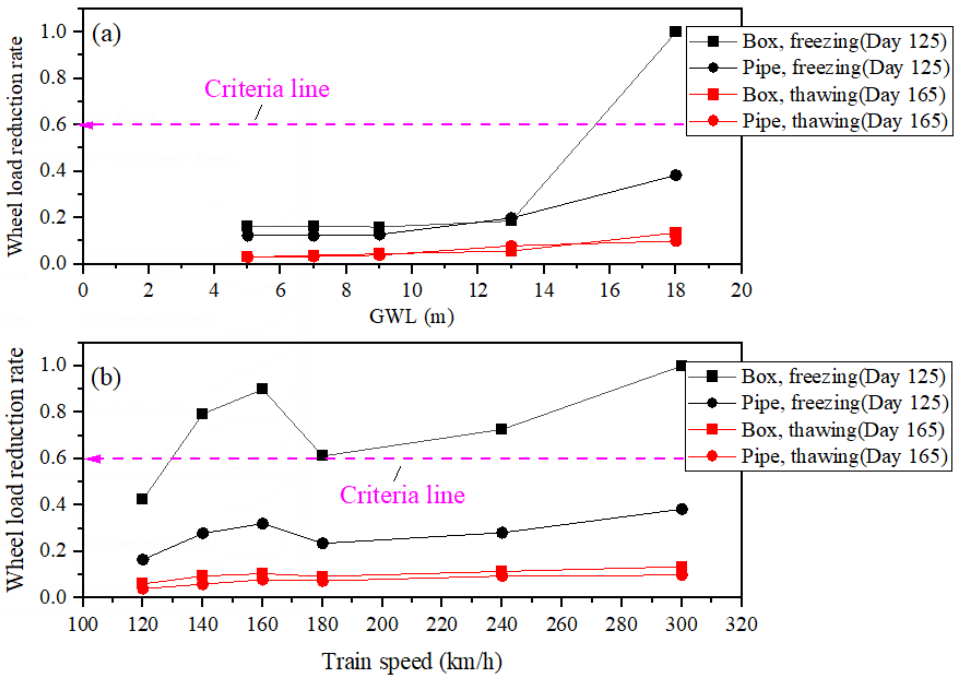

Figure 5-3 Wheel load reduction rate: (a) under different GWLs (V=300km/h) (b) under different train speeds (GWL=18m)

Figure 5-3 shows the wheel load reduction rates obtained from the numerical simulations under different GWLs and train speeds in both freezing and thawing periods. The wheel load reduction rates increase with the GWL increase for both cases of culvert. In Figure 5-3(a), when GWL is 18m, the wheel load reduction rate exceeds the criteria for the box culvert case in the freezing period. The wheel load reduction rate has a positive correlation with train speed. In Figure 5-3(b), for the box culvert case, the wheel load reduction rate exceeds the criteria at higher train speed than 140km/h in the freezing period. Besides, since the train vibration is sensitive to the train speed of 140 and 160 km/h, the wheel load reduction rate has a higher value when train speed is 140 and 160 km/h than when train speed is 120 and 180 km/h. In addition, the wheel load reduction rate for the case of the box culvert is higher than the case of the pipe culvert. To ensure the safety of train operation, the selection of the buried structure type and the reduction of GWL are effective countermeasures.

5.2 Stability Evaluation

5.2.1 Car body acceleration

As a stability evaluation index, different countries have developed different control standards of maximum car body acceleration. The criteria for maximum car body acceleration of China, Europe, and Japan are listed in Table 5-2 (Jeon et al., 2016; Zhai 2015; Zhou 2012). Figure 5-4 shows the maximum car body acceleration (a_{vmax}) obtained from the numerical simulations under different GWLs and different train speeds in both freezing and thawing periods. The calculated car body acceleration reaches to max value when the GWL is 18m in the freezing period, though it is much smaller than the controlling criteria value shown in Table 5-2. The maximum car body acceleration for both cases of culvert increases with the increase in GWL at a constant train speed (V=300km/h). This phenomenon indicates that controlling groundwater levels provides a feasible way to decrease the maximum car body acceleration. In addition, the maximum car body acceleration increases with the increase of train speed at a constant GWL (18m), which means that the maximum car body acceleration could be beyond control standards at a higher train speed. These indicate that in case not considering the reduction of train speed, it is a feasible solution for the stability of train operation to control the freeze-thaw induced track surface deformation by reducing the

groundwater level. Besides, by comparing the result of the box culvert case and pipe culvert case, the type of buried structure also affects the maximum car body acceleration. It implies that one of the countermeasures to reduce the maximum car body acceleration is considering the buried structure type.

Table 5-2 Acceleration controlling criteria

Country	Standard
China	a_v≤2.5m/s^2 (Coach), a_v≤7.0m/s^2 (Wagon)
Europe	a_v≤1.0m/s^2 (Excellent), a_v≤1.3m/s^2 (Good), a_v≤2.0m/s^2 (Qualified);
Japan	Descent:2.4m/s^2 /Ascent:2.0m/s^2 (Inspection vehicle, high-performance premium train) Descent:3.6m/s^2 /Ascent:3.0m/s^2 (Other coach)

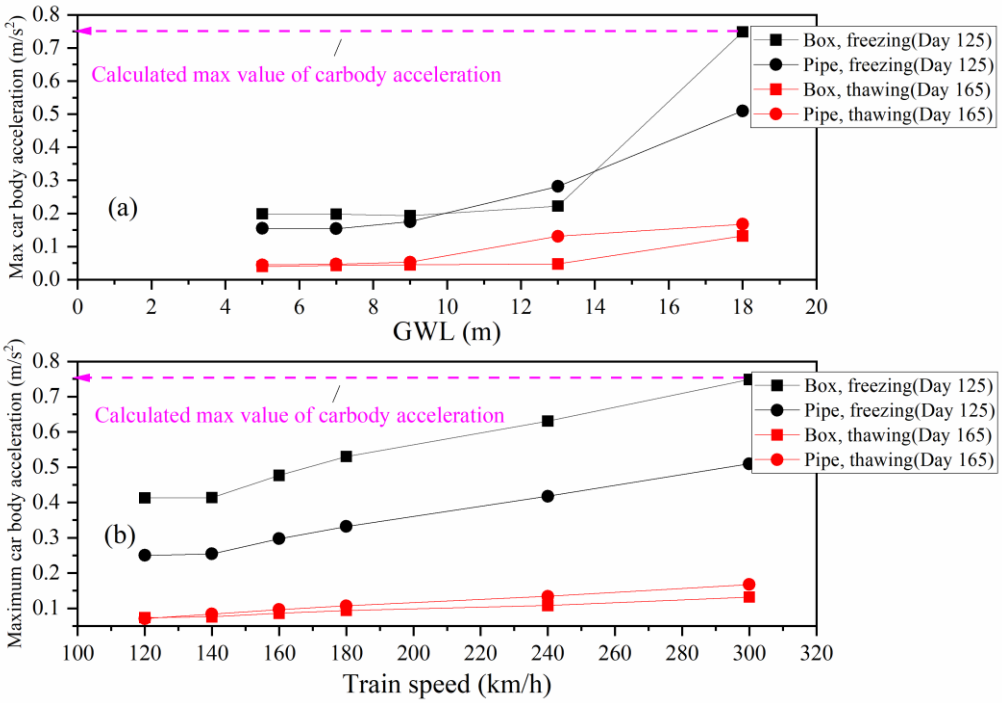

Figure 5-4 Max car body acceleration: (a) under different GWLs (V=300km/h) (b) under different train speeds (GWL=18m)

5.2.2 Sperling Index

As a stability index, the world widely adopted Sperling index is used to evaluate comfortability (Xia 2017). The rating of the Sperling index can be found in Table 5-3. The Sperling index is written as:

$$W = 3.567\left[F(f)a_v^3 / f\right]^{0.1} \tag{5.1}$$

Where a_v is acceleration of car body (m/s^2), f is frequency (Hz), F (f) is frequency correction factor. For vertical vibration, F (f) is written as:

$$F(f) = \begin{cases} 0.325f^2 & (f = 0.5 \sim 5.9Hz) \\ 400/f^2 & (f = 5.9 \sim 20Hz) \\ 0 & (f > 20\ Hz) \end{cases} \tag{5.2}$$

As the frequency and acceleration change with time, the wave is divided into several groups in accordance with frequency. The comfortability of each group (W_i) is calculated separately in accordance with the corresponding frequency and acceleration. For the comfortability of the total wave, it can be written as:

$$W = \sqrt[10]{W_1^{10} + W_2^{10} + \ldots + W_N^{10}} \tag{5.3}$$

Where N is the entire number of groups for waveband. The acceleration data calculated by train vibration analysis is in the time domain and consists of many dispersed points. In this study, N equals the number of points of acceleration data (i.e. $N = L_t$ /V/ t_{step}). Firstly, the MATLAB built-in FFT function transforms the acceleration from time to the frequency domain. After the FFT, the point number also equals N. Then, the acceleration in the frequency domain was grouped into three sections according to frequency. Each section has many points. Assuming the corresponding number of points in each section is N1, N2, N3 (i.e., N1+N2+N3=N), three sections correspond to three F (f). Note that the N1, N2, and N3 will differ for each train vibration analysis. In each section, each point has corresponding f and a_v. Finally, the W_1, W_2 ...W_N can be calculated with its corresponding F (f), f, and a_v using Eq. (5.1).

Table 5-3 Rating of Sperling index (Xia 2013)

Vibration level	Ride quality	Sperling index (*W*)
Just noticeable	Very good	<1.0
Clearly noticeable	Good	1.0~2.0
Pronounced but not unpleasant		2.0~2.5
Strong but tolerate	Tolerable	2.5~3.0
Very strong and unpleasant		3.0~3.5
Extremely strong and unpleasant	Not tolerable	3.5~4.0

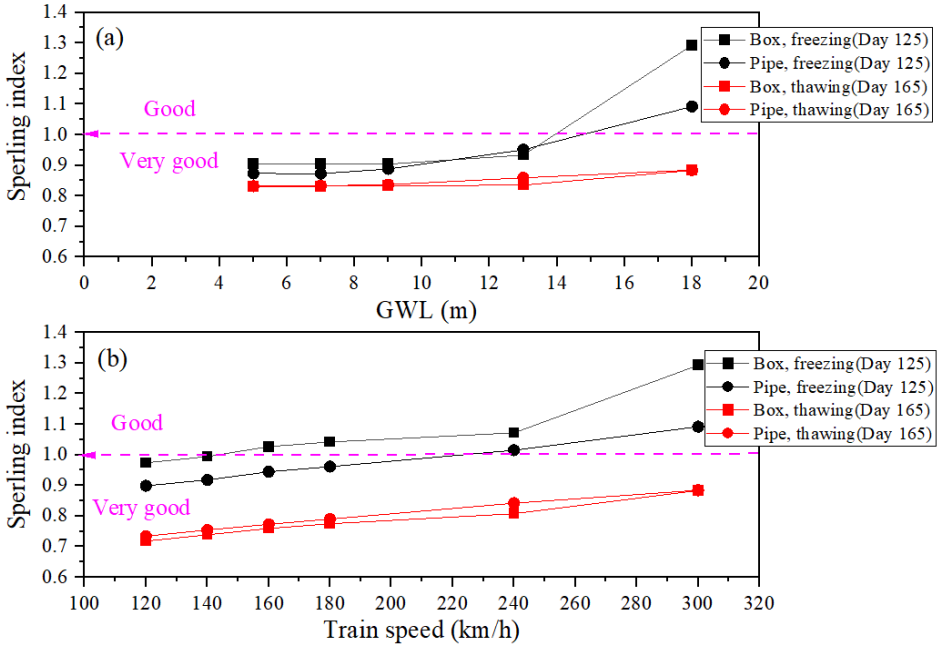

Figure 5-5 Sperling index: (a) under different GWLs (V=300km/h) (b) under different train speeds (GWL=18m)

The results of Sperling index under different GWLs and different train speeds in both freezing and thawing periods are shown in Figure 5-5. The pink dotted line means the dividing line of ride quality shown in Table 5-3. Besides, the Sperling index has a larger value in the freezing period, which means that the vehicle stability in the freezing period is lower than the thawing period. Figure 5-5 shows that compared with the pipe culvert case, the box culvert case has a larger Sperling index value in the freezing period. In addition, the Sperling index positively correlates with train speed and GWL, which

means that the instability of the vehicle increases with train speed and GWL, irrespective of the culvert case. In Figure 5-5(a), when GWL is over 15m, the ride quality change from 'Very good' to 'Good' for both culvert types in the freezing period. In Figure 5-5(b), for both culvert types, the ride quality changes from 'Very good' to 'Good' at higher train speed than 240km/h in the freezing period. Although acceleration does not exceed control standards, riding comfort level drops at higher train speeds and higher GWL. To ensure riding comfort, choosing the buried structure type and reducing GWL are effective countermeasures.

5.3 Summary of This Chapter

In this chapter, the safety (minimum vertical wheel-rail force, maximum vertical wheel-rail force, and wheel load reduction rate) and stability were investigated considering different factors (i.e. GWLs, temperature, and buried structures) under different train speeds. The following findings can be mainly observed:

(1) Both in the freezing and thawing period, the decrement of minimum wheel-rail force for the box culvert case is less than the value for the pipe culvert case. The decrement of vertical wheel-rail force shows an increasing trend with the GWL and train speed increase.

(2) For both case of culvert, the maximum vertical wheel-rail forces increase with train speed and GWL. Besides, for the box culvert case, it has larger maximum vertical wheel-rail forces comparing with the pipe culvert case.

(3) The wheel load reduction rates increase with the GWL and train speed for both cases of culvert. Besides, for the box culvert case, it has larger wheel load reduction rates comparing with the pipe culvert case.

(4) Both maximum car body acceleration and Sperling index increase with train speed and GWL in the freezing and thawing period. For the Sperling index, when GWL is over 15m, the ride quality change from 'Very good' to 'Good' for both culvert types in the freezing period. In addition, for both culvert types, the ride quality changes from 'Very good' to 'Good' at higher train speed than 240km/h in the freezing period.

6. DIFFERENTIAL PLASTIC DEFORMATION OF BALLASTED TRACK UNDER CYCLIC LOADS

The accumulated deformation of track structure will increase due to long-time running, which would cause various kinds of track irregularities. These irregularities will greatly excite the detrimental vibration between vehicle and track, not only deteriorating the train running quality but also posing extremely unfavorable effects on the parts damage of the wheel-rail system and the track quality.

The track surface deformation induced by frost heave of subgrade will affect the vibration between vehicle and track, therefore, affecting the process of ballast settlement. Lin et al. (2018) investigated the characteristics and controlling factors of frost heave in high-speed railway. On the other side, scholars established various models to predict ballast deformation (Sato, 1995; Ford et al., 1995; Shenton, 1985; Thom, 2006). Thom and Ford et al. studied the permanent deformation of ballast and proposed their model to predict the differential ballast settlement.

According to the research of Zhai (2004), about 75% of the daily maintenance work on track structures is due to the ballast and its deformation. Thus, it is very important to investigate the settlement of the ballast so as to minimize its vibration level. In this chapter, the differential settlement affected by the frost heave induced track surface deformation was investigated. Same as mentioned in the chapter 3, the frost heave induced track surface deformation was calculated with a thermal-hydro-mechanical (THM) finite element model. The calculated relative track surface deformation was inputted into the vehicle-track model as an excitation. The force below each sleeper were outputted for the calculation of the ballast layer. The research flowchart is shown in Figure 6-1.

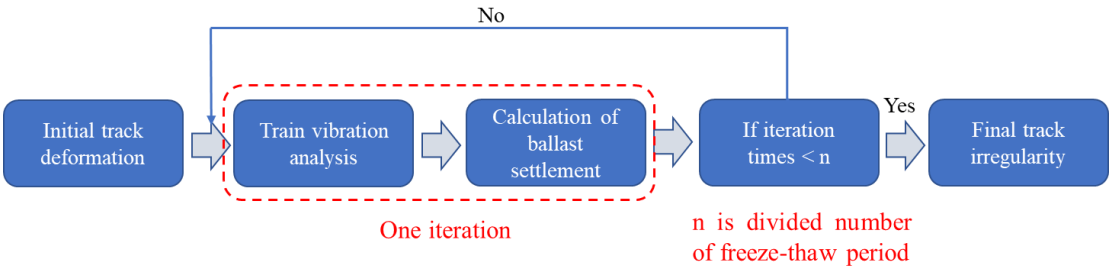

Figure 6-1 Settlement calculation process

The simulation investigates the influence of train speed (V=120, 150, 180, 210, 240, 270, and 300 km/h) and GWLs on ballast settlement. A total of 150 m track is simulated. After passing the 60m smooth track, the train began to traverse the deformed track caused by frost heave (See Figure 6-2). Considering the box culvert case, as it has a similar track surface deformation under the GWLs of 5m, 7m, and 9m, the final GWLs are separately assigned as 7m, 13m, and 18m. The ballast settlement after each period in the longitude direction are respectively plotted in Figure 6-4 (a), (b), and (c).

A typical ballasted track of Japan is used in the simulation. The schematic diagram of ballasted track structure is shown in Figure 3-6. A common sleeper spacing of 600mm is adopted in the simulation (Luo et al., 2018; Yang et al., 2021; Aikawa et al., 2013). Only the subgrade is considered as a frost susceptible material and the frost heave induced track surface deformation is contributed from subgrade. In this study, the settlement of roadbed and subgrade will not be considered. In addition, as the residual deformation of track after thaw contraction is quite small, the track may go back to the initial state (Luo et al., 2018). Therefore, the most important period is the freeze-thaw period, when the freeze-thaw induces track surface deformation. The freeze-thaw period is shown in Figure 6-3, marked as gray area. The freeze-thaw period starts when the displacement begins to increase and ends until the displacement reaches a stable value.

6.1 Differential Track Settlement Calculation

In this study, only the clean ballast was considered, and the fouled ballast was not considered. The widely used UIUC model is applied to calculate the settlement of ballast (S) below each sleeper. The model is shown in Eq. (6.1) ~ (6.5) (Yang et al., 2021). In this study, only the ballast settlement during the period where from day 50 to day 150 is calculated. To reflect the variation procedure of track irregularity, the freeze-thaw period needs to be divided into several segments. For simplification, the freeze-thaw period is divided into three periods, and each period is one iteration. The calculation process is shown in Figure 6-1. For the first iteration, the initial track surface deformation at the beginning of frost heave is used to calculate the ballast settlement. The ballast settlement calculated in the first iteration is summed with the frost heave induced track surface deformation of next segment and used for the next iteration. For

each iteration, train vibration analysis is conducted to get the new stress below sleeper by considering the renewed final track deformation. Final track deformation is the sum of ballast settlement (minus) in former iteration and frost heave induced track surface deformation (plus) in the next period. In the freeze-thaw period, the number of load cycles is considered as 300000 (N=300000) in 3 periods (iterations), number of load cycles is 100000 for each period (iteration) (Zhu, 2009).

$$\varepsilon_{\mathrm{p}} = AN^{B}\sigma_{d}^{C}\left(\frac{\tau_{f}}{\tau_{\max}}\right)^{D} \tag{6.1}$$

$$\tau_{f} = \sqrt{\left(\frac{\sigma_{d}}{2}\right)^{2} - \left(\sigma_{f} - \left(\sigma_{3}^{'} + \frac{\sigma_{d}}{2}\right)\right)^{2}} \tag{6.2}$$

$$\sigma_{f} = \frac{2\sigma_{3}^{'} + 2\tan^{2}\phi'\sigma_{3}^{'} + \sigma_{d} + \tan^{2}\phi'\sigma_{d} - \sqrt{\tan^{2}\phi'\sigma_{d}^{2} + \tan^{4}\phi'\sigma_{d}^{4}}}{2\left(1+\tan^{2}\phi'\right)} \tag{6.3}$$

$$\sigma_{d} = \left(\frac{F_{s}}{l_{e}\times l_{b}}\right) - \sigma_{3}^{'} \tag{6.4}$$

$$S = L\cdot\varepsilon_{\mathrm{p}} \tag{6.5}$$

Where, ε_{p} is the permanent axial strain corresponding to N_{c} applications (%); σ_d is the axial deviator stress (kPa); and A, B, C, D are regression parameters. Besides, τ_f and σ_f are the effective shear stress and effective normal stress acting on the failure plane. $\tau_{\max}$ is the effective shear strength determined by monotonic loading triaxial compression tests. ϕ' is effective internal friction angle. l_{e} is the effective length of the sleeper which equal to $2l'$ according to load transfer to ballast assumed by Japanese Standards (Sayeed, 2018). l' is the distance from the central line of rail to the edge of sleeper. l_b is the width of sleeper. L is the thickness of ballast layer. The schematic diagram of sleeper is shown in Figure 3-6 and Figure 6-2. The parameters used in this model are listed in Table 6-1.

Table 6-1 Parameters for UIUC model (Yang et al., 2021)

Parameter	A	B	C	D	τ_{max} (kPa)	σ_3' (kPa)	ϕ'(deg.)
Value	0.1938	0.1306	1.213	6.523	40.73	20	54.7

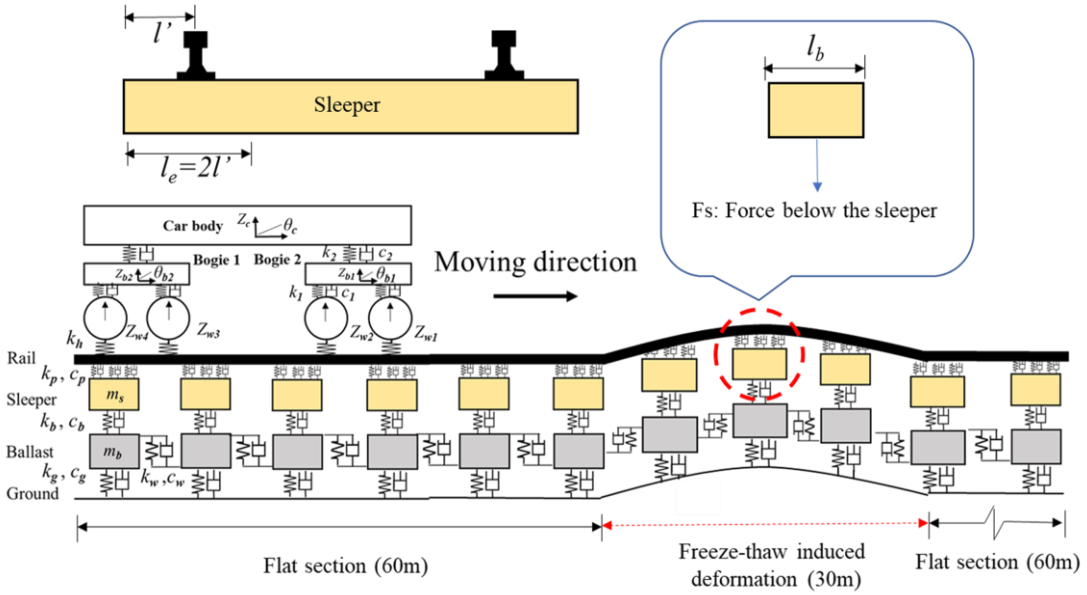

Figure 6-2 Change in vertical displacement of point A and B with surface temperature

As mentioned in chapter 4, Point A and point B are selected for study, and the corresponding deformations and temperatures are depicted in Figure 6-3. Both the point A and point B deformation coincide with the change of temperature. In the early period of freezing, both two points' deformation does not show a clear increasing trend as the temperature decreases due to the high heat capacity of the soil. With the increase of frost penetration depth, the deformation increases significantly after 50 days. It reaches a peak on day 120 when the air temperature becomes positive (as the blue dash line shown in Figure 6-3). The difference of point A deformation and point B deformation also reach to max value while these two points' deformation reaches to max value. As the obvious difference between point A deformation and point B deformation during day 50 to day 150, this study focuses on the this period.

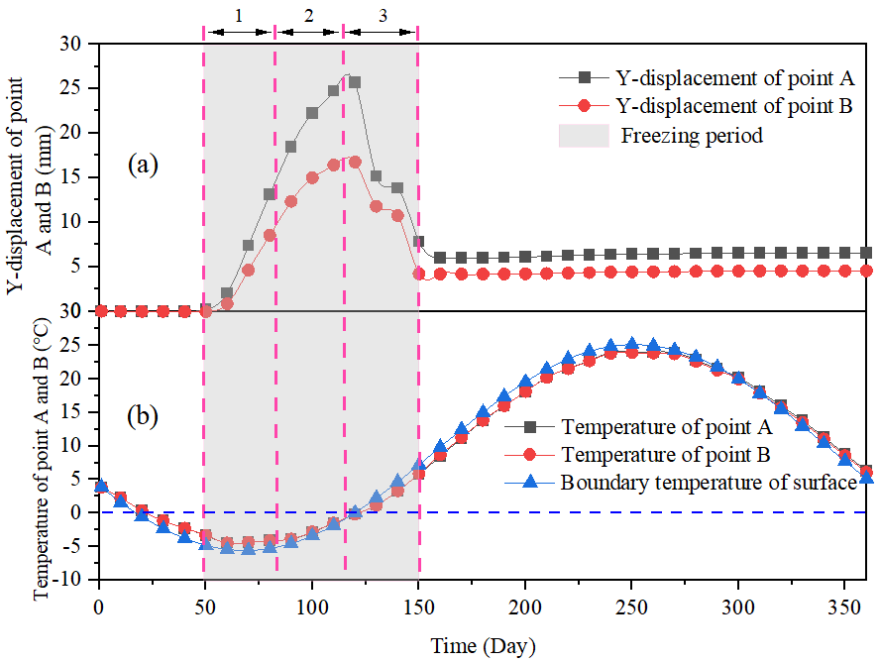

Figure 6-3 Change in vertical displacement of point A and B with surface temperature

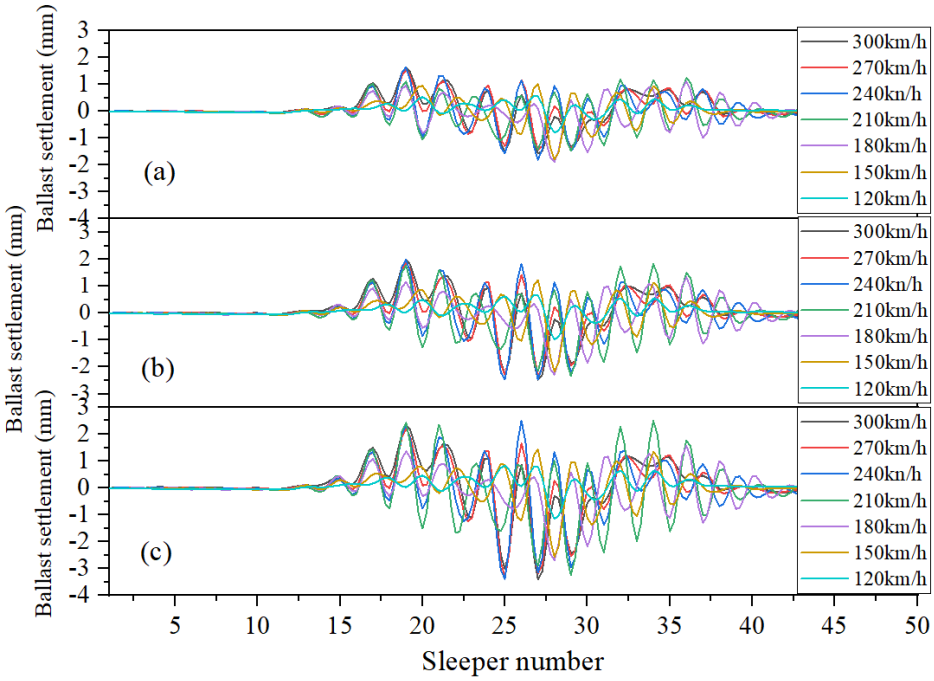

Figure 6-4 Ballast settlement (GWL=18): (a) Ballast settlement in the longitude direction (after first iteration) (b) Ballast settlement (after second iteration) (c) Ballast settlement (after third iteration)

6.2 Stress below Sleeper under Different Train Speed and GWL

The influence of GWL and train speed on stress below sleeper (for convenience, hereinafter called stress) are investigated in the first load cycle and plotted in Figure 6-5. As shown in Figure 6-5, the stress has a larger value at which close to the central. Comparing Figure 6-5. (a), (b) with (c), the max value reached at the 19th sleeper, because the track deformation increases sharply. As shown in Figure 6-5(c), the slope of the deformation reaches the limit of allowable slope in Japanese railway design standard (Railway Technical Research Institute, 2012) at the 19th sleeper. As shown in Figure 6-5 (b), the stress increases when the GWL has a larger value.

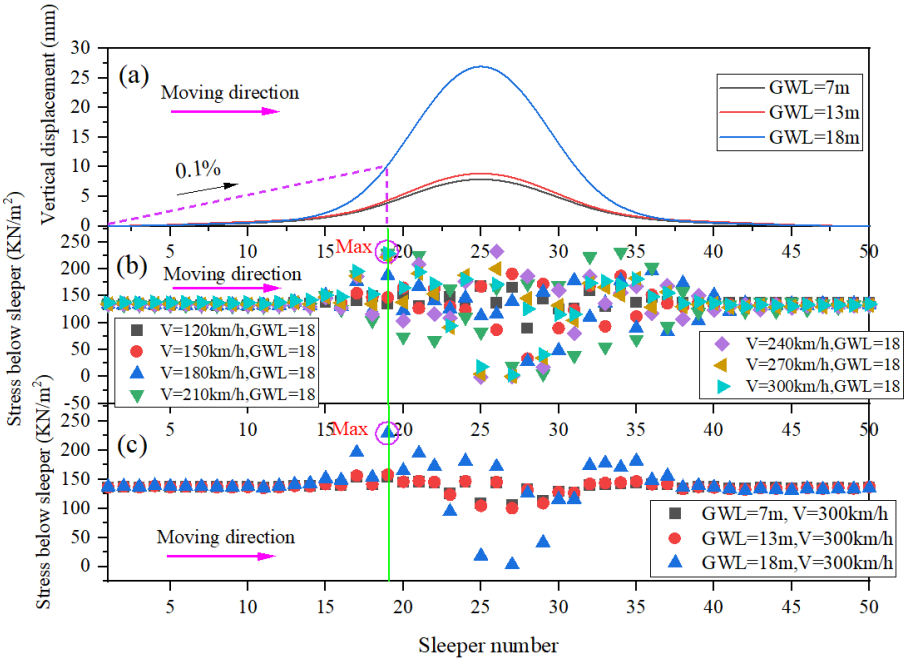

Figure 6-5 Stress below sleeper considering frost heave induced track surface deformation (Day 120): (a) Relative track surface deformation (b) Different train speed, GWL=18 (c) Different GWL, V=300km/h

6.3 Influence of Different Train Speed on Ballast Settlement

The ballast settlement and the final track deformation after freeze-thaw period in the longitude direction are respectively plotted in Figure 6-6 (a) and (b). As shown in Figure 6-6 (b), the final track deformation fluctuates much more at a higher train speed, especially in the central area. To compare these two conditions, the stability of train

operation is estimated by using Sperling index and maximum car body acceleration. As shown in Figure 6-7, compared with the result only considering freeze-thaw induced track surface deformation at the end of thawing period, the final track deformation induces larger car body acceleration and Sperling index. This means that the stability of train operation becomes worse due to the ballast settlement affected by the frost heave of subgrade.

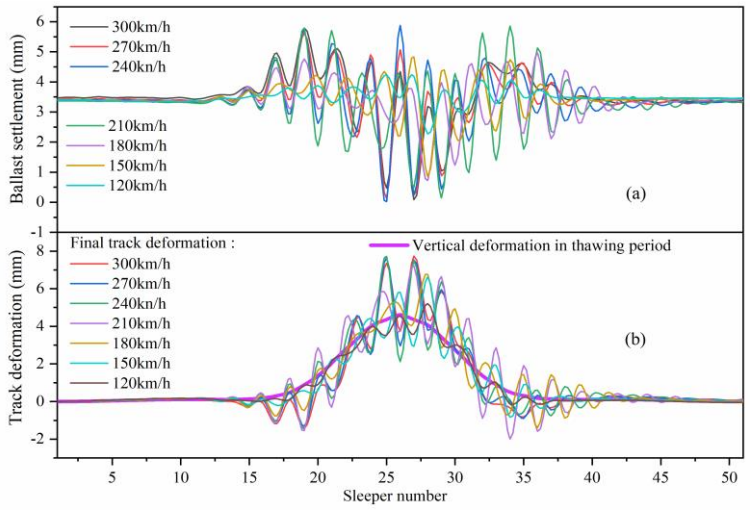

Figure 6-6 Ballast settlement and track surface deformation (a) Ballast settlement in the longitude direction (GWL=18, Day 150) (b) Ballast settlement plus frost heave induced track surface deformation (GWL=18, Day 150)

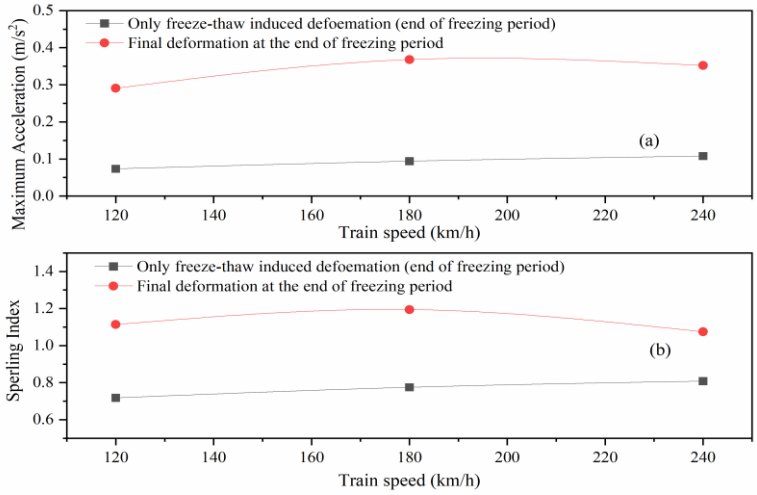

Figure 6-7 Train operation stability (GWL=18, Day 150) (a) Max car body acceleration (b) Sperling index

6.4 Summary of This Chapter

This chapter clarified the influence of frost heave induced track surface deformation on the differential plastic deformation of ballast. The following findings can be mainly observed:

(1) The stress below sleeper increase with GWLs and train speed. The stress below sleeper reaches the max value when the slope of the deformation reaches the limit (0.1%) of allowable value in design standard.

(2) The ballast settlement under each sleeper increases with train speed when the train passes the same track surface deformation. After large number of loading cycles, due to the influence of subgrade frost heave on differential settlement of ballast, the final track deformation leads to worse stability of train operation.

7. CONCLUSIONS AND RECOMMENDATIONS

7.1 Conclusions and Recommendations

The influence of freeze-thaw of the ballasted track on vehicle vibration is investigated based on the THM finite element analysis and vehicle track model. The freeze-thaw induced track surface deformation was inputted into the vehicle-track model as an excitation, and the safety and stability were investigated considering different speed levels. The following conclusions can be summarized:

(1) Frost heave induced total track surface deformation and relative track surface deformation are larger than the value in the thawing period. This indicates that the most unfavorable stage is during the freezing period.

(2) Different types of the culvert transition section are selected to investigate their response to relative track surface deformation in the freeze-thaw period. The result implies that the box culvert transition section is different from the pipe culvert transition section in the response of deformation amplitude and wavelength.

(3) Different GWLs are simulated. The result indicates that the variation trend of deformation amplitude and wavelength for two types of culvert transition section is different with the increase in GWL. It is preliminarily inferred that this is caused by the different boundary conditions produced by different culvert shapes.

(4) The results indicate that higher GWL results in lower the safety and stability of train operation in the freezing period. On the other hand, the effect of freeze-thaw induced track surface deformation on the safety and stability of train operation in the thawing period can be ignored.

(5) Different types of culverts induce different safety and stability of train operation. In this study, the safety and stability are lower at the box culvert case compared with the pipe culvert case. It is feasible to guarantee the safety and stability of train operation by considering the buried structure type.

(6) At a constant GWL, the safety and stability of train operation increase with decreasing train speed. Compared with reduction of train speed, choosing the buried structure type and reducing GWL are effective countermeasures to ensure riding

comfort.

(7) The stress below sleeper has a proportional relationship with GWLs and train speed. The stress below sleeper reaches the max value when the slope of the deformation reaches the limit of allowable value in design standard.

(8) The ballast settlement under each sleeper increases with train speed. Due to the influence of subgrade frost heave on differential settlement of ballast, the final track deformation leads to worse stability of train operation.

Although the verification of the calculated track surface deformation by the present THM model could not be carried out due to the lack of in-situ test data, this study reveals the primary variation trend of track surface deformation under different factors through the THM finite element numerical simulation. Secondly, it reveals the primary variation trend of train vibration when the train passes these track surface deformations through the train vibration analysis. Finally, the influence of frost heave induced track surface deformation on ballast settlement was clarified under different factors.

7.2 Future Assignments

(1) The phenomenon of frost heave may happen in the wet clayey ground during winter in seasonally frozen regions, or in active layers during autumn to winter in permafrost regions. The frost heave induced railway track deformation, which happens in cold regions, is generally understood to occur in subgrade layers. However, scholars confirmed that the upheaval due to frost heaving sometimes happens in the ballast layers [Sato et al., 1995].The reason contributed to the fine materials in the ballast layers consist of clayey minerals and crushed rock-forming minerals of ballast. Scholars performed a series of frost heave tests conducted using crushed rock and fine material. To consider the more comprehensive conditions, the frost heave in the ballast layer need to be considered as one of the future assignment.

(2) Because the vertical track deformation is the main influence factor for the train vibration, in this study, the vehicle-track model, a plane 2D model was adopted to investigate the influence of vertical track deformation on train vibration. To consider the more complex realistic conditions, it is necessary to build a 3D vehicle-track model to consider the influence of more complex track deformation. With the 3D vehicle-track

model, more evaluation indices can be calculated (e.g. derailment factor).

(3) As one type of track structure, the slab track becomes more and more widely used in the high speed railway. Especially, the high speed railway constructed in the cold region needs more theoretical research support to prevent the occurrence of slab track freeze-thaw disaster. Therefore the frost heave induced slab track deformation also needs to be investigated in the future.

(4) Need to consider the more complex and realistic conditions, for instance, the influence of rainfall overall the year and water supply during the freeze-thaw period in the embankment, etc. on the frost heave of the ballasted. Besides, except for the culvert transition section, need to carry out relevant research to reveal the mechanism of frost heave in the normal section.

(5) The influence factors which control frost heave induced track deformation were clarified through the above study. To prevent the occurrence of frost heave on the track, the detailed technical countermeasures (e.g., replacement of non-frost heave soil in the transition section, wrapping insulating material on the outer layer of the culvert) need to be proposed.

LIST OF REFERENCES

1. Andersland, O. B., Ladanyi, B., Frozen ground engineering, second ed., Wile y, Hoboken, NJ, 2003.
2. Akagawa, S., Hori, M., Sugawara, J., Frost heaving in ballast railway tracks, Procedia engineering. 189 (2017) 547-553.
3. Amiri, S. G., Grimstad, G., Gao, H., & Kjelstrup, S. (2021, April). Numeric al modelling of distinct ice lenses in frost heave. In IOP Conference Series: Earth and Environmental Science (Vol. 710, No. 1, p. 012039). IOP Publishi ng.
4. Aikawa, A., Sakai, H., & Abe, K. (2013). Numerical and experimental study on measuring method of rail axial stress of continuous welded rails based on use of resonant frequency. *Quarterly Report of RTRI* 54(2), 118-125.
5. Boushehri, R., Hasanpour Estahbanati, S., & Ghasemi-Fare, O. (2019). Contr olling frost heaving in ballast railway tracks using low enthalpy geothermal energy (No. 19-03687).
6. Cai, X., Liang, Y., Xin T., Ma, C., Wang, H., Assessing the effects of subg rade frost heave on vehicle dynamic behaviors on high-speed railway, Cold Regions Science and Technology. 158 (2019) 95-105.
7. Cheli, F., Corradi, R., On rail vehicle vibrations induced by track unevennes s: Analysis of the excitation mechanism, Journal of Sound and Vibration. 33 0.15 (2011) 3744-65.
8. Dong, S., & Yu, X. (2018). Microstructure-based random finite element meth od simulation of frost heave: theory and implementation. Transportation Rese arch Record, 2672(52), 347-357.
9. Ekevid, T., Li, M. X., & Wiberg, N. E. (2001). Adaptive FEA of wave pro pagation induced by high-speed trains. Computers & Structures, 79(29-30), 26 93-2704.
10. Eugenio Oñate.., Structural Analysis with the Finite Element Method. Linea r Statics: Volume 2: Beams, Plates and Shells, Springer Netherlands, 2016
11. Ferrara, R., A Numerical Model to Predict Train Induced Vibrations and D ynamic Overloads, PhD thesis, University of Reggio Calabria and University Montpellier 2, 2014.

12. Ford, R. (1995). Differential ballast settlement and consequent undulations i n track caused by vehicle-track interaction. *Vehicle System Dynamics* 24(sup1), 222-233.
13. Fu, M., Li, P., Liang, X. F., Numerical analysis of the slipstream developm ent around a high-speed train in a double-track tunnel. PloS one, 2017, 12.3 : e0175044.
14. Fukami, H., On the Fluctuation of Unconfined Groundwater Level for Sno w Period in Snowy Cold Region, Geophysical Bulletin of Hokkaido Universi ty. 75 (2012) 15-24.
15. Guo, Y., Wanming, Z., Long-term prediction of track geometry degradation in high-speed vehicle–ballastless track system due to differential subgrade set tlement, Soil Dynamics and Earthquake Engineering. 113 (2018) 1-11.
16. Germonpré, M., Nielsen, J. C. O., Degrande, G., Lombaert, G., Contributio ns of longitudinal track unevenness and track stiffness variation to railway i nduced vibration, Journal of Sound and Vibration. 437 (2018) 292-307.
17. Hua, L., Fujun, N., Yonghong, N., Xifeng, Y., Study on thermal regime of roadbed–culvert transition section along a high-speed railway in seasonally fr ozen regions, Cold Regions Science and Technology. 106 (2014) 216-231.
18. Hirotsu, T., Terada, K., Hiraishi, M., Yui, S., Simulation of hunting of rail vehicles: The case using a compound circular wheel protile, JSME internati onal journal. Ser.3, Vibration, control engineering, engineering for industry, 3 4.3 (1991) 396-403.
19. Hashiguchi K, Ueno M. Elastoplastic constitutive laws of granular materials . Constitutive Equations of Soils (Proc. 9th Int. Conf. Soil Mech. Found. En g., Spec. Ses.9), Tokyo, JSSMFE, 73-82, 1977.
20. Ishikawa, T., Tokoro, T., Akagawa, S., Frost heave behavior of unsaturated soils under low overburden pressure and its estimation, Proceedings of GEO Quebec (2015).
21. Ishikawa, T., Kijiya, I., Tokoro, T., Sato, M., Application of coupled therm o-hydro-mechanical analysis to frost-heave behavior of earth structures, Japan ese Geotechnical Society Special Publication. 2.13 (2016) 531-6.
22. Ishikawa, T., Kijiya, I., Tokoro, T., Evaluation of frost heave-thaw behavior

pavement with coupled thermo-hydro-mechanical analysis, Proceedings of th e Civil Engineering Society. 71 (2015) 185-192.

23. Ishikawa, T., Kijiya, I., Tokoro, T., Sato, M., Numerical experiments on fre eze-thaw of soils with coupled thermo-hydro-mechanical FE analysis, In: Pro ceedings of the 14th International Conference of the International Association for Computer Methods and Advances in Geomechanics, Kyoto, 2014, pp. 4 15-420.
24. Ishida, H., Masaki, M., Safety criteria for evaluation of railway vehicle der ailment, Quarterly Report of RTRI 40.1 (1999): 18-25.
25. Iwan WD. On a class of models for the yielding behavior of continuous a nd composite systems. Journal of Applied Mechanic, 1967; 34(3): 612-617.
26. Japanese Geotechnical Society. In Japanese Geotechnical Society Standards-Laboratory Testing Standards of Geomaterials, Tokyo, 2015. (in Japanese)
27. Jeon, B. G., Kim, N. S., Kim, S. I., Estimation of the vibration serviceabil ity deflection limit of a high-speed railway bridge considering the bridge-trai n interaction and travel speed, KSCE Journal of Civil Engineering. 20.2 (201 6) 747-761.
28. Jing Z., Pingbo W., Study on the wheel/rail interaction and derailment safe ty, Wear. 265.9-10 (2008) 1452-1459. https://doi.org/10.1016/j.wear.2008.01.031 .
29. Jinsong Z., Railway Vehicle Vibration and Control, Bei Jing, 2012.
30. Koike, Y., Nakamura, T., Hayano, K., Momoya, Y., Numerical method for evaluating the lateral resistance of sleepers in ballasted tracks, soils and Fou ndations, 54.3 (2014) 502-514.
31. Lei, X., Noda, N. A., Analyses of dynamic response of vehicle and track coupling system with random irregularity of track vertical profile, Journal of sound and vibration. 258.1 (2002) 147-165.
32. Liu, H., Maghoul, P., Shalaby, A., & Bahari, A. (2019). Thermo-hydro-mec hanical modeling of frost heave using the theory of poroelasticity for frost-s usceptible soils in double-barrel culvert sites. Transportation Geotechnics, 20, 100251.
33. Lai, Y., Pei, W., Zhang, M., & Zhou, J. (2014). Study on theory model of

hydro-thermal–mechanical interaction process in saturated freezing silty soil. International Journal of Heat and Mass Transfer, 78, 805-819.

34. Luo, B., Lai, H., Ishikawa, T., Tokoro T., Frost heave analysis of ballasted track above box culvert and its influence on train vibration, Sciences in Co ld and Arid Regions. 9.3 (2018) 229-35.
35. Li, D., & Selig, E. T. (1996). Cumulative plastic deformation for fine-grain ed subgrade soils. Journal of geotechnical engineering, 122(12), 1006-1013.
36. Lin, Z., Niu, F., Li, X., Li, A., Liu, M., Luo, J., Shao, Z., Characteristics and controlling factors of frost heave in high-speed railway subgrade, North west China, Cold Regions Science and Technology. 153 (2018) 33-44.
37. Luo, B., Ishikawa, T., Tokoro, T., Lai, H., Coupled thermo-hydro-mechanic al analysis of freeze–thaw behavior of pavement structure over a box culvert , Transportation Research Record. 2656.1 (2017) 12-22.
38. Niu, F., Li, A., Luo, J., Lin, Z., Yin, G., Liu, M., Zheng, H., Liu, H., Soi l moisture, ground temperatures, and deformation of a high-speed railway e mbankment in Northeast China, Cold Regions Science and Technology.133 (2017) 7-14.
39. Nishimura, S., Gens, A., Olivella, S., & Jardine, R. J. (2009). THM-couple d finite element analysis of frozen soil: formulation and application. Géotech nique, 59(3), 159-171.
40. Niemunis, A., Wichtmann, T., & Triantafyllidis, T. (2005). A high-cycle ac cumulation model for sand. Computers and geotechnics, 32(4), 245-263.
41. Okayasu T, Nakamurab T, Muramoto K, Momoya Y. Elastoplastic deformati on behavior for ballast under monotonic and cyclic loading conditions. Proce edings of the 18th International Conference of the ISTVS, Seoul, Korea, 20 14.
42. Peckover, F. L. (1978). Frost heaving of track--causes and cures. Area Bull etin, 79(Proceeding).
43. Pylkkänen, K., Luomala, H., Guthrie, W. S., Nurmikolu, A., Real-time in s itu monitoring of frost depth, seasonal frost heave, and moisture in railway t rack structures, In Cold Regions Engineering 2012: Sustainable Infrastructure Development in a Changing Cold Environment. (2012) 446-455.

44. Qamhia, I., Tutumluer, E., Chow, L. C., & Mishra, D. (2016). A framework to utilize shear strength properties for evaluating rutting potentials of unbound aggregate materials. Procedia engineering, 143, 911-920.
45. Rempel, A. W., Wettlaufer, J. S., & Worster, M. G. (2004). Premelting dynamics in a continuum model of frost heave. Journal of fluid mechanics, 498, 227-244.
46. SHENG, D. C., ZHANG, S., NIU, F. J., & Cheng, G. (2014). A potential new frost heave mechanism in high-speed railway embankments. Géotechnique, 64(2), 144-154.
47. Sayeed, M. A., Shahin, M. A., Design of ballasted railway track foundations using numerical modelling, Part I: Development. Canadian geotechnical journal, 55.3 (2018) 353-368.
48. Sun, Y. Q., & Dhanasekar, M. (2002). A dynamic model for the vertical interaction of the rail track and wagon system. International journal of solids and structures, 39(5), 1337-1359.
49. Sato, Y. (1995). Japanese studies on deterioration of ballasted track. *Vehicle system dynamics* 24(sup1), 197-208.
50. Shenton, M. J. (1985). Ballast deformation and track deterioration. *Track technology* 253-265.
51. Tai, B., Liu, J., Wang, T. Shen, Y., Li, X., Numerical modelling of anti-frost heave measures of high-speed railway subgrade in cold regions, Cold Regions Science and Technology.141 (2017) 28-35.
52. Thom, N., and J. Oakley. (2006). Predicting differential settlement in a railway trackbed. *Proceedings of Railway foundations conference: Railfound*. Vol. 6. 190-200.
53. Tokoro, T., Tatsuya I., Shoya S., Tsutomu N., Estimation methods for thermal conductivity of sandy soil with electrical characteristics, Soils and Foundations. 56.5 (2016) 927-936.
54. Tong, F., Gao, L., Cai, X., Zhong, Y., Zhao, W., & Huang, Y. (2019). Experimental and theoretical determination of the Frost-Heave cracking law and the crack propagation criterion of slab track with water in the crack. Applied Sciences, 9(21), 4592.

55. Wu X., Niu F., Lin Z., Luo J., Zheng H., Shao Z., Delamination frost hea ve in embankment of high speed railway in high altitude and seasonal froze n region, Cold Regions Science and Technology.153 (2018) 25-32.
56. Wang H., Markine V., Modelling of the long-term behavior of transition zo nes: Prediction of track settlement, Engineering structures.156 (2018) 294-304 .
57. Wei, L., Zeng, J., Wu, P., Song, C., Safety analysis of high speed trains u nder cross winds using indirect wheel-rail force measuring method, Journal o f Wind Engineering and Industrial Aerodynamics. 183 (2018) 55-67.
58. Xia, H., Traffic induced environmental vibrations and controls: theory and a pplication, Bei Jing, 2013.
59. Xiao, X., Jin, X., Deng, Y., Zhou, Z., Effect of curved track support failur e on vehicle derailment, Vehicle System Dynamics, 46(11) (2008): 1029-1059.
60. Youcef, K., Sabiha, T., El Mostafa, D., Ali, D., Bachir, M., Dynamic analy sis of train-bridge system and riding comfort of trains with rail irregularities , Journal of Mechanical Science and Technology. 27.4 (2013) 951-962.
61. Yang, J., Ishikawa, T., Lin, T., Tokoro, T., Nakamura, T., & Momoya, Y. (2021). Influence of aging on hydro-mechanical behavior of unsaturated ballas t. *Transportation Geotechnics* 27, 100480.
62. Yang Guotao. Research on frost heave mechanism and track smoothness co ntrol of subgrade bed surface of high-speed railway in alpine regions. Diss. Beijing Jiaotong University, 2020.
63. Yatsumoto, H., Mitsuyoshi, Y., Sawamura, Y., Kimura, M., Evaluation of se ismic behavior of box culvert buried in the ground through centrifuge model tests and numerical analysis, Underground space, 4.2 (2019) 147-167.
64. Zhang, S., Sheng, D., Zhao, G., Niu, F., He, Z., Analysis of frost heave mechanisms in a high-speed railway embankment, Canadian Geotechnical Jou rnal. 53.3 (2016) 520-529.
65. Zhai, W., He, Z., Song, X., Prediction of high-speed train induced ground vibration based on train-track-ground system model, Earthquake Engineering and Engineering Vibration. 9.4 (2010) 545-54.
66. Zhu, Z. Y., Ling, X. Z., Chen, S. J., Zhang, F., Wang, L. N., Wang, Z. Y.

, Zou, Z. Y., Experimental investigation on the train-induced subsidence prediction model of Beiluhe permafrost subgrade along the Qinghai–Tibet railway in China, Cold regions science and technology. 62.1 (2010): 67-75.

67. Zhai, W. M., Wang, K. Y., Lin, J. H., Modelling and experiment of railway ballast vibrations, Journal of sound and vibration. 270.4-5 (2004) 673-683.
68. Zhai W. M., Vehicle-track coupled dynamics, fourth ed., Bei Jing, 2015.
69. Zhang, J., Gao, Q., Tan, S. J., Zhong, W. X., A precise integration method for solving coupled vehicle–track dynamics with nonlinear wheel–rail contact, Journal of Sound and Vibration. 331.21 (2012) 4763-4773.
70. Zhang, Y., White, D. J., Vennapusa, P. K., Johnson, A. E., & Prokudin, M. M. (2018). Investigating Frost Heave Deterioration at Pavement Joint Locations. Journal of Performance of Constructed Facilities, 32(2), 04018001.
71. Zhai, W., & Cai, Z. (1997). Dynamic interaction between a lumped mass vehicle and a discretely supported continuous rail track. Computers & structures, 63(5), 987-997.
72. Zhai, W., & Sun, X. (1994). A detailed model for investigating vertical interaction between railway vehicle and track. Vehicle system dynamics, 23(sup1), 603-615.
73. Zhu Zhanyuan. Vibration response and vibration subsidence prediction of subgrade in permafrost sites for trains on Qinghai-Tibet Railway. 2009. Harbin Institute of Technology, PhD dissertation. (In Chinese)

LIST OF NOTATIONS

Fitting parameter	a
Acceleration of car body	a_v
Maximum car body acceleration	a_{vmax}
Temperature amplitude	A
Amplitude of frost heave	A_0
Fitting parameter	c
Volumetric heat capacity of soil	C_T
Volumetric heat capacity of soil particles	C_{Tp}
Volumetric heat capacity of water	C_{Tw}
Vehicle damping matrix	C_v
The substructure damping matrix	C_{sub}
Rubber pad damping	c_p
Ballast damping	c_b
Ground damping	c_g
Horizontal ballast damping	c_w
Damping contact coefficient	c_h
Elastic constant tensor	D_{ijkl}
Fitting parameter	d
Young's modulus	E
Young's modulus of ballast	E_b
K_{30} modulus of roadbed	E_f
Frequency correction factor	$F(f)$
Frequency	f
Forces vector	$f_{sub/v}$
Forces vector	$f_{v/sub}$
The acceleration in the *i* direction	g_i
Gravity matrix	g_v
Gravity matrix	g_{sub}
Thickness of ballast	h_b
Bulk modulus for the soil structure	K
Bulk modulus for the soil structure under undrained condition	K_u
Bulk modulus for the soil structure under drained condition	K_d
The reciprocal of volume elastic constant of the pore water in the unsaturated region	K_b
Fitting parameter	k_f
Vehicle stiffness matrix	K_v
Rubber pad stiffness	k_p

Ballast stiffness	k_b
Ground stiffness	k_g
Horizontal ballast stiffness	k_w
Hertzian contact stiffness coefficient	k_h
Coefficient of water permeability when mean effective stress equals 0	k_0
Permeability	k_s
Wavelength of frost heave	l
Sleeper spacing	l_s
Effective supporting length of half sleeper	l_e
Width of sleeper underside	l_b
Latent heat of fusion of water	L
Track length	L_t
Storage volume of water per unit volume	m
Water absorption	m_w
Vehicle mass matrix	M_v
Sleeper mass	m_s
Ballast mass	m_b
The substructure mass matrix	M_{sub}
Porosity	n
Corresponding period	p
Wheel load reduction	ΔP
Average wheel-rail force	P_0
Wheel rail contact force	$R_{w/r}$
Degree of saturation for liquid water	S_w
Saturated degree of saturation	S_{rs}
Residual degree of saturation	S_{rr}
Initial degree of saturation	S_{w0}
Average initial degrees of saturation	S_0
Temperature	T
Final freezing temperature	T_f
Temperature of ground surface or culvert	T_s
Mean annual air temperature	T_m
Time	t
Initial phase	t_0
Time step in train vibration analysis	t_{step}
Temperature increment induced by boundary layer	ΔT
Displacement tensor	$u_{k,l}$, $u_{l,k}$
Pore-water pressure	u_w

Cooling rates	U
Poisson's ratio	υ
Flux vector of water	v_w
Train speed	V
Sperling index	W
Longitudinal position of subgrade surface	x
Fitting parameters	x_0 , y_0
Frost heave induced relative deformation	y
Fitting parameters	y_0
Depth below the air temperature boundary	z
Vehicle displacement vector	z_v
Substructure displacement vector	z_{sub}
Vertical displacement of vehicle body	z_c
Vertical displacement of bogies	z_{b1} , z_{b2}
Vertical displacements of the four wheels	z_{w1} , z_{w2} , z_{w3} , z_{w4}
Total deflection of wheel and rail at the contact point	z_h
Substructure displacement vector	z_{sub}
Dry density of soil	ρ_d
Density of ballast	ρ_b
Wet density of soil	ρ
Density of water	ρ_w
Thermal conductivity of soil	λ_T
Van Genuchten-Mualem fitting parameter	λ
Van Genuchten-Mualem fitting parameter	α
Thermal expansion coefficient under undrained condition	α_{Tu}
Thermal expansion coefficient of water	α_{Tw}
Thermal diffusivity	α_u
Maximum frost expansion strain	ε_{fmax}
Frost expansion strain	ε_f
Thaw contraction strain	ε_t
Volumetric strain of soil element	ε_v
Fitting parameter	ς
Matric suction	ψ
Ballast stress distribution angle	φ
Kronecker delta	δ_{ij}
Mean total normal stress	σ_m
Mean effective stress	σ'_m
Total stress at the direction of heat flow	σ_n

Effective stress at the direction of heat flow	σ'_n
Overburden pressure	σ_a
Volumetric ice content	θ_i
Pitch of vehicle body	θ_c
Pitch of two bogies	θ_{b1} , θ_{b2}

APPENDIX

Main_program_start.m

```
zz = 3;      % Used for select the vehicle speed

 for runtime = 1 %:18  % Number of simulation loops-----zsl-2020.0318

    cnt3 = 1;    % Main simulation loop counter

    for cnt= zz  % Vehicle type in each simulation loop

        tic      % Starting time for each vehicle sim loop

        disp(['runtime ',num2str(runtime),', cnt ',num2str(cnt)]);  % Display
runtime and vehicle sim counter

        if cnt==1
            V = 20;
            VehicleProperties_CRH3_ZSL

        elseif cnt==2
            V = 40;
            VehicleProperties_CRH3_ZSL

        elseif cnt==3                   %zsl-2020.0318
            V = 60;                     %zsl-2020.0318
            VehicleProperties_CRH3_ZSL    %zsl-2020.0318

        elseif cnt==4
            V = 80;
            VehicleProperties_CRH3_ZSL

        elseif cnt==5                       % ZSL-2020.0326
            V = 100;                        % ZSL-2020.0326
            VehicleProperties_CRH3_ZSL      % ZSL-2020.0326

        elseif cnt==6                       % ZSL-2020.0318
            V = 120;                        % ZSL-2020.0318
            VehicleProperties_CRH3_ZSL      % ZSL-2020.0318
```

```
%              VehicleProperties_MAYA_ZSL
%              VehicleProperties_varification_ZSL
        end



        AssigningValues       % Assigns vehicle, simulation, hertz contact, rail,
                              % sleeper, rubber pad, ballast and subgrade
parameters.
%% Substructure parameters

SubstructureProperties_ModelVerification2_CRH    % For IR properties
% SubstructureProperties_ModelVerification1      % For Case 2: Wheel Flat
% SubstructureProperties_ModelVerification       % For Case 1
% SubstructureProperties_ModelVerification2_Zhai % For Zhai

        VehicleMatrix         % Forms vehicle mass (Mv), stiffness (Kv), damping
(Cv) and
                              % force matrix (Fv) depending upon number of wheels
(Nw)
                              % present in vehicle model.

        InitialCalculations   % Calculates some parameters needed for finite
element model


            RailIrrData = zeros(1,m);                   % m: number of sleeper
            Kb = Kb*ones(1,m);                          % Kb--ballast stiffness
            Ef = Ef*ones(1,m);                          % Ef—subgrade
modulus     %[ones(1,30),100*ones(1,28),ones(1,30)];    %ones(1,m);
            Kf = Kf*ones(1,m);                          % Kf--subgrade
stiffness   %[ones(1,30),100*ones(1,28),ones(1,30)];
            Kp = Kp*ones(1,m);                          % Kp--Rubber Pad stiffness
2020.0320  ZSL
%              Kp = Kp*[ones(1,30),10*ones(1,28),ones(1,30)]; % ones(1,m);  If the
simL is 52m, so,total sleeper No.is 88.----2020.0320  ZSL

%%%%%%%%%%%%%%%%%%%%%%%%%%%%%%%%%%%%%%%%%%%%%%%%%%%%%%%%%%%%%%%%%%%%%%%%%%%%%%%%%%%%%%%%
%%%%%%%%%%
        SubMatrices

%          sumNcyl(cnt5 + 1) = sumNcyl(cnt5) + Ncyl;     %2020.0326
```

```
%         Rail_unevenness = 1;    % 2020.0412 ZSL

        PreMatrices % Calculates Av matrix for Newton-Raphson method and Keff
matrix
                    % for Newmark integration method

        InitialisingNodalDisplacements % Initialising nodal displacements for rail
                                       % and vehicle and variables related to wheel
                                       % position

        MainStepsLoop

        % for ploting Sperling stability coeffecient-----2020.0409.ZSL

        % plot_fig                        % for ploting result ----zsl

    end  % zsl-2020.0318
 end    %  zsl-2020.0318
        toc
```

VehicleProperties_CRH3_ZSL.m

```
% VehicleName = 'Case2Wagon¥n';
% Ncyl = 37230; % number of load cycles in one year   % no need to do cycles(zsl)
Nw = 4;       % number of wheels
VDof = 6+Nw;  % number of degrees of freedom

mc = 48000/2; % 48000/2 is for CRH    % mass of car body kg      -----
mt = 3200/2;  % 3200/2 for CRH % mass of truck kg         -----
mw = 2400/2;  % mass of one wheel set kg -----
rw = 0.46;    % new wheel radius m       -----
Lcb = 20.7;   % length of car body m     -----
Hcb = 4.05;   % 3.89  %2.34 + (1.654-1.090); % height of car body m      -----
Jc = mc/12*(Lcb^2 + Hcb^2); % rotational inertia of car body kgm^2   -----
ZSL.2020.0310
Ltr = 3.36;   % length of truck m     Wheel rolling circle diameter 0.86 m -----
Htr = 0.25;   % height of truck m
Jt = mt/12*(Ltr^2 + Htr^2); % rotational inertia of truck kgm^2    -----
ZSL.2020.0310
lw = 2.5/2;   % half of wheel base m   ----- axle distance
ltx = 17.5/2; % half of distance between c/l of bogie and c/l of coach m     -----
Half of bogie distance
```

```
k2 = 0.4e6;   %6.12e5+2.32e5; %35.13e6; %35e05; %35.42e6; % secondary spring
stiffness N/m   -----
k1 = 1.04e6;  % 1.04e6; %(11.06e5 + 11.5e6); % primary spring stiffness N/m     ---
--
c2 = 50e3;    % secondary damping constant Ns/m          -----
c1 = 45e3;    % primary damping constant Ns/m            -----
axleDis = [0;2.5;17.5;20]; % distance of each axle from coach start m
                           % [1.83;4.13;12.98;15.28] is for YAMA34
                           % [0;2.5;17.5;20] is for CRH
g =9.81;      %------ZSL.2020.0310
```

AssigningValues.m

```
%% Simulation Parameters
s1=101;         % s1, s2 denote start and stop sleeper number
s2=151;
simL=150;

v = V/3.6;      % m/s
dFStt = 1;      % 5; % Distance of sim start from left end m
dFStp = 0;      % 5; % Distance of sim stop from right end m
% dFStp = 1;      % 5; % Distance of sim stop from right end m
slprI = 60/100; % Unit:m  % sleeper distance

dt = 5e-5;      % Unit:  s    % simL/v/d; d - no. of steps in short wavelength
defects

% % % if V<=60
% % % dt = 0.00125/v/(2.75+  (1-2.75)/(60-20)*(V-20)); % Calculating simulation
time step
% % % else
% % %     dt=0.00125/v;
% % % end

T_preload = 0.5;  % preload time   Unit: S
stepsPRELOAD = round(T_preload/dt);
T_postload = 0;
stepsPOSTLOAD = round(T_postload/dt);

%% Rail Unevenness Parameters

Rail_unevenness = 1;
```

```
% Rail_unevenness = 0; % 0- no rail defect, 1 - rail defect
%
RUType = 'FT_Deformation';            % Freeze Thaw induced subgrade deformation,
used in paper;
% RUType = 'TRC';                       % If TRC data , RUType = 'TRC';
% RUType = 'FrostHeave';                % If Frost Heave, RUType = 'FrostHeave';  %
Reliability_Cai
% RUType = 'WheelFlat';                 % If Wheel Flat, RUType = 'WheelFlat';
% RUType = 'Isolated';                  % If Isolated Dip or Rise, RUType =
'Isolated';   ---P27  Dipped joint
% RUType = 'DifferentialHeight';        % If Differential Height Difference, RUType
= 'DifferentialHeight'---P28  jagged joint

%% Track Receptance Calculation
TrackRecepCal = 'No';  % If track receptance calculation is wanted then 'Yes'

%% Newmark beta method parameters and Permissible error
% if beta = 1/4, gamma = 1/2 => Constant acceleration method
% if beta = 1/6, gamma = 1/2 => Linear acceleration method
% if beta = 0, gamma = 1/2 => Central difference method

% For LINEAR structural dynamics:
% -> for gamma < 1/2, Newmark beta method is conditionally stable, depending
% upon timestep value dt
% -> for 2*beta >= gamma >= 1/2, Newmark beta method is unconditionally stable
% for all values of timestep dt
%.............................
% for gamma = 1/2, Newmark beta method is atleast 2nd order accurate
% for gamma ~= 1/2, Newmark beta method is 1st order accurate

% alfa = beta, delta = gamma

beta = 1/4;    % Newmark constant acceleration method applicable here
gamma = 1/2;

err = 1e-4; % Permissible error in solution

%% Hertz contact parameters
Re = rw;     % wheel radius
Ew = E;      % wheel modulus of elasticity N/m^2
muw = muu;   % wheel Poisson's ratio
```

```
%Kh = 4/3 * Ew/2/(1-muw^2) * sqrt(Re); %1e11; % contact stiffness coefficient
Tutorial Taylor Brian
Kh = 0.87*10^11;
Ch = 0; %3e5;    % contact damping coefficient
```

SubstructureProperties_ModelVerification2_CRH.m

```
%% 60kg rail properties

mr = 60.64; % rail mass per unit length kg/m
E = 2.07e11; % rail modulus of elasticity N/m^2
muu = 0.3; % 0.27; %0.3; % Poisson's ratio
G = E/2/(1+muu); % shear modulus of elasticity N/m^2
I = 3.217e-5; % modulus of inertia m^4
EI = E*I; % modulus of rigidity Nm^2
A = 66.15e-4; % rail cross-section area m^2
chi = 0.34; % Timoshenko coefficient
eleMRP = 9; % eleMRP: number of beam elements in one main rail panel (MRP)
railHt = 172/1000;  % refer to substructureproperties_IR    2020.0320---ZSL  in
fact, it is not used
%% Rubber Pad Properties

eleHRP = 3;    % number of beam elements in half rubber pad (HRP)
Kp = 120e6;    % RP stiffness N/m           50-300MN/m
Kp = Kp/(2*eleHRP+1);   % Kp for area contact model
Cp = 7.5e4;    %% RP damping constant Ns/m    20?80KNs/m
Cp = Cp/(2*eleHRP+1); % Cp for area contact model
Pw = 0.17;             % pad width m
padHt = 6/1000;        % pad thickness m      2020.0320---ZSL  In fact, it is not
used
%% Sleeper properties

ms = 237;        % mass of sleeper kg
ms = ms/2;       % mass of sleeper for half train-track model = 33 kg
lslp = 2.750;    % sleeper length m
bs = 0.273;      % width of sleeper m
slprHt = 0.235; % height of sleeper m   2020.0320---ZSL  In fact, it is not used


%% Ballast properties

tan_phi = 1.5/1;    % ballast angle (H:V)
```

```
hb = 0.3;           % height of ballast m
Bsr = 50e6;         % N/m^3 Coefficient of ballast N/cm^3.....track substructure
response
                    % in terms of surface pressure between sleeper and ballast
                    % and vertical settlement under load. 1 N/cm3 = 1 N/cm2 surface
pressure
                    % when sleeper subsides by 1cm
h0 = hb - (slprI - bs)/(2*tan_phi) ;  % Height of overlapping ballast   2020.0320---ZSL
Eb = 130e6;         % modulus of elasticity of ballast N/m^2
rowb = 1200;        % density of ballast kg/m^3
Kb = 240e6;         % 2*tan_phi*(lslp-bs)*Eb/log((lslp*(2*tan_phi*hb +
bs))/(bs*(2*tan_phi*hb + lslp))); %24e7  % Ballast Stiffness N/m
Kb = Kb/2;          % ballast stiffness N/m
mb = rowb*hb*(lslp*bs + (lslp+bs)*hb*tan_phi + 4/3*hb^2*tan_phi^2);
%mb = 683;           % rowb*hb*(lslp*bs + (lslp+bs)*hb*tan_phi +
4/3*hb^2*tan_phi^2); % mass of vibrating ballast kg
mb = mb/2;          % mass of vibrating ballast for half train-track model = 700 kg
Kw = 78.4e6;        % 0.3*Kb;     % horizontal stiffness between ballast
N/m  %7.84e7;
Cb = 58.8e3;        % ballast damping constant Ns/m
Cw = 0.3*Cb;        %80e3;  % 0.3*58.8e3; %80e3; % horizontal damping between
ballast Ns/m

%% Subgrade Properties

Ef = 50e6; % 50e6; % modulus of subgrade reaction N/m^3    %28e6;
Kf = 65e6; %(lslp + 2*bs*tan_phi)*(bs+2*lslp*tan_phi)*(Ef/0.36);  % subgrade
stiffness N/m
Kf = Kf/2;
Cf = 31.2e3; % subgrade damping constant Ns/m

%% Overlapping   added on 2020.0320---ZSL
%
if h0 > 0

    Kb1 =  2*(lslp-bs)*tan_phi*Eb/log(lslp*slprI/(bs*(lslp+slprI-bs)));

    Kb2 = slprI*(slprI - bs + 2*lslp + 2*hb*tan_phi)*tan_phi*Eb/(bs - slprI +
2*hb*tan_phi);

    Kb = Kb1*Kb2/(Kb1+Kb2);
```

```
    Kb = Kb/2;

    mb = rowb*(bs*hb*(lslp + hb*tan_phi) + lslp*(hb^2 - h0^2)*tan_phi + (4/3)*(hb^3
- h0^3)*tan_phi^2);

    mb = mb/2;

    Kf = slprI*(lslp + 2*hb*tan_phi)*Ef;

    Kf = Kf/2;

    Kw = 0.3*Kb;
end
%}
```

VehicleMatrix.m

```
g = 9.8; % acceleration due to gravity m/s^2

if VDof == 12
    Mv = diag([mc Jc mt Jt mt Jt mw mw mw mw mw mw]);

    Kv = [2*k2 0          -k2     0                -k2     0                0
0        0      0       0    0;
          0    2*k2*ltx^2 -k2*ltx 0                k2*ltx  0                0
0        0      0       0    0;
          -k2  -k2*ltx    k2+3*k1 0                0       0                -k1
-k1      -k1    0       0    0;
          0    0          0       k1*(lw1^2+lw3^2) 0       0                -k1*lw1
0        k1*lw3 0       0    0;
          -k2  k2*ltx     0       0                k2+3*k1 0                0
0        0      -k1     -k1  -k1;
          0    0          0       0                0       k1*(lw1^2+lw3^2) 0
0        0      -k1*lw3 0    k1*lw1;
          0    0          -k1     -k1*lw1          0       0                k1
0        0      0       0    0;
          0    0          -k1     0                0       0                0
k1       0      0       0    0;
          0    0          -k1     k1*lw3           0       0                0
0        k1     0       0    0;
```

```
          0    0          0       0                -k1     -k1*lw3          0
0        0      k1      0    0;
          0    0          0       0                -k1     0                0
0        0      0       k1   0;
          0    0          0       0                -k1     k1*lw1           0
0        0      0       0    k1];

    Cv = [2*c2 0           -c2     0                -c2     0                0
0        0      0       0    0;
          0    2*c2*ltx^2 -c2*ltx  0                c2*ltx  0                0
0        0      0       0    0;
          -c2  -c2*ltx     c2+3*c1 0                0       0                -c1
-c1      -c1    0       0    0;
          0    0          0       c1*(lw1^2+lw3^2) 0       0                -
c1*lw1 0        c1*lw3 0       0    0;
          -c2  c2*ltx      0       0                c2+3*c1 0                0
0        0      -c1     -c1  -c1;
          0    0          0       0                0       c1*(lw1^2+lw3^2) 0
0        0      -c1*lw3 0    c1*lw1;
          0    0          -c1     -c1*lw1          0       0                c1
0        0      0       0    0;
          0    0          -c1     0                0       0                0
c1       0      0       0    0;
          0    0          -c1     c1*lw3           0       0                0
0        c1     0       0    0;
          0    0          0       0                -c1     -c1*lw3          0
0        0      c1      0    0;
          0    0          0       0                -c1     0                0
0        0      0       c1   0;
          0    0          0       0                -c1     c1*lw1           0
0        0      0       0    c1];

    Fv = [mc; 0; mt; 0; mt; 0; mw; mw; mw; mw; mw; mw]*g;

elseif VDof == 10
    Mv = diag([mc Jc mt Jt mt Jt mw mw mw mw]);
    %Mv = diag([14400 6.7505e5 1800 2.5669e3 1800 2.5669e3 250 250 250 250]);

    Kv = [2*k2  0          -k2      0         -k2      0          0      0        0
0;
          0     2*k2*ltx^2 -k2*ltx  0         k2*ltx   0          0      0        0
0;
```

```
          -k2   -k2*ltx    k2+2*k1  0          0         0          -k1    -k1       0
0;
          0     0          0        2*k1*lw^2 0         0          -k1*lw k1*lw     0
0;
          -k2   k2*ltx     0        0          k2+2*k1   0          0      0         -
k1    -k1;
          0     0          0        0          0         2*k1*lw^2  0      0         -
k1*lw k1*lw;
          0     0          -k1      -k1*lw     0         0          k1     0         0
0;
          0     0          -k1      k1*lw     0          0          0      k1        0
0;
          0     0          0        0          -k1       -k1*lw     0      0
k1     0;
          0     0          0        0          -k1       k1*lw      0      0         0
k1];

    Cv = [2*c2  0          -c2      0          -c2       0          0      0         0
0;
          0     2*c2*ltx^2 -c2*ltx  0          c2*ltx    0          0      0         0
0;
          -c2   -c2*ltx    c2+2*c1  0          0         0          -c1    -c1       0
0;
          0     0          0        2*c1*lw^2 0         0          -c1*lw c1*lw     0
0;
          -c2   c2*ltx     0        0          c2+2*c1   0          0      0         -
c1    -c1;
          0     0          0        0          0         2*c1*lw^2  0      0         -
c1*lw c1*lw;
          0     0          -c1      -c1*lw     0         0          c1     0         0
0;
          0     0          -c1      c1*lw     0          0          0      c1        0
0;
          0     0          0        0          -c1       -c1*lw     0      0
c1     0;
          0     0          0        0          -c1       c1*lw      0      0         0
c1];


    Fv = [mc; 0; mt; 0; mt; 0; mw; mw; mw; mw]*g;

end
```

InitialCalculations.m

```
%% Simulation Parameters

m = round(simL/slprI) + 1; % Number of sleepers or ballast elements
simL = (m-1)*slprI; % Making simulation length multiple of sleeper interval

%eleMRP = round((slprI-Pw)/0.050556); % Fixing the rail panel element size
%eleHRP = round(Pw/0.024167); % Fixing the sleeper panel element size

eleOne = eleMRP + 2*eleHRP; % Number of beam elements in one sleeper interval
eleTot = (m-1)*eleOne; % Number of beam elements in entire rail model
neqR = (eleTot+1)*2; % Total number of dof in rail FE model

% No. of iterations for left to right movement of wheels

steps = round((simL - axleDis(Nw) - (dFStt + dFStp))/(v*dt))+ stepsPRELOAD +
stepsPOSTLOAD;  % dFStt--- Distance of sim start from left end  (m).

 % dFStp--- Distance of sim stop from right end m


% No. of iterations for right to left movement of wheels
%steps = round((simL - (dFStt + dFStp))/(v*dt)) + stepsPRELOAD;


l = (slprI-Pw)/eleMRP; % Length of a beam element ij or is or js
lp = Pw/(2*eleHRP); % Length of beam element ss

% Constants for Newmark Method
C0 = 1/(beta*dt^2);
C1 = 1/(beta*dt);
C2 = 1/(2*beta) - 1;
C3 = gamma/(beta*dt);
C4 = gamma/beta - 1;
C5 = dt*(gamma/(2*beta) - 1);

% phi value for different beam elements
f = 12*EI/(G*A*chi*l^2);
fp = 12*EI/(G*A*chi*lp^2);
```

```
% Total degree of freedom of the system = neqR + 2*m + VDof;
% neqR - no. of dof of rail
% 2*m - no. of dof of sleeper and ballast
% VDof - no. of dof of vehicle

% Static wheel-rail contact force for first iteration (i=1)
Pst = (Fv(1,1) + 2*Fv(3,1) + Nw*Fv(7,1))/Nw;


%% Calculating global x-coordinates of all nodes on rail

% Vector of x-coordinates of one interval
Xint=zeros(eleOne+1,1);

% Complete vector
Xtot=zeros((m-1)*(eleOne)+ 1,1);

Xtot(1) = 0;
% On sleeper
for ii = 1:eleHRP
    Xint(ii+1) = Xint(ii) + lp;
end

% Between sleepers
for ii = eleHRP+1:(eleHRP+eleMRP)
    Xint(ii+1) = Xint(ii) + l;
end

% On sleeper
for ii = (eleHRP+eleMRP)+1:eleOne
    Xint(ii+1) = Xint(ii) + lp;
end

% Complete coordinates vector
for ii = 1 : m-1
    Xtot((ii-1)*eleOne+1:(ii)*eleOne+1)= Xint + slprI*(ii-1)*ones(eleOne+1,1);
end

%%
ww = EI/(G*A*chi);
```

SubMatrices.m

```
% Compiling Ms, Ks, Cs

[Mij,Kij] = BeamEleMatrix(l,f,mr,E,I,A); % Beam element mass and stiffness
                                         % matrix for beam element of length l
                                         % between sleepers.
%error('hi');

[Mijp,Kijp] = BeamEleMatrix(lp,fp,mr,E,I,A); % Beam element mass and stiffness
                                             % matrix for beam element of
                                             % length lp on sleepers.
% Rayleigh Damping
Cij = zeros(4);
Cijp = Cij;
%Cij = 0.005*Mij + 0.005*Kij;
%Cijp = 0.005*Mijp + 0.005*Kijp;


SubMassMatrix % Gives global substructure mass matrix Ms

SubK_C_Matrix1  % Gives global substructure stiffness Ks and damping matrix Cs
% SubK_C_Matrix1  % For variable Kb, Kp, Kf below each sleeper


% Applying the boundary conditions, Deleting:
% - the 2nd row and 2nd column (rotational dof of the 1st node)
% - the neqR th row and neqR th column (rotational dof of the last node)

if strcmp(TrackRecepCal,'Yes')
   RecepCal  % For calculation of track receptance
   error('Program stopped');
end

%Cs(1:neqR,1:neqR) = Cs(1:neqR,1:neqR) + 0.005*Ms(1:neqR,1:neqR) +
0.005*Ks(1:neqR,1:neqR);

% Nodes to be eliminated (Both ends fixed)
eliN1 = neqR-1:neqR;
eliN2 = 1:2;
nRem = length(eliN1) + length(eliN2);
```

```
Ks(eliN1,:) = []; Ks(:,eliN1) = [];
Ks(eliN2,:) = []; Ks(:,eliN2) = [];

Cs(eliN1,:) = []; Cs(:,eliN1) = [];
Cs(eliN2,:) = []; Cs(:,eliN2) = [];

Ms(eliN1,:) = []; Ms(:,eliN1) = [];
Ms(eliN2,:) = []; Ms(:,eliN2) = [];

nx = neqR - nRem + 2*m;  % Used for initialNodalDisplacement  % For example: Us_FP
= zeros(nx,1);  2020.0416 zsl

% Now Ms, Ks, Cs are of size (neqR + 2*m - nRem)x(neqR + 2*m -nRem)
```

PreMatrices.m

```
%% Calculating Av for Newton-Raphson
Av = Mv + Cv*gamma*dt + Kv*(dt^2)/6; %*beta


%% Calculating Keff for Newmark integration
Keff = Ks + C3*Cs + C0*Ms;

% Constants for Newmark Method (For reference)
% C0 = 1/(beta*dt^2);
% C1 = 1/(beta*dt);
% C2 = 1/(2*beta) - 1;
% C3 = gamma/(beta*dt);
% C4 = gamma/beta - 1;
% C5 = dt*(gamma/(2*beta) - 1);


% Cholesky factorisation    % It is special case of LU decomposition of a
% matrix A when A is a symmetric matrix i.e. A=A'. Then U becomes L'and
% A=LL'. Storing only one part L or L' saves computer memory.
UT = chol(Keff);
LT = UT';

%% EQUIVALENT NODAL LOADS FOR DISTRIBUTED LOAD (RAIL WEIGHT) 1:neqR
% Constant for all steps. Part of SubExtForces

% Calculate the distributed load per unit of length given by the mass
qv = mr*9.8; %N/m
```

```
Fsudl = zeros(neqR+2*m,1);
Fs1 = zeros(2*(eleOne+1),1);


for ii = 1:2:2*(eleOne+1)  % Calculates nodal loads for one rail panel

    if ii < 2*eleHRP
        Fs1(ii,1) = Fs1(ii,1) - qv*lp/2;
        Fs1(ii+1,1) = Fs1(ii+1,1) - qv*lp^2/12;
        Fs1(ii+2,1) = Fs1(ii+2,1) - qv*lp/2;
        Fs1(ii+3,1) = Fs1(ii+3,1) + qv*lp^2/12;
    end

    if ii >= 2*eleHRP+1 && ii < 2*(eleHRP+eleMRP)
        Fs1(ii,1) = Fs1(ii,1) - qv*l/2;
        Fs1(ii+1,1) = Fs1(ii+1,1) - qv*l^2/12;
        Fs1(ii+2,1) = Fs1(ii+2,1) - qv*l/2;
        Fs1(ii+3,1) = Fs1(ii+3,1) + qv*l^2/12;
    end

    if ii >= 2*(eleHRP+eleMRP)+1 && ii < 2*eleOne
        Fs1(ii,1) = Fs1(ii,1) - qv*lp/2;
        Fs1(ii+1,1) = Fs1(ii+1,1) - qv*lp^2/12;
        Fs1(ii+2,1) = Fs1(ii+2,1) - qv*lp/2;
        Fs1(ii+3,1) = Fs1(ii+3,1) + qv*lp^2/12;
    end

end


j=1;
while j+2<neqR  % Calculates nodal forces for entire rail length
    Fsudl(j:j+size(Fs1,1)-1) = Fsudl(j:j+size(Fs1,1)-1) + Fs1;
    j = j + size(Fs1,1)-2;
end

% According to boundary conditions:
Fsudl(eliN1) = [];   Fsudl(eliN2) = [];
```

InitialisingNodalDisplacements.m

```
%% Initialising SUBSTRUCTURE nodal displacements Us, Us1, Us2
% rail nodes: neqR-2, 2 nodes are reduced considering boundary conditions
% sleeper nodes: m
% ballast nodes: m

Us  = zeros(nx,1);   % displacement at the previous time step
Us1 = zeros(nx,1);   % velocity at the previous time step
Us2 = zeros(nx,1);   % acceleration at the previous time step

Us_i = Us;    % displacement at the current time step
Us1_i = Us1;  % velocity at at the current time step
Us2_i = Us2;  % acceleration at at the current time step

% Temporary variables to store Us_i, Us1_i, Us2_i for SubResolveLoop at
% h-th iteration.
Us_FP = zeros(nx,1);
Us1_FP = zeros(nx,1);
Us2_FP = zeros(nx,1);


uRailPlot = zeros(neqR+2*m,steps);      % stores rail nodal displacement at all
steps
uPlot = zeros(neqR+2*m,m);              % stores rail nodal acceleration at all
steps
u1Plot = zeros(neqR+2*m,m);
uS = zeros(Nw,m); u1S = uS; uB = uS; u1B = uS;
%u2SlprPlot = zeros(m, steps);          % contains sleeper nodal acceleration at
all steps
uSlprPlot = zeros(m, steps);

% Us_pf = Us;  % rail nodal displacement used to check convergence of rail
%              % nodal displacements through norm


%% Initialising VEHICLE nodal displacements Uv, Uv1, Uv2
Uv = zeros(VDof,1);      % displacement at the previous time step
Uv1 = zeros(VDof,1);     % velocity at the previous time step
Uv2 = zeros(VDof,1);     % acceleration at the previous time step

% Displacement values for time step i=1 coherent with static loads
```

```
Uv(3) = -( Fv(1)/2 + Fv(3))/(2*k1);            % Sign convention in matrix
formation is postive upwards for both vehicle EOM and substructure EOM. See
register.
Uv(5) = Uv(3);
Uv(1) = Uv(3) -  Fv(1)/(2*k2) ;

Uv_i = Uv;                      % displacement at at the current time step
Uv1_i = gamma*Uv1/beta/dt;      % velocity at at the current time step
Uv2_i = Uv/beta/dt^2;           % acceleration at at the current time step

% Temporary variables to store Uv_i, Uv1_i, Uv2_i for VehResolveLoop at
% k-th iteration.
Uv_NR = zeros(VDof,1);
Uv1_NR = zeros(VDof,1);
Uv2_NR = zeros(VDof,1);

%% Initialising variables related to WHEEL POSITION

% The position of the wheels is determined by several variables:

%xG_all = zeros(Nw,steps);    % Stores position of all wheels at all time instances
xG = zeros(Nw,1); % global x-coordinates of wheel. Distance between start and wheel
location
locR = zeros(Nw,1); % location of beam element in one sleeper interval
wPos = zeros(Nw,1); % nearest left beam element
xL = zeros(Nw,1); % local x-coordinates of wheel. Distance between wheel and
previous node on beam element
disFrLastSlpr = zeros(Nw,1); % distance between wheel and last sleeper
intNo = zeros(Nw,1); % interval on which wheel is located
Nf = zeros(4,Nw); % shape functions: one column per wheel
N = zeros(Nw,1); % rail defect function: one for each wheel location

Vxi = zeros(Nw,1); % Initialising beam element nodal displacements on which a
WHEEL-RAIL CONTACT occurs

D0 = zeros(Nw,1); % deformation of the previous time step (to calculate velocity)
D = zeros(Nw,1); % deformation of the current time step

Rst = zeros(VDof,1); % Stores rail-wheel impact force for all wheels

%%
```

```
RstNwPlot = zeros(Nw,steps);    % Stores Rst value for all wheels at all steps

h = zeros(steps,1,'int16');     % Will calculate and store the number of times
                                % SubResolveLoop runs at all time steps i
RE = zeros(Nw);                 % Part of Jacobian matrix
%Uv_iPlot = zeros(Nw,steps);    % Stores the vertical displacement of all wheels
                                % at all positions.
%VxiPlot = zeros(Nw,steps);
%DiffPlot = zeros(Nw,steps);
VehAccPlot = zeros(VDof,steps);    % Stores the vehicle nodal acceleration at all
steps.
%VehDisPlot = zeros(VDof,steps);  % Stores the vehicle nodal displacement at all
steps.
%slprLoc = zeros(Nw,m);
```

MainStepsLoop.m

```
%Waitbar creation
%wb=waitbar(0,'Iterations','Name','Progress');

i = 1; % Start of iteration


while i <= steps
    % Waitbar updation
%     if mod(i,1000)==0 || i==steps
%         waitbar(i/steps,wb,['steps: ',num2str(i),'/',num2str(steps),'
(',num2str(int8(100*i/steps)),'%) ','Time taken: ',num2str(int16(toc))]);
%     end

    WheelPos_ShapeFunc % Calculates wheel positions (wPos) & shape
    % functions(Nf) corresponding to the position of wheel
    % on a particular beam element i.e. sleeper
    % beam element or beam element in between sleepers.

    RailUnevenness % Calculates rail unevenness under each wheel (N) of
    % vehicle from TRC measured data depending upon
    % option selected in GUI.
    % Rail_unevenness = 0, No rail unevenness
    %                   1, Rail unevenness
```

```
    check_fp = 0;   % Variable used in SubResolveLoop to start it.
    h = 0;
    SubResolveLoop % Resolves rail nodal displacements at the current time
                   % step i
end
```

Acc_SperlingStability.m

```
%%%%%%%%%%%%%%%%%%%%%%%%%%%%%%%%%%%%%%%%%%%%%%%%%%%%%%%%%%%%%%%%%%%%%%%%%%%%
%%%     Sperling stability---ZSL  2020.02.12 %%%
%%%%%%%%%%%%%%%%%%%%%%%%%%%%%%%%%%%%%%%%%%%%%%%%%%%%%%%%%%%%%%%%%%%%%%%%%%%%
%TTS_MainStart       % ZSL
%% ----------------------------------------------------------------------
figure(1)
% t=1/1000:1/1000:N/1000;   %   Build time array t for sampling
% plot(t,z);        %   X: time t ,Y: vertical acceleration
plot(steps,z);      %   X: time t ,Y: vertical acceleration
xlabel('Time Unit：s');                         %  xlabel('Time Unit')
ylabel('Vertical acceleration Unit：m/s^2');   %  ylabel('Vertical acceleration
Unit：m/s^2')
title('Relationship between vertical acceleration and time');     %
title('Vertical acceleration-Time')
grid on;
axis([0,1/1000,-2.5,2.5]);
axis fill
%% ----------------------------------------------------------------------
fs=1000;        % 1000Hz---Sampling frequency is 1000Hz
fz=fft(z,N);    %  FFT  z: vehicle vertical acceleration   N: sampling number
a=abs(fz);      %  Modulus value(mo zhi) at each frequency, ZSL translate
a=a*2/N;        %  The modulus value at this point divided by N/2 is the amplitude
of the signal at the corresponding frequency.
n=0:N-1;
f=n*fs/N;       %  The frequency of each point, the first point is the component of
frequency 0, so the value of N is minused by 1.
%----------------------------------------------------------------------
figure(2)       %  plot vertical acceleration VS frequency
plot(f,a);
xlabel('frequency Unit:Hz');                          % xlabel('frequency
Unit:Hz');
```

```
ylabel('Vertical acceleration Unit:m/s^2');           % ylabel('Vertical
acceleration Unit」=m/s^2');
title('Relationship between vertical acceleration and frequency');   %
title('Relationship between vertical acceleration and frequency')
axis([0,30,0,0.1]);
axis fill
%% ------------------------------------------------------------------
 for i=1:N          %calculate vertical stability

f(i)=(i-1)*fs/N;
                   % The vibration frequency represented by each point.
                   % The first point is a component with a frequency of 0,
                   % so the value of i is reduced by one.

j(i)=(a(i)*100)^3;  % Unit of acceleration in the formula: cm/s^2
 end
syms i1 i2 i3        % to piecewise the frequency  % syms is used to define a
continuous function---ZSL
i1=round(0.5*N/fs);  %   for points: frequency 0.5Hz - 5.9Hz
i2=round(5.9*N/fs);  %   for points: frequency 5.9Hz - 20Hz
i3=round(20*N/fs);   %   for points: frequency >20Hz
sum=0;
for i=i1:i2                                  % Piecewise Calculation of
Stationarity Index
sum=sum+(0.896*(j(i)*0.325*f(i))^0.1)^10;    % The Sperling index refering the
criteria of B/T5599-1985
end
for i=i2+1:i3
sum=sum+(0.896*(j(i)*400/(f(i)^3))^0.1)^10;
end
for i=i3+1:N
sum=sum+(0.896*(j(i)/f(i))^0.1)^10;
end
Wz=(sum)^(0.1); % Total Stationarity Index


%%%%%%%%%%%%%%%%%%%%%%%%%%%%%%%%%%%%%%%%%%%%%%%%%%%%%%%%%%%%%%%%%%%%%%%%%%%%%%%
%%%       Max Acc of vehicle   m/s^2
%%%%%%%%%%%%%%%%%%%%%%%%%%%%%%%%%%%%%%%%%%%%%%%%%%%%%%%%%%%%%%%%%%%%%%%%%%%%%%%
%% Max Acc of vehicle   m/s^2

format long
```

```
[max_data,index1]=max(VehAccPlot(1,20001:steps));     % index is the location

Max_Vehi_Acc=max_data;                     % to calculate the max value of Acc


%%%%%%%%%%%%%%%%%%%%%%%%%%%%%%%%%%%%%%%%%%%%%%%%%%%%%%%%%%%%%%%%%%%%%%%%%%%%%%%%%%
%%%        Max WheelRail Force
%%%%%%%%%%%%%%%%%%%%%%%%%%%%%%%%%%%%%%%%%%%%%%%%%%%%%%%%%%%%%%%%%%%%%%%%%%%%%%%%%%

format long

[max_wheelrail,index2]=max(RstNwPlot(1,20001:steps));     % index is the location of max value   RstNwPlot(1,10001:steps)   20000steps means after 1s

Max_WheelRail=max_wheelrail;
```

SubMassMatrix.m

```
%% RAIL MASS MATRIX

% Geometric Stiffness Matrix - Stiffness increases when a member
% experiences tension and reduces when it experiences compression.
% Useful in buckling analysis. But this is MASS MATRIX. See fundamentals.

% Local mass matrix for one rail panel
Mint = sparse(2*(eleMRP+2*eleHRP+1),2*(eleMRP+2*eleHRP+1));

for ii = 1:eleHRP
    nodes = (2*ii-1):(2*ii-1)+3;
    Mint(nodes,nodes) = Mint(nodes,nodes) + Mijp;
end

j = ii + 1;
for ii = j:j + eleMRP - 1
    nodes = (2*ii-1):(2*ii-1)+3;
    Mint(nodes,nodes) = Mint(nodes,nodes) + Mij;

end
```

```
j = ii +1;
for ii = j:j + eleHRP - 1
    nodes = (2*ii-1):(2*ii-1)+3;
    Mint(nodes,nodes) = Mint(nodes,nodes) + Mijp;


end

% Global substructure mass matrix (rail+sleeper+ballast)
Ms = sparse(neqR+2*m,neqR+2*m);

% Assembling local rail panel mass matrix into global substructure mass matrix
ii = 1;
while ii <= neqR-size(Mint)+1
    nodes1 = ii:ii+size(Mint,1)-1;
    Ms(nodes1,nodes1) = Ms(nodes1,nodes1) + Mint;
    ii = ii + size(Mint,1)-2;
end

%% SLEEPER AND BALLAST MASS MATRIX
% Assembling sleeper and ballast masses into global substructure mass
% matrix
Ms(neqR+1:neqR+m,neqR+1:neqR+m) = ms*eye(m,m);
Ms(neqR+m+1:neqR+2*m,neqR+m+1:neqR+2*m) = mb*eye(m,m);
```

SubK_C_Matrix1.m

```
%% RAIL STIFFNESS AND DAMPING MATRIX

% Pre-allocating matrices
K_rail = sparse(neqR,neqR);      % K_rail - global stiffness matrix of the rail
model
C_rail = sparse(neqR,neqR);      % C_rail - global damping matrix of the rail model
slprDof = ones(m,1);             % slprDof - contains dof of center node of each
sleeper
slprEle = zeros(4+7*(m-2)+4,1); % Contains nodes which are on top of sleepers

%Kint = sparse(2*(eleMRP+2*eleHRP+1),2*(eleMRP+2*eleHRP+1));   % Assembled K matrix
that repeats at each sleeper interval
%Cint = sparse(2*(eleMRP+2*eleHRP+1),2*(eleMRP+2*eleHRP+1));   % Assembled C matrix
that repeats at each sleeper interval
```

```
% LOCAL C MATRICES
% Rail damping has been neglected as has been found to be negligible.
% Adding rubber pad damping at suitable degree of freedom
eleN = 0; ii=1;

for tt = 1:m-1

% Cis & Csj: damping matrices of the beam elements connected at the beginning
% or at the end to the sleeper
Cis = Cij + [0, 0, 0, 0; 0, 0, 0, 0; 0, 0, Cp/2, 0; 0, 0, 0, 0];
Csj = Cij + [Cp/2, 0, 0, 0; 0, 0, 0, 0; 0, 0, 0, 0; 0, 0, 0, 0];

%Css: damping matrix of the element on sleeper at both ends
Css = Cijp + [Cp/2, 0, 0, 0; 0, 0, 0, 0; 0, 0, Cp/2, 0; 0, 0, 0, 0];

% LOCAL K MATRICES


% Kis & Ksj: stiffness matrices of the elements connected at
% the beginning or at the end to sleeper
%Kis = Kij + [0, 0, 0, 0; 0, 0, 0, 0; 0, 0, Kp(tt)/2, 0; 0, 0, 0, 0];
Ksj = Kij + [Kp(tt)/2, 0, 0, 0; 0, 0, 0, 0; 0, 0, 0, 0; 0, 0, 0, 0];

%Kss: stiffness matrix of the element with both nodes on sleeper
Kss = Kijp + [Kp(tt)/2, 0, 0, 0; 0, 0, 0, 0; 0, 0, Kp(tt)/2, 0; 0, 0, 0, 0];




% Forming Kint and Cint

for ii = eleN+1:eleN+eleHRP
    rdof = (2*ii-1):(2*ii-1)+3;
    K_rail(rdof,rdof) = K_rail(rdof,rdof) + Kss;
    C_rail(rdof,rdof) = C_rail(rdof,rdof) + Css;
end

% nodes=[1:32]
%
array2table(full(Kint(nodes,nodes)),'RowNames','r'+string(nodes),'VariableNames','c
'+string(nodes))
```

```
%     error



ii = ii + 1;

rdof = (2*ii-1):(2*ii-1)+3;
K_rail(rdof,rdof) = K_rail(rdof,rdof) + Ksj;
C_rail(rdof,rdof) = C_rail(rdof,rdof) + Csj;


j = ii + 1;
for ii = j:j + eleMRP - 3
    rdof = (2*ii-1):(2*ii-1)+3;
    K_rail(rdof,rdof) = K_rail(rdof,rdof) + Kij;
    C_rail(rdof,rdof) = C_rail(rdof,rdof);
end

Kis = Kij + [0, 0, 0, 0; 0, 0, 0, 0; 0, 0, Kp(tt+1)/2, 0; 0, 0, 0, 0];
%Ksj = Kij + [Kp(tt+1)/2, 0, 0, 0; 0, 0, 0, 0; 0, 0, 0, 0; 0, 0, 0, 0];

%Kss: stiffness matrix of the element with both nodes on sleeper
Kss = Kijp + [Kp(tt+1)/2, 0, 0, 0; 0, 0, 0, 0; 0, 0, Kp(tt+1)/2, 0; 0, 0, 0, 0];


ii = ii + 1;

rdof = (2*ii-1):(2*ii-1)+3;
K_rail(rdof,rdof) = K_rail(rdof,rdof) + Kis;
C_rail(rdof,rdof) = C_rail(rdof,rdof) + Cis;


j = ii+1;
for ii = j:j + eleHRP - 1
    rdof = (2*ii-1):(2*ii-1)+3;
    K_rail(rdof,rdof) = K_rail(rdof,rdof) + Kss;
    C_rail(rdof,rdof) = C_rail(rdof,rdof) + Css;

end

eleN = eleN + eleOne;
slprDof(tt+1) = 2*(eleN+1)-1;
```

```
end


% Assembling global rail stiffness and damping matrix

% ii = 1; j = 1;
% slprDof(j) = 1;
% while ii <= neqR-size(Kint,1)+1
%
%     j=j+1;
%     C_rail(ii:ii+size(Cint,1)-1,ii:ii+size(Cint,1)-1) =
C_rail(ii:ii+size(Cint,1)-1,ii:ii+size(Cint,1)-1) + Cint;
%     K_rail(ii:ii+size(Kint,1)-1,ii:ii+size(Kint,1)-1) =
K_rail(ii:ii+size(Kint,1)-1,ii:ii+size(Kint,1)-1) + Kint;
%     ii = ii + size(Kint,1)-2;
%     slprDof(j)=ii;
%
%
% end

%% Calculates beam elements on top of sleepers which helps in plotting sleepers
ff=1;
for jj=1:m
    dof1 = (slprDof(jj) + 1)/2;
    if jj == 1
        slprEle(ff:ff+3) = dof1:dof1+3;
        ff = ff+7;
    elseif jj == m
        slprEle(ff-3:ff) = dof1-3:dof1;
    else
        slprEle(ff-3:ff+3) = dof1-3:dof1+3;
        ff = ff+7;
    end
end

ballastLoc = (slprDof+1)/2;  % Ballast and Sleeper node locations


% Geometric Stiffness Matrix - Stiffness increases when a member
% experiences tension and reduces when it experiences compression.
% Useful in buckling analysis. But this is MASS MATRIX. See fundamentals.
```

```
%% SLEEPER AND BALLAST STIFFNESS AND DAMPING MATRIX
Ak = diag(Kb) + (2*eleHRP+1)*diag(Kp);
Ac = (Cb + (2*eleHRP+1)*Cp)*eye(m,m);

Bk = zeros(m,neqR);
Bc = zeros(m,neqR);

j = 1;
for i = (1:m)
    Bk(i,j)= -Kp(i); %(i);
    Bc(i,j)= -Cp;

    for h = 1:eleHRP
        if i ~= m
            Bk(i,j+2*h) = -Kp(i);
            Bc(i,j+2*h) = -Cp;
        end
        if i ~= 1
            Bk(i,j-2*h) = -Kp(i);
            Bc(i,j-2*h) = -Cp;
        end
    end

    j = j + 2*(eleMRP+2*eleHRP);
end

i = 1;

Ck = (2*Kw)*eye(m,m) + diag(Kb) + diag(Kf);
Cc = (2*Cw+Cb+Cf)*eye(m,m);

% Condition at boundary
Ck(1,1) = (Kw+Kb(1)+Kf(1));
Cc(m,m) = (Cw+Cb+Cf);

for j =(1:m)
    for h =(1:m)

        if h == j + 1
            Ck(j, h) = -Kw;
        end
```

```
        if h == j - 1
            Ck(j, h) = -Kw;
        end

        if h == j + 1
            Cc(j, h) = -Cw;
        end

        if h == j - 1
            Cc(j, h) = -Cw;
        end

    end
end

%Dk = -Kb*eye(m);
Dk = -diag(Kb);
Dc = -Cb*eye(m);

% Assembling stiffness and damping matices of RAIL, SLEEPER and BALLAST
Ks = [K_rail, Bk', zeros(neqR,m); Bk, Ak, Dk; zeros(m, neqR), Dk', Ck];
Cs = [C_rail, Bc', zeros(neqR,m); Bc, Ac, Dc; zeros(m, neqR), Dc', Cc];


% for kk=neqR+m+27:neqR+m+34
%     Ks(kk,kk) = Kf*10;
% end
```

WheelPos_ShapeFunc.m

```
%% WHEEL POSITION
% if i>stepsPRELOAD
%     %if mod(runtime,2)==0
%
%     %else                                          % end of the end towards which
vehicle is moving.
%     % xG(1) = simL - axleDis(Nw) - (i-stepsPRELOAD)*v*dt - dFStp;
%     %end
% else
%     %if mod(runtime,2)==0
%     xG(1) = dFStt;
```

```
%     %else
%     %    xG(1) = simL - axleDis(Nw) - dFStp;
%     %end
%
% end

if i>stepsPRELOAD
    xG(1) = (i-stepsPRELOAD)*dt*v + dFStt; % Calculating distance of the last wheel
from the opposite
                                           % end of the end towards which vehicle
is moving.
else
    xG(1) = dFStt;
end



for j=(2:Nw)            % Calculating distance of other wheels from the
                        % entry end.

    xG(j) = xG(1) + axleDis(j);
end


xG_all(:,i) = xG;  % Stores position of all wheels at all time instances

%% SHAPE FUNCTIONS
for j = 1:Nw

    intNo(j,1) = floor(xG(j)/slprI)+1;  % sleeper interval in which the wheel is
located
    disFrLastSlpr(j) = xG(j) - (intNo(j)-1)*slprI; % distance of wheel from the
nearest sleeper


    % Finding the beam element on which wheel is located
    % Range 1
    if disFrLastSlpr(j) < Pw/2
        wPos(j) = floor(disFrLastSlpr(j)/lp) + 1;
        xL(j) = disFrLastSlpr(j) - (wPos(j)-1)*lp;
        locR(j) = 1;
        wPos(j) = wPos(j) + (intNo(j)-1)*eleOne;
```

```
        l_b = lp;
        l_f = fp;

    end

    % Range 2
    if disFrLastSlpr(j,1) >= Pw/2 && disFrLastSlpr(j,1) < Pw/2 + (slprI - Pw)
        wPos(j,1) = floor((disFrLastSlpr(j,1) - lp*eleHRP)/l) + 1;
        xL(j,1) = disFrLastSlpr(j,1) - lp*eleHRP - (wPos(j,1)-1)*l;
        locR(j,1) = 2;
        wPos(j,1) = wPos(j,1)+ (intNo(j,1)-1)*eleOne + eleHRP;
        l_b = l;
        l_f = f;
    end

    % Range 3
    if disFrLastSlpr(j,1) >= Pw/2 + (slprI-Pw)
        wPos(j,1) = floor((disFrLastSlpr(j,1)-lp*eleHRP-l*eleMRP)/lp) + 1;
%         if xG(j) == simL
%             wPos(j) = floor((disFrLastSlpr(j,1)-lp*eleHRP-l*eleMRP)/lp);
%         end
        xL(j,1) = disFrLastSlpr(j,1) - lp*eleHRP - l*eleMRP - (wPos(j,1)-1)*lp;
        locR(j,1) = 3;
        wPos(j,1) = wPos(j,1)+ (intNo(j,1)-1)*eleOne + eleHRP + eleMRP;
        l_b = lp;
        l_f = fp;
    end

%     if wPos(j) > eleTot  % If the wheel goes slightly out of simL
%           wPos(j) = wPos(j) - 1;
%     end


    gxi = xL(j,1)/l_b;
    mu(j) = (-2*xL(j)^3 + 3*l_b*xL(j)^2 + 12*ww*xL(j))/(l_b^3 + 12*ww*l_b);

    % shape functions
    Nf(1,j) = 1 / (1 + l_f) * (1 + 2*gxi^3 - 3*gxi^2 + l_f*(1 - gxi));
    Nf(2,j) = -l_b / ( 1 + l_f) * (gxi + gxi^3 - 2*gxi^2 + l_f / 2 * (gxi -
gxi^2));
    Nf(3,j) = 1 / (1 + l_f) * (-2*gxi^3 + 3*gxi^2 + l_f*gxi);
    Nf(4,j) = -l_b / ( 1 + l_f) * (gxi^3 - gxi^2 + l_f/2*(gxi^2 - gxi));
```

```
%     if xG(j) > simL
%         Nf(:,j)=0;
%     end

end
```

RailUnevenness.m

```
if Rail_unevenness == 1 % && i>stepsPRELOAD
    N = zeros(Nw,1);

    %% TRC calculated defect  %%%%%%%%%%%%%%%%%%%%%%%%%%%%%%%%%%%%%%%%%%%%
    if strcmp(RUType,'TRC')
        amp = 1e-3; %2.71e-3; % 1e-6;  %1e-8; % Rail Unevenness Amplitude (m)
        RI_wavelength = 9.6; % Rail Unevenness Wavelength (m)

        b1=RI_wavelength;
        A1=b1;
        B1=RI_wavelength/2;


        for whl=1:Nw
            dist= xG(whl,1);   % global x-coordinates of wheel. Distance between
start and current wheel location
            k1=floor(dist/RI_wavelength);
            N(whl)= amp/2 * (1 - cos(2*pi/b1*(dist - k1*A1 - B1))); % Dynamics of
railway bridges. L. Fryba Pg 122
        end  % N contains uneveness magnitude (positive values) as track unevenness
which are
        % subtracted from vehicle displacement

        % Rail unevenness at each node used for plotting
        k1=floor(Xtot/RI_wavelength);
        RUneven = amp/2 * (1 - cos(2*pi/b1*(Xtot - k1*A1 - B1))) ;
    end

    %% Wheel flat defect  %%%%%%%%%%%%%%%%%%%%%%%%%%%%%%%%%%%%%%%%%%%%
    if strcmp(RUType,'WheelFlat')
        b1 = 40/1000;  % Length of the wheel flat
        amp(1:Nw) = [0,0,0,0.35/1000]; % Depth of the wheel flat
```

```
        A1 = 2*pi*rw;
        B1 = axleDis(Nw) + disFrEdge;

        for whl=1:Nw
            dist= xG(whl);   % global x-coordinates of wheel. Distance between
start and current wheel location
            %k1=floor(dist/A1);
            k1=floor((dist - B1)/A1);
            if dist > B1 + k1*A1 && dist < B1+ k1*A1 + b1 && k1>=0
                N(whl)= amp(whl)/2 * (1 - cos(2*pi/b1*(dist - k1*A1 - B1))); %
Dynamics of railway bridges. L. Fryba Pg 122
            end
        end  % N contains uneveness magnitude (positive values) as track unevenness
which are
        % subtracted from vehicle displacement

        % Rail unevenness at each node used for plotting
        if i == 1
            RUneven = zeros(length(Xtot),1);

            for tt = 1:length(Xtot)
                k1=floor((Xtot(tt)- B1)/A1);
                if Xtot(tt) > B1 +k1*A1 && Xtot(tt) < B1+ k1*A1 +b1 && k1>=0
                    RUneven(tt) = amp(4)/2 * (1 - cos(2*pi/b1*(Xtot(tt) - k1*A1 -
B1)));
                    %RUneven(tt)
                end

            end
        end
    end

    %% Isolated irregularity defect - Zhai   ---( wheel flat---
zhang) %%%%%%%%%%%%%%%%%%%%%%%%%%%%%%%%%%%%%%%%%%%%%%%%%%%%
    if strcmp(RUType,'Isolated')
        dipAngle = 0.02; % 2*alpha
        b1 = 1; %v*dt;  %1000/1000;  % Length of the wheel flat
        amp = (dipAngle/1)*(b1/2); % Depth of the wheel flat

        for whl=1:Nw
            dist= xG(whl);   % global x-coordinates of wheel. Distance between
start and current wheel location
```

```
            if dist >= simL/2 && dist < simL/2 + b1/2
                %Uv1(6+whl) = -v*dipAngle;  % Impact velocity Ref: Sun and
Dhanasekar % Better results
                % Uv1(6+whl) = -v*dipAngle;  % Impact velocity (dipped joint)
                N(whl)= -amp * (1 - cos(2*pi/b1*(dist - simL/2)/2)); % Dynamics of
railway bridges. L. Fryba Pg 122
            end
            if dist >= simL/2 + b1/2 && dist <= simL/2 + b1
                %Uv1(6+whl) = -v*dipAngle;  % Impact velocity Ref: Sun and
Dhanasekar % Better results
                N(whl)= -amp * (1 + cos(2*pi/b1*(dist - simL/2)/2)); % Dynamics of
railway bridges. L. Fryba Pg 122
            end
        end  % N contains uneveness magnitude (positive values) as track unevenness
which are
        % subtracted from vehicle displacement

        % Rail unevenness at each node used for plotting
        if i == 1
            RUneven = zeros(length(Xtot),1);

            for tt = 1:length(Xtot)
                %k1=floor((Xtot(tt)- B1)/A1);
                if Xtot(tt) > simL/2 && Xtot(tt) < simL/2 + b1
                    RUneven(tt) = amp/2 * (1 - cos(2*pi/b1*(Xtot(tt) - simL/2)));
                    %RUneven(tt)
                end

            end
        end
    end

    %% Differential height - Zhai    ---(jagged joint---
zhang) %%%%%%%%%%%%%%%%%%%%%%%%%%%%%%%%%%%%%%%%%%%%%%%%%%%%
    if strcmp(RUType,'DifferentialHeight')
        b1 = v*dt;
        diffHt = 1/1000;


        for whl=1:Nw
            dist= xG(whl);   % global x-coordinates of wheel. Distance between
start and current wheel location
```

```
            if  dist >= simL/2 && dist  <= simL/2 + b1
                Uv1(6+whl) = v*sqrt(2*diffHt/rw);
                %N(whl)= 1/1000; % Dynamics of railway bridges. L. Fryba Pg 122
            end
        end  % N contains uneveness magnitude (positive values) as track unevenness
which are
        % subtracted from vehicle displacement

        % Rail unevenness at each node used for plotting
        if i == 1
            RUneven = zeros(length(Xtot),1);

            for tt = 1:length(Xtot)
                if Xtot(tt) > simL/2 && Xtot(tt)  < simL/2 + b1
                    RUneven(tt) = 1/1000;
                end

            end
        end
    end

%% Frost Heave Rail Irregularity Data - Can be used for differential
settlement %%%%%%%%%%%%%%%%%%%%%%%%%%%%%%%%%%%%%%%%%%%%%%%%%%%%
    if strcmp(RUType,'FrostHeave')

        %Frost Heave
% % % % % % %             RailIrrData=[-1E-6,0.00644,0.01493,0.03566....
% % % % % % %                    0.06201,0.10223,0.15594,0.22731,0.32922,0.45344...
% % % % % % %                    0.64123,0.85355,1.18387,1.53439,2.06876,2.66076...
% % % % % % %                    3.42566,4.35351,5.42125,6.74765,8.18221,9.6935...
% % % % % % %                    11.18982,12.53377,13.63431,13.92302,13.63431...
% % % % % % %
12.53377,11.18973,9.69325,8.18212,6.74765,5.42125...
% % % % % % %                    4.3554,3.42799,2.66123,2.06876,1.53439,1.18387...
% % % % % % %                    0.85066,0.6167,0.43685,0.32314,0.22731,0.15594...
% % % % % % %                    0.10223,0.06201,0.03566,0.01493,0.00644,-1E-6];  %
Freezing period---GWL6m (30m)

%
RailIrrData=[0,0.05478,0.21852,0.48943,0.86455,1.33975,1.90983...
%                            2.56855,3.30869,4.12215,5,5.93263,6.90983,7.92088...
%                            8.95472,10,11.04528,12.07912,13.09017,14.06737...
```

```
%                                15,15.87785,16.69131,17.43145,18.09017,18.66025...
%                                19.13545,19.51057,19.78148,19.94522,20,19.94522...
%                                19.78148,19.51057,19.13545,18.66025,18.09017...
%                                17.43145,16.69131,15.87785,15,14.06737,13.09017...
%                                12.07912,11.04528,10,8.95472,7.92088,6.90983...
%                                5.93263,5,4.12215,3.30869,2.56855,1.90983,1.33975...
%                                0.86455,0.48943,0.21852,0.05478,0]/1000;  % Frost
heave Cai (cos wave)  2020.0327


RailIrrData=[ 0,0.01973,0.07885,0.17713,0.31417,0.48943,0.70224,0.95173,1.23693...

1.55672,1.90983,2.29487,2.71031,3.15453,3.62576,4.12215,4.64173...

5.18246,5.74221,6.31875,6.90983,7.5131,8.12619,8.74667,9.37209...

10,10.62791,11.25333,11.87381,12.4869,13.09017,13.68125,14.25779...

14.81754,15.35827,15.87785,16.37424,16.84547,17.28969,17.70513,18.09017...

18.44328,18.76307,19.04827,19.29776,19.51057,19.68583,19.82287,19.92115...

19.98027,20,19.98027,19.92115,19.82287,19.68583,19.51057,19.29776...

19.04827,18.76307,18.44328,18.09017,17.70513,17.28969,16.84547...

16.37424,15.87785,15.35827,14.81754,14.25779,13.68125,13.09017...

12.4869,11.87381,11.25333,10.62791,10,9.37209,8.74667,8.12619...

7.5131,6.90983,6.31875,5.74221,5.18246,4.64173,4.12215,3.62576...

3.15453,2.71031,2.29487,1.90983,1.55672,1.23693,0.95173,0.70224...

0.48943,0.31417,0.17713,0.07885,0.01973,0]/1000;  % Frost heave Cai (cos wave)
2020.00427


        %RailIrrData =  (SlprDiffSet2-min(SlprDiffSet2))/SlToRail;  %100e-
3*rand(1,m);

% %         load mat60.mat SlprDiffSet2    % For Impact Force Validation
```

```
% %         RailIrrData = SlprDiffSet2;

% 2020.0415        noOfDataPoints = length(RailIrrData);
%         irrStart = (x2(1)-1)*slprI;
%         irrStop = (x2(end)-1)*slprI;
%         interSize = (irrStop - irrStart)/(noOfDataPoints - 1); % Size of one
interval
%
% 2020.0415        RU = [irrStart:interSize:irrStop; RailIrrData];
        noOfDataPoints = length(RailIrrData);
        irrStart = (s1-1)*slprI;
        irrStop = (s2-1)*slprI;
        interSize = (irrStop - irrStart)/(noOfDataPoints - 1); % Size of one
interval

        RU = [irrStart:interSize:irrStop; RailIrrData];

        N = zeros(1,Nw);
        for whl=1:Nw
            dist= xG(whl); % global x-coordinates of wheel. Distance between start
and current wheel location

            %N(whl) = 0;
            for kkk = 1 : size(RU,2)-1
                %[RU(1, kkk) dist RU(1, kkk+1)]
                %pause
                if dist >= RU(1,kkk) && dist <= RU(1,kkk+1)
                    %gradient = (RU(2,kkk+1) - RU(2,kkk))/(RU(1,kkk+1) -
RU(1,kkk));
                    %N(whl) = -1*(RU(2,kkk) +  gradient * (dist - RU(1,kkk)));

%                     % CHANGE SIGN
%                     xb = dist - RU(1,kkk);             %2020.0415  ZSL
%                     XB = RU(1,kkk+1) - RU(1,kkk);      %2020.0415  ZSL
%                     N(whl) = -1*( RU(2,kkk) * (1 - 3*(xb/slprI)^2 +
2*(xb/slprI)^3) + RU(2,kkk+1) * (3*(xb/slprI)^2 - 2*(xb/slprI)^3));  % 2020.0415
ZSL
                    N(whl) = RU(2,kkk) + ((RU(2,kkk+1) - RU(2,kkk))/(RU(1,kkk+1)
- RU(1,kkk))) * (dist - RU(1,kkk));
                    % N(whl) = -1*( RU(2,kkk) +   (3*(xb/slprI)^2 - 2*(xb/slprI)^3)
* (RU(2,kkk+1)-RU(2,kkk)) );
```

```
                    break;
                end
            end

            %k1=floor(dist/RI_wavelength);
            %N(whl)= N(whl) + amp/2 * (1 - cos(2*pi/b1*(dist - k1*A1 - B1)));


        end  % N contains uneveness magnitude (positive values) as track unevenness
which are
        % subtracted from vehicle displacement

        %[i N]

        % Plotting rail profile
        for jjj = 1:length(Xtot)

            RUneven(jjj) = 0;
            for kkk = 1 : size(RU,2)-1
                if Xtot(jjj) >= RU(1,kkk) && Xtot(jjj) <= RU(1,kkk+1)

                    RUneven(jjj) = RU(2,kkk) + ((RU(2,kkk+1) -
RU(2,kkk))/(RU(1,kkk+1) - RU(1,kkk))) * (Xtot(jjj) - RU(1,kkk)) ;
                    break;

                end
            end
        end
        RUneven = RUneven';

    end
%% Frost Heave Rail Irregularity Data - Can be used for differential settlement---
zsl %%%%%%%%%%%%%%%%%%%%%%%%%%%%%%%%%%%%%%%%%%%%%%%%
    if strcmp(RUType,'FT_Deformation')    % FreezeThaw_paper

%%%%%%%%%------Load Frost Heave or thaw settlement

%        FreezeThaw=load('JR_HOKKAIDO_1_1000m.txt');   % Unit: mm

% FreezeThaw=load('Freeze_Box_5m.txt');    %% 150m   Unit: mm
% FreezeThaw=load('Freeze_Box_7m.txt');    %% 150m   Unit: mm
% FreezeThaw=load('Freeze_Box_9m.txt');    %% 150m   Unit: mm
```

```
% FreezeThaw=load('Freeze_Box_13m.txt');    %% 150m   Unit: mm
FreezeThaw=load('Freeze_Box_18m.txt');    %% 150m   Unit: mm

% FreezeThaw=load('Freeze_Pipe_5m.txt');    %% 150m   Unit: mm
% FreezeThaw=load('Freeze_Pipe_7m.txt');    %% 150m   Unit: mm
% FreezeThaw=load('Freeze_Pipe_9m.txt');    %% 150m   Unit: mm
% FreezeThaw=load('Freeze_Pipe_13m.txt');    %% 150m   Unit: mm
% FreezeThaw=load('Freeze_Pipe_18m.txt');    %% 150m   Unit: mm

%%%%%%%%%
       T_FreezeThaw=FreezeThaw(:,2);
       RailIrrData=T_FreezeThaw'/1000;

        noOfDataPoints = length(RailIrrData);
        irrStart = (s1-1)*slprI;
        irrStop = (s2-1)*slprI;
%               irrStart = 0;
%               irrStop =(m-1)*slprI;

        interSize = (irrStop - irrStart)/(noOfDataPoints - 1); % Size of one
interval

        RU = [irrStart:interSize:irrStop; RailIrrData];        % interplate the
RailIrrData
        RUt=RU';

        N = zeros(1,Nw);
        for whl=1:Nw
            dist= xG(whl); % global x-coordinates of wheel. Distance between start
and current wheel location

            %N(whl) = 0;
            for kkk = 1 : size(RU,2)-1
                %[RU(1, kkk) dist RU(1, kkk+1)]
                %pause
                if dist >= RU(1,kkk) && dist <= RU(1,kkk+1)
                    %gradient = (RU(2,kkk+1) - RU(2,kkk))/(RU(1,kkk+1) -
RU(1,kkk));
                    %N(whl) = -1*(RU(2,kkk) +  gradient * (dist - RU(1,kkk)));

%                     % CHANGE SIGN
%                     xb = dist - RU(1,kkk);            % 2020.0415  ZSL
```

```
%                       XB = RU(1,kkk+1) - RU(1,kkk);      % 2020.0415  ZSL
%                       N(whl) = -1*( RU(2,kkk) * (1 - 3*(xb/slprI)^2 +
2*(xb/slprI)^3) + RU(2,kkk+1) * (3*(xb/slprI)^2 - 2*(xb/slprI)^3));  % 2020.0415
ZSL
                        N(whl) = RU(2,kkk) + ((RU(2,kkk+1) - RU(2,kkk))/(RU(1,kkk+1)
- RU(1,kkk))) * (dist - RU(1,kkk));
                    % N(whl) = -1*( RU(2,kkk) +   (3*(xb/slprI)^2 - 2*(xb/slprI)^3)
* (RU(2,kkk+1)-RU(2,kkk)) );

                    break;
                end
            end

            %k1=floor(dist/RI_wavelength);
            %N(whl)= N(whl) + amp/2 * (1 - cos(2*pi/b1*(dist - k1*A1 - B1)));


        end  % N contains uneveness magnitude (positive values) as track unevenness
which are
        % subtracted from vehicle displacement

        %[i N]

        % Plotting rail profile
        for jjj = 1:length(Xtot)

            RUneven(jjj) = 0;
            for kkk = 1 : size(RU,2)-1
                if Xtot(jjj) >= RU(1,kkk) && Xtot(jjj) <= RU(1,kkk+1)

                    RUneven(jjj) = RU(2,kkk) + ((RU(2,kkk+1) -
RU(2,kkk))/(RU(1,kkk+1) - RU(1,kkk))) * (Xtot(jjj) - RU(1,kkk)) ;
                    break;

                end
            end
        end
        RUneven = RUneven';

    end
%% Cai's Irregularity Data    ----
zsl    %%%%%%%%%%%%%%%%%%%%%%%%%%%%%%%%%%%%%%%%%%%%%%%%%%%%%%%%
```

```
    if strcmp(RUType,'Reliability_Cai')
       Cai=load('Zv_Irre_Cai_240m.txt');   %% Unit: mm
       TCai=Cai(:,1);
       RailIrrData=TCai;

        noOfDataPoints = length(RailIrrData);
        irrStart =0;
        irrStop = m*slprI;
        interSize = (irrStop - irrStart)/(noOfDataPoints - 1); % Size of one
interval

  RU = [irrStart:interSize:irrStop; RailIrrData];


        for whl=1:Nw
            dist= xG(whl,1);   % global x-coordinates of wheel. Distance between
start and current wheel location
            N(whl) = 0;
            for kkk = 1 : size(RU,1)-1
                if dist >= RU(1,kkk) && dist <= RU(1,kkk+1)
                    N(whl) = RU(2,kkk) + ((RU(2,kkk+1) - RU(2,kkk))/(RU(1,kkk+1) -
RU(1,kkk))) * (dist - RU(1,kkk));
                    break;
                end
            end
        end  % N contains uneveness magnitude (positive values) as track unevenness
which are
        % subtracted from vehicle displacement

        % Plotting rail profile
        for jjj = 1:length(Xtot)

            RUneven(jjj) = 0;
            for kkk = 1 : size(RU,2)-1
                if Xtot(jjj) >= RU(1,kkk) && Xtot(jjj) <= RU(1,kkk+1)

                    RUneven(jjj) = RU(2,kkk) + ((RU(2,kkk+1) -
RU(2,kkk))/(RU(1,kkk+1) - RU(1,kkk))) * (Xtot(jjj) - RU(1,kkk)) ;
                    break;

                end
            end
```

```
        end
        RUneven = RUneven';
    end
end
```

SubResolveLoop.m

```
while(check_fp == 0)

    h = h+1; % Counts the number of iterations need to solve the substructure
             % nodal displacements at current time step i


    RailDispUnderWheel %(wPos, Us_i, Nf, Nw, eleTot);   %% Restored


    for j=(1:Nw)
        [Rst(6+j), D(j)] = Hertz(dt, Uv_i(6+j), Kh, Vxi(j), N(j), DO(j), Ch,
i);     % Restored loop
        % upon relative vertical displacement between wheel (Uv_i), rail (Vxi) and
        % rail irregularity (N(j)).

    end

    SubExtForces  % Calculates the BEAM ELEMENT NODAL FORCES (Fs_i) for
current         % Changed i==1 condn
    % wheel position (wPos) and time step as a sum of CONCENTRATED FORCE
    % of rail-wheel impact force (Rst) for current step, when present on a
    % beam element and adds it to the DISTRIBUTED LOAD (Fs_udl) due to weight
    % of the rail (mr) which is calculated only once before MainStepsLoop
    % starts in PreMatrices.


    NewmarkMethod  % Calculates RAIL NODAL DISPLACEMENTS (Us_i) due to
    % current time-step rail nodal forces (Fs_i) using Newmark beta
    % method.


    if norm(Us_i-Us_FP)/norm(Us_i) < err % Checking CONVERGENCE of
```

```
        % current time step nodal displacments (Us_i) with previous
        % time step nodal displacements (Us_pf) using norm. If
        % difference is within permissible error then the code moves
        % onto next time step i.

        % Updating rail nodal variables (Us, Us1, Us2) and vehicle
        % nodal variables (Uv, Uv1, Uv2) for the next comparison and
        % exiting from while loop

        % Updating substructure nodal velocity and acceleration values for the
        % next i-th step
        Us2_i = C0*(Us_i-Us) - C1*Us1 - C2*Us2; % Acceleration at time i+1
        Us1_i = C3*(Us_i-Us) - C4*Us1 - C5*Us2; % Velocity at time i+1

        Us  = Us_i;
        Us1 = Us1_i;
        Us2 = Us2_i;

        uP = [0;0;Us_i(3:neqR-2,1);0;0;Us_i(neqR-nRem+1:neqR-nRem+2*m)];
        u1P = [0;0;Us1_i(3:neqR-2,1);0;0;Us1_i(neqR-nRem+1:neqR-nRem+2*m)];


        for jj=1:Nw

            if mod(xG(jj),slprI) < v*dt  || mod(xG(jj) + v*dt, slprI) < v*dt
               slprNo = round(xG(jj)/slprI)+1;

               %slprLoc(jj,slprNo) = i;  % Stores step no. 'i' when wheel 'jj' is
over sleeper 'slprNo'
               uS(jj,slprNo) = uP(neqR+slprNo);   % Stores sleeper nodal
displacement when wheel 'jj' is over sleeper 'slprNo'
               u1S(jj,slprNo) = u1P(neqR+slprNo); % Stores sleeper nodal velocity
when wheel 'jj' is over sleeper 'slprNo'
               uB(jj,slprNo) = uP(neqR+m+slprNo); % Stores ballast mass nodal
displacement when wheel 'jj' is over sleeper 'slprNo'
               u1B(jj,slprNo) = u1P(neqR+m+slprNo); % Stores ballast mass nodal
velocity when wheel 'jj' is over sleeper 'slprNo'

            end
        end

        Uv  = Uv_i;
```

```
        Uv1 = Uv1_i;
        Uv2 = Uv2_i;

        %uRailPlot(:,i)= [0;0;Us_i(3:neqR-2,1);0;0;Us_i(neqR-nRem+1:neqR-
nRem+2*m)];
        %u1RailPlot(:,i) = [0;0;Us1_i(3:neqR-2,1);0;0;Us1_i(neqR-nRem+1:neqR-
nRem+2*m)];
        %uRailPlot(:,i)= [Us_i(1,1);0;Us_i(2:neqR-2,1);0;Us_i(neqR-2+1:neqR-
2+2*m)]; % Used for
        % plotting vertical displacement of rail nodes at all time steps.

        %%uRail2Plot(:,i)= [0;0;Us2_i(3:neqR-2);0;0;Us2_i(neqR-nRem+1:neqR-
nRem+2*m)];
        %uRail2Plot(:,i)= [Us2_i(1);0;Us2_i(2:neqR-2);0;Us2_i(neqR-2+1:neqR-
2+2*m)]; % Used for
        % plotting vertical displacement of rail nodes at all time steps.

        %uRailNode2Plot(i) = Us2_i(neqR/2); % Used for plotting rail acceleration
at all time steps

        Uv_iPlot(:,i) = Uv_i(7:VDof);  % Used for plotting vertical
        % displacement of wheel nodes at all time steps.

        %VxiPlot(:,i) = Vxi;

        %RstMeanPlot(i) = mean(Rst(7:VDof));  % Used for calculating and
        % plotting mean Rst at all time steps. Used for settlement calculation.

        RstNwPlot(:,i) = Rst(7:VDof);    % Used for plotting Rst of a particular
wheel
                                         % at all time steps.


        %DiffPlot=Uv_iPlot-VxiPlot;

        %u2SlprPlot(:,i) = Us2(neqR-nRem+1:neqR-nRem+m);
        %uSlprPlot(:,i) = Us(neqR-nRem+1:neqR-nRem+m);

        VehAccPlot(:,i) = Uv2_i; % Used for plotting vehicle nodal acceleration at
all time steps.
        VehDisPlot(:,i) = Uv_i;  % Used for plotting vehicle nodal displacement at
all time steps.20191109
```

```
        % Storing current relative penetration between wheel and rail(D)
        % as previous relative penetration (DO)which is used in Hertz to
        % calculate relative penetration velocity (D1) and thus Hertz
        % contact force (Rst)
        DO = D;

        i = i+1;

        if mod(i,2000)==0    % Displays steps         %2020.0409--zsl
            if  i==2000                                %2020.0409--zsl
                disp(['Total steps = ',num2str(steps)]);
                disp('Current Step');
            end
            disp(i);
        end


        break
    end

    %% IF CONVERGENCE AT THE CURRENT hth STEP IS NOT FULFILLED

    % Substructure (rail+sleeper+ballast) nodal displacements, velocities
    % accelerations are updated. Us_FP is a temporary value for h-th
    % iteration updation. It is not to be confused with Us which is nodal
    % displacement of previous i-th step.

    Us_FP = Us_i;
%     Us1_FP = Us1_i;  % No use.
%     Us2_FP = Us2_i;

    RailDispUnderWheel%(wPos, Us_i, Nf, Nw, eleTot); % Calculates new
        % rail vertical displacement (Vxi) under the wheel using NEW
        % substructure nodal deformations (uRailPlot(:,i)) which contain
        % all nodal displacements including the two removed rotations at
        % node '2' and node 'neqR' which are boundary conditions.



        % Calculates the rail
    % vertical displacement exactly at the location under the wheel
```

```
    % (Vxi) using present rail nodal deformations of the 4 dof of the
    % beam element on which wheel (Us) is present interpolated with
    % shape functions (Nf)

    % v(x,t) = N(x).Us(t)     (Beam Element 2)
    % x - location of wheel on beam element
    % t - nodal displacements depending upon time??


    % Calculating bv which is part of Func_k function which is vehicle
    % equations of motion.

    % Sign of Fv is negative downwards. When brought to RHS it becomes postive.
    % Sign of Kv and Cv will depend upon the sign of nodal displacements.
    %%%%%bv = Fv + Kv*(Uv + dt*Uv1 + (0.5-beta)*(dt^2)*Uv2)...
    %%%%%    + Cv*(Uv1 + (1-gamma)*dt*Uv2);
    bv = Fv + Kv*(Uv + dt*Uv1 + (1/3)*(dt^2)*Uv2)...
        + Cv*(Uv1 + (1-gamma)*dt*Uv2);



    check = 0; % Variable to guide entry into VehResolveLoop_NR loop
    k = 1;  % Counter for number of iterations in VehResolveLoop_NR

%     result = fsolve(@(z) eqns(z,Av,bv,VDof), [Uv2_i;Rst],
optimoptions('fsolve','Algorithm','levenberg-
marquardt','Display','off','StepTolerance',1e-4));
%
%     Uv2_i = result(1:VDof);
%     Rst = result(VDof+1:VDof+VDof);
    VehResolveLoop_NR % Solves equations of motions (EsOM) of vehicle model which
                      % is a non-linear system equations between
                      % vehicle nodal displacements (Uv_i), velocities (Uv1_i)
                      % and accelerations (Uv2_i), rail-wheel contact
                      % forces (Rst) acting on the vehicle wheel nodes,
                      % mass (Mv), stiffness (Kv), damping (Cv) and weight
                      % (Fv)matrices. Since the EsOM are non-linear, they
                      % are solved by Newton-Raphson method.


    % Results of the NR iterations for hth SubResolveLoop.
     Uv1_i = Uv1 + (1-gamma)*dt*Uv2 + gamma*dt*Uv2_i;
```

```
    %Uv_i = Uv + dt*Uv1 + (0.5 - beta)*dt^2*Uv2 + beta*dt^2*Uv2_i;     % Changed
    Uv_i = Uv + dt*Uv1 + (1/3)*dt^2*Uv2 + (1/6)*dt^2*Uv2_i;
    %Uv2_i also given

    if h == 100000
        error('PF_BREAK - over 10000 iterations at this time step, CHECK IT!!');
    end

end
```

NewmarkMethod.m

```
% Newmark beta method - Implicit method - As solution at time i+1 is
% determined from the equation of motion (EOM) at time i+1.

% Calculating the effective load
if i==1
    Feff = Fs_i;
else
    Feff =  Fs_i + Ms*(C0*Us + C1*Us1 + C2*Us2) + Cs*(C3*Us + C4*Us1 + C5*Us2);
end

% Fs - nodal load array containing distributed load of rail and
% concentrated wheel rail contact force wherever present.

% Cholesky factorisation (See Matrix Decompositions)
                      % LT from SubMatrices after Cholesky decomposition of
                      % Keff matrix.
                      % Keff x Us_i = Feff
                      % L x L' x Us_i = Feff
                      % LT x UT x Us_i = Feff
y = LT¥Feff;          % (UT x Us_i) = inv(LT) * Feff
                      % (UT x Us_i) = y
Us_i = UT¥y;          % Us_i = inv(UT) *

% % Constants for reference
% C0 = 1/(beta*dt^2);
% C1 = 1/(beta*dt);
% C2 = 1/(2*beta) - 1;
% C3 = gamma/(beta*dt);
% C4 = gamma/beta - 1;
% C5 = dt*(gamma/(2*beta) - 1);
```